

**OPTICAL DISC DESIGN AND DESIGN SOFTWARE
DEVELOPMENT**

LIM KIAN GUAN

A THESIS SUBMITTED
FOR THE DEGREE OF MASTER OF ENGINEERING
NATIONAL UNIVERSITY OF SINGAPORE

2007

**OPTICAL DISC DESIGN AND DESIGN SOFTWARE
DEVELOPMENT**

LIM KIAN GUAN

(B.SC.(HONS), UNIVERSITY OF MALAYA, MALAYSIA)

A THESIS SUBMITTED
FOR THE DEGREE OF MASTER OF ENGINEERING
NATIONAL UNIVERSITY OF SINGAPORE

2007

Acknowledgement

First, I want to thank my supervisors, Professor Chong Tow Chong and Dr Shi Luping for giving me this opportunity to work on such an interesting and challenging project. Without their support and guidance, I could not have finished this dissertation so smoothly.

Secondly, I want to thank Dr Li Jianming for helping me complete and check the writing of this dissertation and his guidance during my research.

Special thank to Dr Ong Eng Hong for helping me in grammar checking and correction of this dissertation.

Finally, I wish to thank my colleagues and friends, especially Dr Miao Xiangshui, Yang Hongxin, Chuah Chong Wei, Tan Wei Lian and Ng Hong Kee for their help during my research.

Contents

Acknowledgement.....	I
Contents	II
Abstract.....	VI
List of Tables	VII
List of Figures	IX
Chapter 1 Phase change optical discs	1
1.1 History of optical discs development	1
1.2 Phase change recording	3
1.2.1 Phase change materials	3
1.2.2 Principle of phase change recording.....	5
1.2.3 Technology for high density phase change optical discs.....	8
1.3 Disc structure of phase change optical discs.....	10
1.3.1 Structure of conventional DVD disc.....	10
1.3.2 Structure of Blu-ray Disc.....	12
1.4 Motivations of the project.....	13
1.5 Objectives.....	14
1.6 Organization of thesis.....	15
Chapter 2 Software development for an integrated optical system and disc design..	16
2.1 Introduction.....	16
2.2 Design and development of an integrate optical system and media design software (IOSMDS).....	17
2.3 Functions of IOSMDS software and implementation	19
2.3.1 Functions of optical near-field analysis and implementation.....	20
2.3.1.1 Main Interface of analysis	20

2.3.1.2 Interface of defining disc structure and material properties.....	21
2.3.1.3 Visualization of simulation results.....	25
2.3.2 Functions of thermal analysis and implementation.....	27
2.3.2.1 Main interface of analysis.....	27
2.3.2.2 Interface of defining structure and material properties....	27
2.3.2.3 Visualization of simulation results.....	30
2.4 Summary.....	31
Chapter 3 Optical system design.....	32
3.1 Working principle of the optical pick up head system.....	32
3.2 System parameters comparison for optical discs	33
3.3 Optical system design parameters consideration	34
3.4 Optical pick up head design	35
3.4.1 Objective lens design.....	35
2.4.1.1 DVD's objective lens-to-disc design.....	36
2.4.1.2 Blu-ray disc's objective lens-to-disc design.....	39
3.4.2 Optical path design -- from laser diode-to-collimator lens.....	42
3.4.3 Incident optical path design-- from optical source-to-optical disc.....	44
3.4.4 Reflected optical path design -- from beam splitter-to-detector..	45
3.4.5 Full optical path of optical pickup head design.....	46
3.5 Summary	46
Chapter 4 Fundamentals of optical and thermal analyses.....	47
4.1 Optical modeling: FDTD method.....	47
4.1.1 Generalized FDTD algorithm.....	47

4.1.2	Numerical solution	52
4.1.2.1	Updating the field components.....	52
4.1.2.2	Building the disc structure with Yee cells.....	54
4.1.2.3	Size of time step	54
4.1.2.4	Radiation boundary condition.....	54
4.1.2.5	Near field to far field transformation.....	55
4.2	Thermal modeling: FEM method.....	56
4.2.1	Initial and boundary conditions.....	59
4.2.1.1	Boundary condition at the disc surface.....	59
4.2.1.2	Initial condition.....	60
4.2.2	FEM solutions for 3D thermal conduction.....	60
4.2.2.1	Galerkin weighted residual method	60
4.2.2.2	Element chosen for thermal conduction problem.....	62
4.2.2.3	Element stiffness matrix.....	64
4.2.2.4	Global stiffness matrix.....	66
4.2.3	Solving the linear equations.....	66
4.2.4	Flow chart of finite element solution for thermal analysis.....	69
4.3	Crystallization modeling: JMA model.....	70
4.4	Summary.....	71
Chapter 5	Design of Blu-ray disc using the developed software.....	72
5.1	Optical analyses of Blu-ray disc.....	72
5.1.1	Geometry modeling of Blu-ray disc	72
5.1.2	Simulation conditions and FDTD meshing.....	73
5.1.3	The effects of black dot on Blu-ray discs.....	74
5.2	Thermal analyses of Blu-ray disc.....	78

5.2.1	Geometry modeling of Blu-ray disc.....	78
5.2.2	FEM meshing.....	79
5.2.3	Simulation conditions.....	80
5.2.4	The effects of disc tilt on thermal behavior of Blu-ray disc.....	81
5.2.5	The effects of disc thickness on thermal behavior of Blu-ray disc	89
5.2.6	The effects of surface scratches on Blu-ray disc.....	92
5.2.7	The effects of black dot on Blu-ray discs	96
5.3	Summary.....	99
Chapter 6 Conclusions.....		100
References.....		102
Publications.....		106
Appendix I.....		109
Appendix II.....		111
Appendix III.....		114
Appendix IV.....		123
Appendix V.....		128
Appendix VI.....		129
Appendix VII.....		130
Appendix VIII.....		133
Appendix IX.....		135
Appendix X.....		136
Appendix XI.....		139

Abstract

The rewrite capability has become a major requirement for optical storage today, and phase changing is the most important technology for rewritable optical disc. Optical disc design software has been used to save the time and cost for developing phase change optical disc. However, such software which is only for optical system or media analysis is inadequate for advanced optical data storage design. Software with optical system and media design capabilities is highly demanded for development of advanced optical data storage. No software has been reported based on the integration of optical system and media design. Most of the commercial optical disc design software packages available in the market mainly provide either optical system or media analysis. The advanced optical data storage design requires both optical system and media analyses be incorporated.

In this project, we have developed an integrated software package which combines both optical system and media analysis. The optical disc analysis becomes more comprehensive when both optical system design and optical media design are linked. The physical phenomena involved in high density optical system and media can be better understood which helps the design of high density optical system and disc. Moreover, the media design becomes more practical by using real optical system input from system solver through commercial software ZEMAX. This software has been used to study the influence of disc tilt, cover layer thickness, scratches and black dot on high density recording, which show that it provides a powerful tool in practical applications.

List of tables

Table 1.1	Comparison of CD-ROM, phase change and MO disc	3
Table 1.2	Phase change materials and their types of phase change	6
Table 1.3	History of phase change optical disc development	10
Table 2.1	Procedure in optical near-field and thermal analyses	20
Table 3.1	Optical disc and system parameters	34
Table 3.2	NA values of objective lens for different optical disc systems	35
Table 3.3	Data of each defined surface for DVD's objective lens-to-disc design	37
Table 3.4	Parameter definitions for even aspheric surfaces DVD's objective lens-to-disc design	37
Table 3.5	System data for DVD's objective lens-to-disc design	38
Table 3.6	Data of each defined surface for Blu-ray disc's objective lens-to-disc design	40
Table 3.7	Parameter definitions for even aspheric surfaces Blu-ray disc's objective lens-to-disc design	40
Table 3.8	System data for Blu-ray disc's objective lens-to-disc design	41
Table 3.9	Data of each defined surface for DVD's optical source-to-collimator lens design	43
Table 3.10	Parameter definitions for even aspheric surfaces DVD's optical source-to-collimator lens design	43
Table 3.11	System data for DVD's optical source-to-collimator lens design	44
Table 3.12	Parameters of each defined surface for DVD's reflected optical path design	45

Table 5.1	Optical properties of Materials	73
Table 5.2	FDTD mesh setting	74
Table 5.3	Simulation parameters	74
Table 5.4	Material properties of various layers in a Blu-ray disc	79
Table 5.5	Blu-ray disc mesh details	79
Table 5.6	Simulation conditions	80

List of figures

Figure 1.1	The history of optical discs development	1
Figure 1.2	Crystallization time of phase change material	4
Figure 1.3	Principle of phase change recording	5
Figure 1.4	Principle of phase change optical recording	7
Figure 1.5	Overwriting methods	8
Figure 1.6	Trend of multi-media application of phase change materials	9
Figure 1.7	Methods for increasing recording capacity	9
Figure 1.8	Conventional DVD disc structure	12
Figure 1.9	Blu-ray Disc structure	13
Figure 2.1	Main structure of the IOSMDS software	20
Figure 2.2	Main panel interface of optical near-field analysis	21
Figure 2.3	Material dialog box	22
Figure 2.4	Database dialog box	22
Figure 2.5	Data file formats for optical properties library	23
Figure 2.6	Disc geometry dialog box	23
Figure 2.7	Disc structure dialog box	24
Figure 2.8	Input ZEMAX beam file dialog box	25
Figure 2.9	Output file setting dialog box	25
Figure 2.10	Format of ZEMAX physical optics propagation output file	25
Figure 2.11	Near-field contour view of selected plane	26
Figure 2.12	Two dimensional plot of detected signal	26
Figure 2.13	Main panel interface of thermal analysis	27

Figure 2.14	Thermal parameters dialog box	28
Figure 2.15	Database dialog box	28
Figure 2.16	Disc geometry dialog box	28
Figure 2.17	Format of thermal data file for optical property library	29
Figure 2.18	Mesh setting dialog box	29
Figure 2.19	Mesh of a disc structure	29
Figure 2.20	Nodes numbering sequence of a finite element	29
Figure 2.21	Dialog box for defining simulation conditions	30
Figure 2.22	Temperature profile of the disc	31
Figure 2.23	Mark formation on the disc	31
Figure 2.24	Temperature along x , y , z -direction of the disc	31
Figure 2.25	Time history of temperature of the disc	31
Figure 3.1	Schematic diagram of the optical pick-up head system	33
Figure 3.2	Light spots obtained from detector	33
Figure 3.3	Definition of parameters for NA calculation	36
Figure 3.4	Three dimensional layout of DVD's objective lens-to-disc design	36
Figure 3.5	Ray aberration and optical path difference of pupil's X and Y coordinate for DVD's objective lens-to-disc design	38
Figure 3.6	Two dimensional and three dimensional plot of physical optical propagation (POP) for DVD's objective lens-to-disc design	39
Figure 3.7	Three dimensional layout of Blu-ray disc's objective lens-to-disc design	39

Figure 3.8	Ray aberration and optical path difference of pupil's X and Y coordinate for Blu-ray's objective lens-to-disc design	41
Figure 3.9	Two dimensional and three dimensional plots of physical optical propagation (POP) for Blu-ray's objective lens-to-disc design	42
Figure 3.10	Three dimensional layout of for DVD's optical source-to-collimator lens design	42
Figure 3.11	Schematic diagram of the incident optical path	44
Figure 3.12	Three dimensional layout of for DVD's reflected optical path design	45
Figure 3.13	Flow chart of optical system design	46
Figure 4.1	Disc Structure with FDTD grid	48
Figure 4.2	Unit Yee Cell in FDTD algorithm	53
Figure 4.3	Scheme to find the phase of electric field	55
Figure 4.4	Diagram of the pupil in the FFT range	56
Figure 4.5	An 8-node 3D solid brick element for thermal analysis	62
Figure 4.6	Flow chart of thermal analysis	70
Figure 5.1	Blu-ray disc structure	73
Figure 5.2	Disc model for FDTD analysis	74
Figure 5.3(a)	Beam profile of the disc without black dot	76
Figure 5.3(b)	Beam profile of disc with black dot (0.01mm offset from center of the recording track)	76
Figure 5.4	Near field intensity distribution of the mark at the center of disc without black dot	76

Figure 5.5	Near field intensity distribution of the mark at the center of disc with black dot	76
Figure 5.6	Near field intensity distribution of the disc without black dot	77
Figure 5.7	Near field intensity distribution of the disc with black dot	77
Figure 5.8	Read back signal along center track	77
Figure 5.9	Finite element model of Blu-ray disc	80
Figure 5.10(a)	OPD along pupil's Y coordinate for the disc with tangential tilt angles of 0.0° , 2.0° and 4.0°	83
Figure 5.10(b)	OPD along pupil's X coordinate for the disc with tangential tilt angles of 0.0° , 2.0° and 4.0°	83
Figure 5.11	The beam profile on Blu-ray disc with tangential tilt angles of 0.0° , 2.0° and 4.0°	84
Figure 5.12	Mark shifted with tangential tilt angles of 0.0° , 2.0° and 4.0°	85
Figure 5.13(a)	Temperature along the center track direction with tangential tilt angles of 0.0° , 2.0° and 4.0°	85
Figure 5.13(b)	Temperature along the cross track direction with tangential tilt angles of 0.0° , 2.0° and 4.0°	86
Figure 5.14(a)	OPD of Y pupil coordinate for the disc with radial tilt angles of 0.0° , 2.0° and 4.0°	86
Figure 5.14(b)	OPD of X pupil coordinate for the disc with radial tilt angles of 0.0° , 2.0° and 4.0°	87
Figure 5.15	The beam profile on the disc with radial tilt angles of 0.0° , 2.0° and 4.0°	87

Figure 5.16	Mark shifted with radial tilt angles of (a) 0.0° , (b) 2.0° and (c) 4.0°	88
Figure 5.17(a)	Temperature along the center track with radial tilt angles of 0.0° , 2.0° and 4.0°	88
Figure 5.17(b)	Temperature along the cross track direction with radial tilt angles of 0.0° , 2.0° and 4.0°	88
Figure 5.18(a)	OPD along pupil's Y coordinate for the disc with cover layer thickness of 0.1, 0.11, 0.115 and 0.12mm	89
Figure 5.18(b)	OPD along pupil's X coordinate for the disc with cover layer thicknesses of 0.1, 0.11, 0.115 and 0.12mm	90
Figure 5.19(a)	Beam profile on the disc with cover layer of thickness 0.1mm	90
Figure 5.19(b)	Beam profile on the disc with cover layer of thickness 0.11mm	90
Figure 5.19(c)	Beam profile on the disc with cover layer of thickness 0.115mm	91
Figure 5.19(d)	Beam profile on the disc of thickness 0.12mm	91
Figure 5.20	Temperature profile along the center track of the disc with cover layer of thicknesses 0.1, 0.11, 0.115 and 0.12mm	91
Figure 5.21(a)	Mark on the disc with cover layer thickness of 0.10mm	91
Figure 5.21(b)	Mark on the disc with cover layer thickness of 0.11mm	91
Figure 5.21(c)	Mark on the disc with cover layer thickness of 0.115mm	92
Figure 5.21(d)	Mark on the disc with cover layer thickness of 0.12mm	92
Figure 5.22(a)	OPD along pupil's Y coordinate for disc without scratch,	93

	with scratch and de-centered scratch	
Figure 5.22(b)	OPD along pupil's X coordinate for disc without scratch, with scratch and de-centered scratch	93
Figure 5.23(a)	Three dimensional view of optical path from the lens to the disc without scratch	94
Figure 5.23(b)	Beam profile on the disc without scratch	94
Figure 5.24(a)	Three dimensional view of optical path from the lens to the disc with scratch of area 0.8mm x 0.03mm	94
Figure 5.24(b)	Beam profile on the disc with scratch of area 0.8mm x 0.03mm	94
Figure 5.25(a)	Three dimensional view of optical path from the lens to the disc with scratch of area 0.8mm x 0.03mm and an offset of 0.01mm along cross track	94
Figure 5.25(b)	Beam profile on the disc with scratch of area 0.8mm x 0.03mm and an offset of 0.01mm along cross track	94
Figure 5.26	Temperature profile along the center track of the disc without scratch, with scratch and with de-centered scratch	95
Figure 5.27(a)	Mark on the disc without scratch	95
Figure 5.27(b)	Mark on the disc with scratch	95
Figure 5.27(c)	Mark on the disc with de-centered scratch	95
Figure 5.28(a)	OPD along pupil's Y coordinate for cover layer without black dot and with black dot	96
Figure 5.28(b)	OPD along pupil's X coordinate for cover layer without black dot and with black dot	97

Figure 5.29(a)	Three dimensional view of optical path from the lens to the disc with a black dot offset 0.01mm from center of the recording track	97
Figure 5.29(b)	Beam profile on the disc with a black dot offset 0.01mm from center of the recording track	97
Figure 5.30	Temperature profile along the center track of cover layer without black dot and with black dot	98
Figure 5.31	Mark on disc with cover layer with black dot and without black dot	98

Chapter 1 Phase change optical discs

1.1 History of optical disc development

Since the audio compact disc was commercialized in 1983[1], great progress has been made in optical storage with the introduction of Compact Disc (CD), CD-I, CD-R, DVD-Video, Digital Versatile Disc(DVD), DVD-RAM , Blu-Ray Disc (BD) and so on [2]. Figure 1.1 shows the history of optical disc development [3].

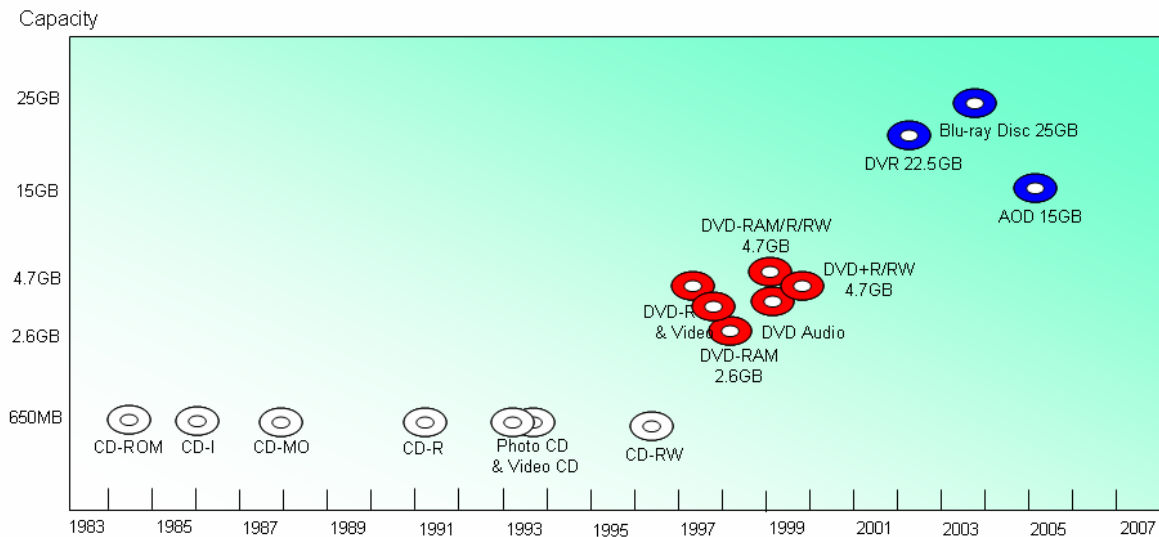


Figure 1.1 The history of optical disc development

Compared with other information storage memories, optical discs have the advantages of higher capacity, higher removability, lower cost, non-contact data retrieval using non-contact optical pick-up system and easy for large mass production. Therefore, they have been widely used as a medium to carry software, audio files, video electronic books, databases and all kinds of information distribution.

The optical discs fall into three categories: Read-Only, Recordable and Rewritable. The Read-Only discs include CD-ROM, CD-DA, VCD, DVD-Video, DVD-ROM and DVD-Audio. CD-R, DVD-R and DVD+R belong to the recordable category. The rewritable optical discs are CD-RW, DVD-RAM, DVD-RW, DVD+RW, Blu-Ray

Disc and Advanced Optical Disc (AOD). The Read-Only optical discs have the advantages of low cost and easy for mass production but the drawback is that their contents cannot be updated or modified once created. Over the years, recordable optical discs such as WORM (Write Once Read Many), CD-Recordable and DVD-R (Digital Versatile Disc Recordable) have been introduced. These formats are useful in permanent information storage applications, such as financial data, medical records, legal documentations and databases. However they cannot meet the reusable requirement, as they are cannot be updated once written. A couple of years later, rewritable optical discs overcome these problems based on Ovshinsky's invention. In 1968, Ovshinsky discovered a new memory phenomenon in chalcogenide film materials, namely the "Ovonic Memory" effect [4].

The main challenges of rewritable optical discs are the stability of reversible cycle, overwrite function and so on [5]. Phase change recoding was soon discovered to be a viable form of rewritable high-density optical data storage. Another leading contender of rewritable optical disc reading is the magneto-optic (MO) recording technique. A magneto-optic disc detects small polarization rotations of light reflected from magnetic domains, the so call Kerr effect, where phase change recoding uses differences of reflected light intensity to distinguish recorded data bits.

Although MO recoding is one of the most matured technologies at present, phase-change discs have their own attractive attributes. They have an optical head with fewer components, which simplifies alignment and installation. The magnitude of the phase-change signal is several orders higher than that of the MO media. Due to the similarity of signal detection methods, the new generation phase-change optical disc drives such as DVD-RAM are compatible with CD-ROM, CD-R, and CD-RW. For

these reasons, the phase change rewritable optical discs are becoming more popular than MO discs.

For a clear understanding of these two important recoding technologies, a comparison is made and shown in Table 1.1.

Table 1.1 Comparison of CD-ROM, phase change and MO disc

	CD-ROM	Phase-Change Optical disc	Magneto-optical disc
Read/write head	Optical head	Optical head	Optical head and magnetic head
Recording method	Emboss-Pit	Amorphous/ Crystalline states	Magnetization Reversal
Reading method	Diffraction	Optical constant change	Polarization Change
Signal detection	Reflectivity	Reflectivity	Kerr Rotation
Normalized readout signal Amplitude to CD-ROM	1	1/4	1/80

1.2 Phase change recoding

1.2.1 Phase change materials

Ge-Sb-Te system materials have both advantages: a stable amorphous state and a high crystallization speed. Ge-Sb-Te, especially GeTe-Sb₂Te₃ pseudo-binary system and its neighboring compositions have high crystallization speeds that allow them to crystallize within 100ns of laser irradiation [6] [7] [8]. The crystallization time needed for the various compositions within the GeSbTe system is presented in Figure 1.2.

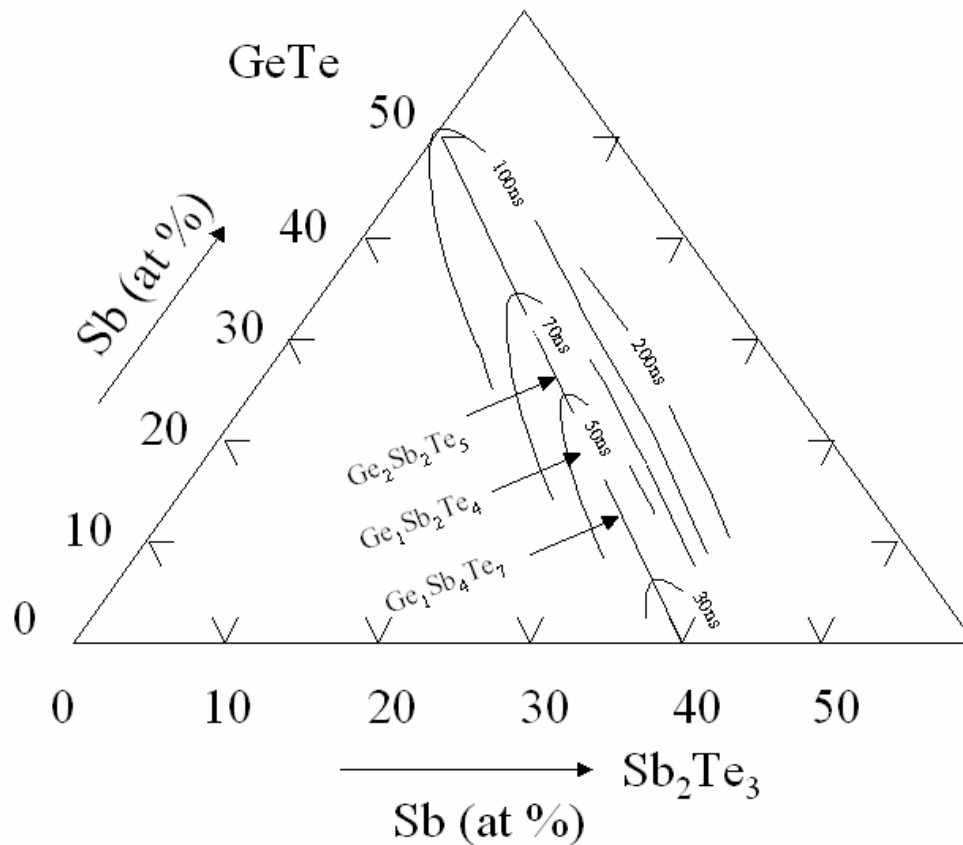


Figure 1.2 Crystallization time of phase change material

These compositions show small degradation with repeated after having been amorphized and crystallized and good overwriting characteristics. It is explained by the existence of the stoichiometric compounds such as $\text{Ge}_2\text{Sb}_2\text{Te}_5$ or GeSb_2Te_4 on the $\text{GeTe-Sb}_2\text{Te}_3$ pseudo-binary composition line, and these materials are supposed to be hard to segregate on repeated melting. It is also reported by adding with excess Sb will cause the compositions to become amorphous from crystalline more easily and vice versa, thereby giving the compositions good cyclability.

$\text{Ge}_2\text{Sb}_2\text{Te}_5$ has been selected for use in most of the commercial DVD rewritable discs, as it is one of the more commonly used phase change materials and it has been found to exhibit useful characteristics as described above.

1.2.2 Principle of phase change recording

In phase change optical discs, recording and erasing take place by the crystallographic structure changes of thin films when the films are heated by laser irradiation. Reading is done by detecting the reflectivity difference between the crystalline state and amorphous state (Figure 1.3). The reflectivity difference due to this crystallographic structure changes is typically greater than 15% [9].

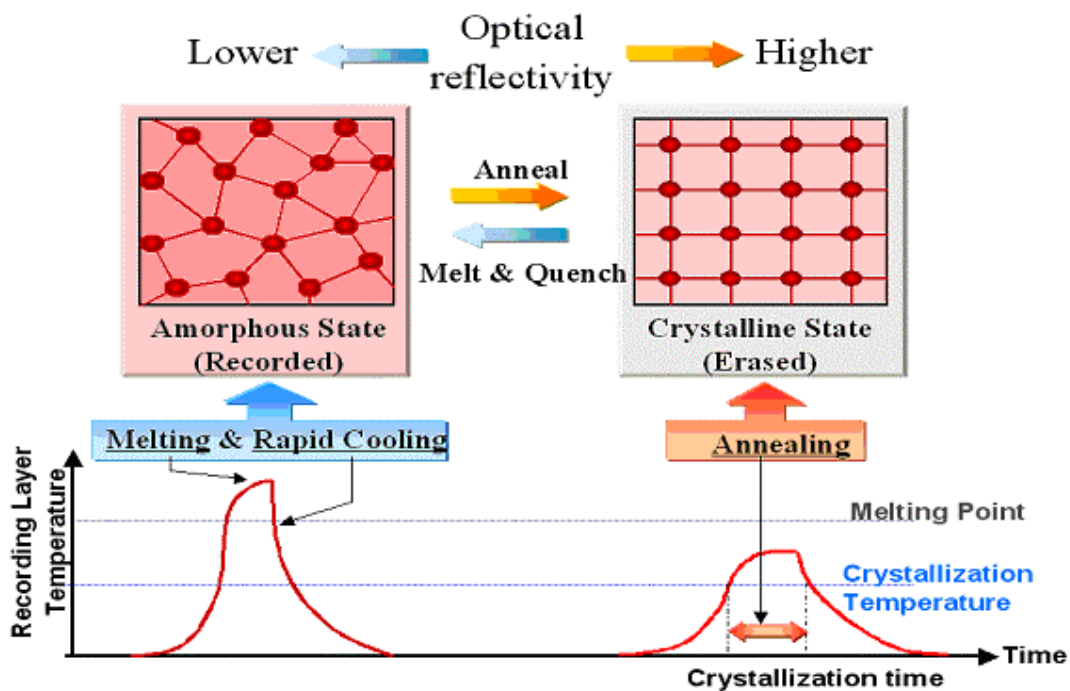


Figure 1.3 Principle of phase change recording

There are two types of phase change materials, one is irreversible when its state changes from crystalline to amorphous, and the other is reversible. The materials used to realize phase change recording is the reversible amorphous-crystalline type. Table 1.2 shows the materials that have been used in phase change recording experiment.

The amorphous state is achieved by heating the thin film over its melting point and then rapidly quenching it to room temperature. The crystalline state is formed by annealing the film at the temperature between the crystallization temperature and the

melting point of the material. The typical quenching rates required for amorphization are in the range of 10^{7-9} deg/s [6].

Table 1.2 Phase change materials and their types of phase change

Type of Phase Change	Materials
Amorphous \Rightarrow Crystalline (Irreversible)	Te-TeO ₂ , Te-TeO ₂ -Pd Bi ₂ Te ₃
Amorphous \Leftrightarrow Crystalline (Reversible)	Ge-Te, Sb-Te Ge-Te-Sb-S Te-TeO ₂ -Ge-Sn, Te-Ge-Sn-Au Ge-Te-Sn Sn-Se-Te Sb-Se-Te, Sb-Se Ga-Se-Te, Ga-Se-Te-Ge In-Se, In-Se-Tl-Co Ge-Sb-Te In-Se-Te, Ag-In-Sb-Te In-Sb-Te

To realize phase change optical recording, the thin film is required to accomplish such phase transition only by having the irradiations of the laser light converged on a spot with a diameter in the order of $1\mu\text{m}$. As shown in Figure 1.4, when a laser beam with $1\mu\text{m}$ diameter traces on the recording thin film at a linear velocity of 10m/s , irradiation time of a point on the films is only 100ns . So, all changes are required to be accomplished in this time duration. On the other hand, assuming the laser power is 10mW , the power density of the converged light spot is up to the order of 10kW/mm^2 . It is possible to shorten the time for amorphizing because the amorphization is achieved by melting and quenching the material. But the crystallization process requires a time duration determined by the physical characteristics of the material. In other words, each material has its own crystallization speed. Phase change material

used for phase change optical discs should process both amorphous state with high thermal stability and high crystallization speed which is within the order of 100ns duration or shorter [5] [10].

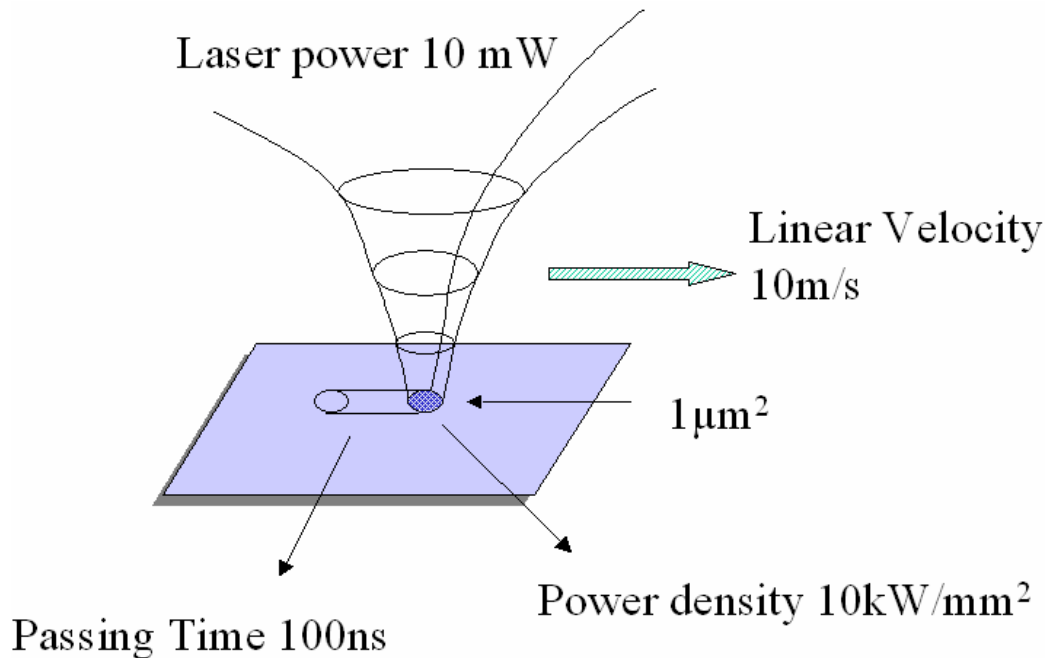


Figure 1.4 Principle of phase change optical recording

The direct overwriting is a common operation in magnetic recording. It is however an issue for optical recording, because current optical recording uses the heat mode technology. For magneto-optical discs, the magnetic field modulation method is used to solve this problem.

If a thin film material has sufficiently high crystallization speed and can be crystallized within the short traversing time of the laser beam, the direct overwriting is accomplished by laser power modulation between a peak recording power level and bias erasing level as shown in Figure 1.5 [11]. No matter the phase before overwriting is amorphous or crystalline, films irradiated with the peak recording power become amorphous, and those irradiated with bias erasing power are crystallized.

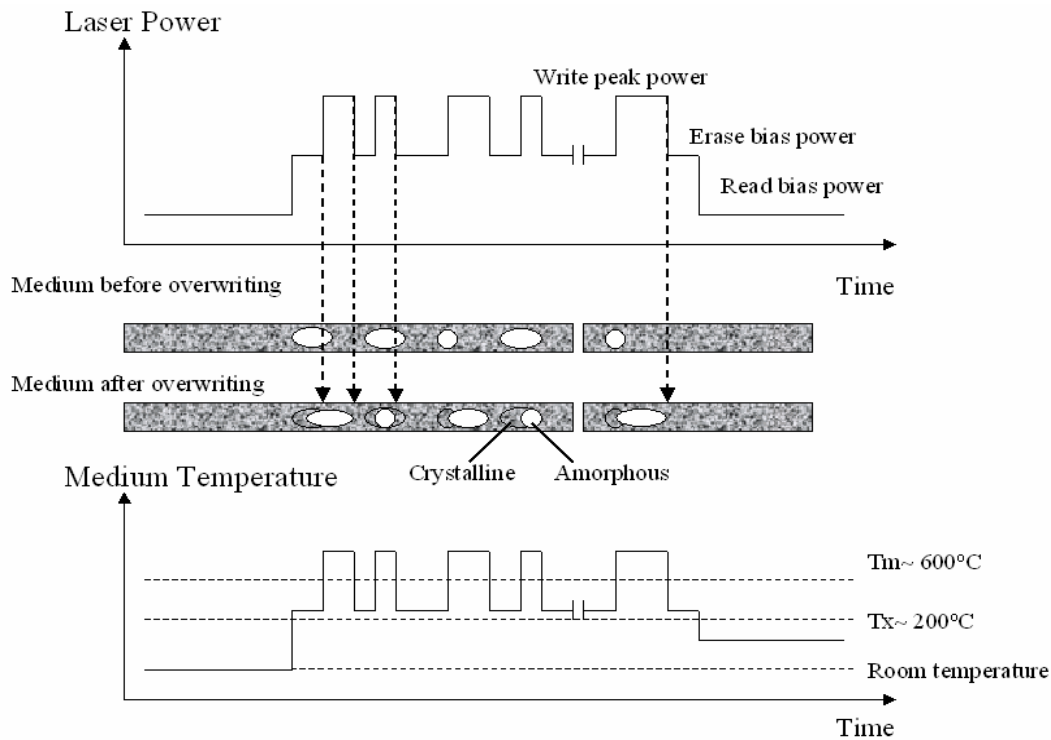


Figure 1.5 Overwriting methods

1.2.3 Technology for high density phase change optical discs

To fulfill the high quality television and movie requirements, optical discs with higher capacity and data transfer rate are needed. Figure 1.6 shows the trend for multi-media applications [3]. In order to increase the recording capacity of optical discs (Figure 1.7) [3], four basic methods can be applied: spot size reduction, data format (coding) improvement, volumetric storage exploration and disc fabrication [5][9]. To reduce the spot size, methods adopted include shortening laser wavelength ($\lambda=405\text{nm}$), increasing numerical aperture ($\text{NA}=0.85$) of objective lens and exploring near-field and super resolution technology. To improve data format, multi-level coding and error correction coding are technologies that have been studied to increase the coding efficiency. The volumetric storage includes multi-layer recording, photo-induced recording and holographic recording. In disc fabrication, high-tech mastering and land-groove structure with deep groove [12] [13] could be used to increase the disc

capacity. Based on these technologies, the Blu-ray disc (Blu-ray) and advanced optical discs (AOD) are designed. The characteristics of these optical discs are tabulated in Table 1.3.

	1997	2000	2005	2010	2015
	Video ROM 2 hrs	Video RAM 2 hrs	HDTV 4 hrs	3-D Video	Interactive 3-D Video
Capacity	4.7 GB	15GB	36GB	100GB	1TB
Transfer Rate	20 MB/s	50-100 MB/s	100-250 MB/s	1 GB/s	

Figure 1.6 Trend of multi-media application of phase change materials

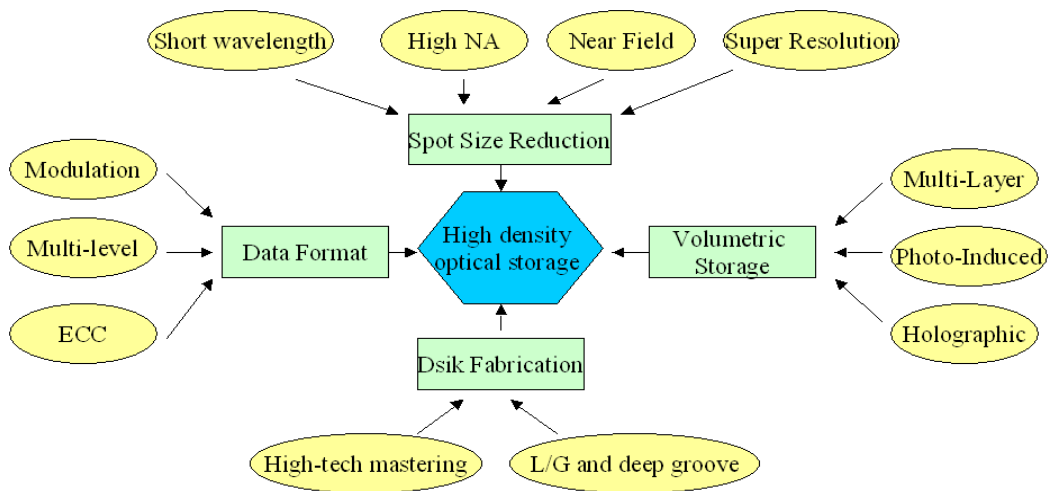
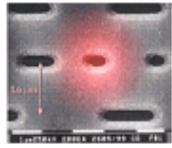
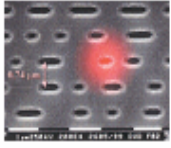
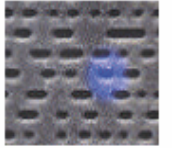
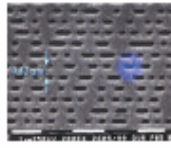


Figure 1.7 Methods for increasing recording capacity

Table 1.3 History of phase change optical disc development

	CD-RW	DVD-RAM	AOD	Blu-Ray Disk
Driving force	 Digital Audio	 Digital Video	 High Definition TV (HD TV)	 High Definition TV (HD TV)
Wavelength (nm)	780	650	405	405
NA	0.45	0.6 ~ 0.65	0.65	0.85
Capacity	0.65 ~ 0.70GB	4.7 ~ 8.5GB	15 ~ 20GB	23 ~ 27GB
Data transfer rate	1.2Mbps	11Mbps	Depend on coding	36Mbps
Writing speed at 1x	1.20 ~ 1.40m/s	3.49m/s	4.55 ~ 5.28m/s	4.55 ~ 5.28m/s

1.3 Disc structure of phase change optical discs

Reduction of spot size has serious consequences for the tolerances of the recording system [5]. The decreased tilt margin due to a higher NA is effectively compensated by applying thinner substrates or cover layer, which is obvious in development from CD(1.2mm thick substrate, NA=0.45) to DVD, AOD(0.6mm substrate, NA=0.65) and then Blu-ray Disc(0.1mm cover layer, NA=0.85). The detail of the structures of phase change optical discs will be discussed in the following sections.

1.3.1 Structure of conventional DVD disc

Figure 1.8 shows the structure of the conventional phase change DVD. Four layers of thin film are formed on the polycarbonate substrate. The phase change layer is sandwiched by dielectric protective layers made of ZnS-SiO₂, and a reflective layer made of Al alloy is attached to the dielectric layer [14]. The function of the bottom dielectric layer is to protect the substrate against humidity and thermal damage. The reflective metallic layer acts as an optical enhancement layer which enlarges the

absorption or reflection change. The dielectric layer and the reflective layer are also used to control the thermal condition during the writing and erasing processes.

In phase change optical discs, the thickness of each layer is important, because all the optical and thermo-mechanical characteristics are influenced by the layer structure, as explained below:

- 1) Optically, the recording layers require large absorption efficiency of laser light and large signal amplitude corresponding to the reflectivity difference between amorphous and crystalline states.
- 2) Thermally, not only heating efficiency but also rapid quenching conditions for amorphization are important, thus, the design should fulfill these requirements.
- 3) Mechanically, the material quality and the structure are required to endure the thermal stress caused by repeated heating and quenching cycles.

So a rapid quenching structure has been proposed to solve these issues. In this rapid quenching structure, the thin dielectric layer is used between the phase change layer and reflective layer. The thermal energy produced in the recording layer is rapidly diffused in this structure and it causes smaller damage to the other layers [14].

It was reported that a million cycles of overwriting have been achieved by using this kind of disc structure [16]. From the accelerated aging test, the lifetime has been estimated to be longer than 60 years in an environment of 32°C temperature and 80% relative humidity, which is sufficiently long for commercial development [17].

The ZnS-SiO₂ thin film material for dielectric protective layer is made of a mixture of small grains of ZnS and SiO₂. ZnS is a suitable material for phase change optical disc because it has a high refractive index of 2.4 and a melting point of 1700°C. Adding SiO₂ to ZnS makes amorphous-like structure decrease its internal stress.

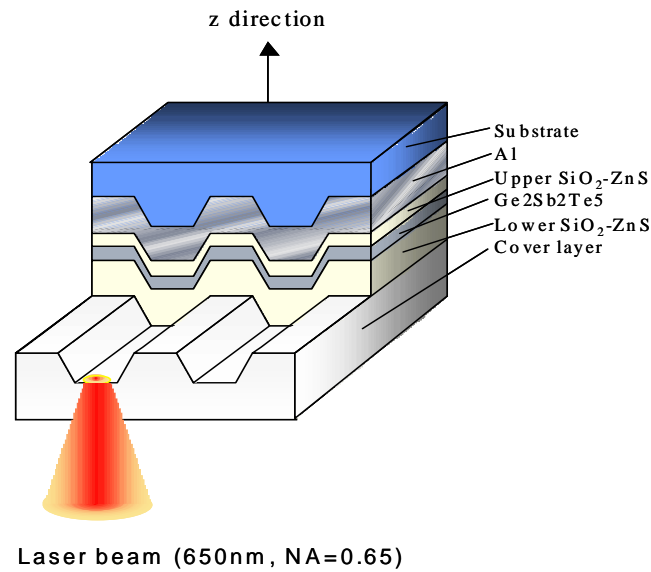


Figure 1.8 Conventional DVD disc structure

1.3.2 Structure of the Blu-ray disc

Figure 1.9 shows the structure of a Blu-ray Disc. The structure of the Blu-ray Disc is different from that of the DVD. In order to make data processing occur near to the laser head, the substrate is made thicker (1.1mm) while the cover layer is made thinner (0.1mm), and the laser irradiates from the cover layer. It can be seen that the Blu-ray disc system is not compatible with the DVD system. A new optical disc drive has been designed specially for Blu-ray Discs by Sony, Philips, Hitachi, Sharp, Samsung and others.

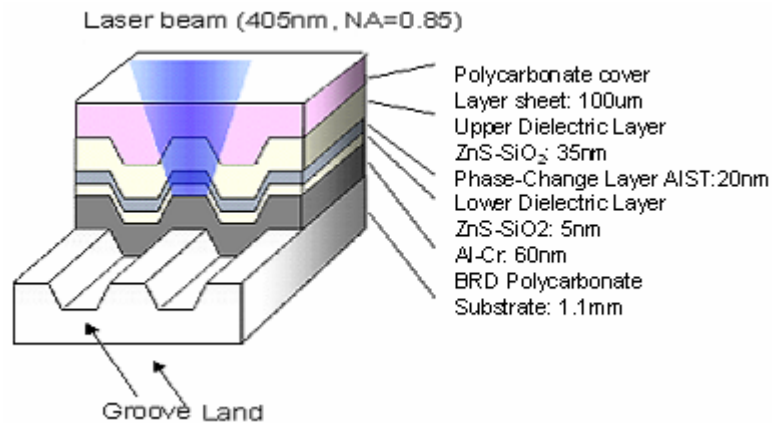


Figure 1.9 Blu-ray Disc structure

1.4 Motivation of the project

In order to increase the capacity of optical storage through an optical system; both shorter wavelength and high numerical aperture (NA) optical system have been applied. When mark sizes become smaller and smaller due to shorter wavelength and high NA optical pick-up (OPU), any slight tilt of disc or defects in optical pick-up will affect the performance of writing and reading [18]. Optical drive with high perform write capability becomes a major requirement for optical storage today. It will strongly affect the performance of optical media. Optical disc design software which is only for optical system or media analysis is inadequate for advanced optical data storage design. Software with optical system and media design capabilities is highly demanded for development of advanced optical data storage system and media. However, most of the commercial optical disc design software packages available in the market mainly provide either optical performance analyses or media analyses. The advanced optical data storage design requires that the complete optical system as well as optical and thermal analyses of the disc be taken into consideration.

In this project, we have developed an integrated software package which combines both optical system and media analysis. The optical disc analyses become more

comprehensive and accurate when both optical system design and optical media design are linked. The physical phenomena involved in high density optical system and media can be better understood and helps the design of high density optical system and media. Moreover, the media design becomes more practical when using real optical system input. This software has been used to study the effect of disc tilt, cover layer thickness, scratches and black dot on cover layer surface for high density recording and these studies indicating clearly that it is a useful and practical tool.

1.5 Objectives

The objectives of the project are as follows:

- 1) To develop an integrated software which combines both optical and media analysis and design for high density and high speed optical discs.
- 2) To develop the finite element thermal modeling and analysis simulator for advanced optical discs design.
- 3) To develop the finite difference time domain near field optic modeling and analysis simulator for advanced optical discs design.
- 4) To use the developed software to analyze and study the influence of disc tilt, cover layer thickness, scratches and black dot on cover layer surface on high density recording.
- 5) To use the developed software to analyze and study the relationship of optical path with a mark formation and thermal distribution.

1.6 Organization of the thesis

This thesis is organized as follows:

Chapter 1 gives the history and the introduction of optical discs.

Chapter 2 describes the software development of integrated software.

Chapter 3 describes the principle of optical system design and the optical system design using the optical solver “ZEMAX”.

Chapter 4 illustrates optical near field modeling and analysis using finite difference time domain method, as well as thermal modeling and the finite element solution for the design of phase change optical discs.

Chapter 5 focuses on the discussion of the results obtained from using the developed software.

Conclusions are then drawn in Chapter 6.

Chapter 2 Software development for an integrated optical system and disc design

2.1 Introduction

The optical data storage industry is very competitive and it is very challenging for a company to stay viable. To produce low cost and short time-to-market optical drives and discs is the key for optical storage companies to remain competitive in the market. Capabilities to standardize or patent new advanced storage methods will allow the optical storage companies to shorten their product development time and launch their new products before their competitors do. To realize the goal of designing better products with lower cost and shorter development time, computer aided design (CAD) is a good solution popular with players in the industry.

There are many studies that many address the numerical techniques for computer aided design and simulations of the optical discs and storage system. These simulation tools mainly fall into three categories. The first one is specific for optical system designs and analyses, such as code V and ZEMAX which are available commercially. The second type deals with the performance analyses of optical discs, such as DIFFRACT. The third type focuses on the thermal analyses of optical discs, multi-physics commercial software ANSYS (based on finite element method) may be used in the design and analysis of optical discs [19]. However, this software is not designed specially for phase change optical discs. The analysis of such discs with ANSYS is time consuming. Moreover, some complicated processes like the amorphization and crystallization processes of the phase change phenomenon cannot be easily simulated.

H. Kando et al [20] have developed a mark simulator for phase change optical discs. With this simulator, the time-dependent temperature distribution in 3-dimensional structure is analyzed by solving the heat conduction equation based on finite difference method (FDM). But, the simulator is not suitable for handling complicated geometry, such as one with a land and groove structure.

In practice, optical systems and discs are interdependent. Optical disc design software which is only based on optical performance or media analysis is inadequate for the design of advanced optical data storage system. Software with optical systems and media design capabilities is thus high demand. However, most of the commercial optical disc design software packages available in the market mainly provide either optical performance analyses or media analyses. The advanced optical data storage system design requires both optical system and disc performance analyses. The optical disc analyses become more comprehensive when both optical system design and optical media design are integrated. The physical phenomena involved in high density optical storage system can then be better understood. In addition, the media design becomes more practical when one uses real optical system inputs from the optical system design software.

2.2 Design and development of an integrated optical system and media design software (IOSMDS)

Integration of optical system and media design software (IOSMDS) is developed in this project. The IOSMDS is run on Microsoft Windows 95/98/NT/XP based operating system. The hardware requirements are Intel Pentium II 450MHz class CPU or better, with 256MB of RAM and a 5GB hard disc space. The IOSMDS allows users to freely design or modify the optical disc with multi-layer structure, as well as

land or groove structures. There is no limit on the number of layers to be included and the land and groove structures can be freely modified. A resource data library is included for the commonly used and prospective materials with their optical and thermal properties, where the properties are obtained from the public domain as well as in-house experiments. Beside in-built library, users may also specify the properties for new materials and add to the data library. To save time, this software provides a function to calculate alloy materials' optical indices, based on the Effective Media Approximation Theory [21]. With this function, the alloy's optical index can be adjusted by changing the compositions of materials in order to optimize the optical performance of the disc.

After designing the optical disc structure, the software can calculate the disc reflectivity, modulation amplitude, cross-talk, track error signal, eye-patterns and so on. The above analyses are calculated by using the scalar method. An alternative, finite-difference time-domain (FDTD) method is also available for near-field optical analyses.

The thermal analyses in 3-dimensional optical discs are simulated based on FEM. The big advantages of FEM are its abilities to handle truly arbitrary geometry and to deal with general boundary conditions. FEM is also well adapted to the cases when geometrical deformation may be resulted from the physical process of heating. FEM is thus an effective and reliable approach to solving heat transfer problems with high level of temperature gradient extremity. The interactive graphical user interface of the software allows users to specify the parameters involved conveniently, such as rotation speed of disc, laser power, laser pulse waveform, thermal convection and so on.

With FEM, the transient thermal state and thermal expansion process of the disc resulting from single pulse, multiple pulses or any combination of them can be simulated and analyzed. All the results can be graphically displayed, including temperature distribution profiles, temperature contour displays, heating and cooling rates, heat flux distribution profiles, displacement profile, displacement contour distribution, stress, strain, animation of time dependent temperature and displacement distribution and other useful information.

2.3 Functions of IOSMDS and implementation

The main structure and features of IOSMDS are shown in Figure 2.1. The design and analyses can split into two parts, namely optical near-field analysis and thermal analysis. The steps involved in the optical near-field and thermal modeling are listed in Table 2.1. The objectives of IOSMDS are to simplify the entire design process of optical disc as much as possible and to allow for maximum design flexibility. Therefore any optical disc designer without any FEM or FDTD knowledge can use this software easily to design optical discs and analyse the optical and thermal performance of their designs. The interface of the software has also been designed such that it is easy to use for Window users.

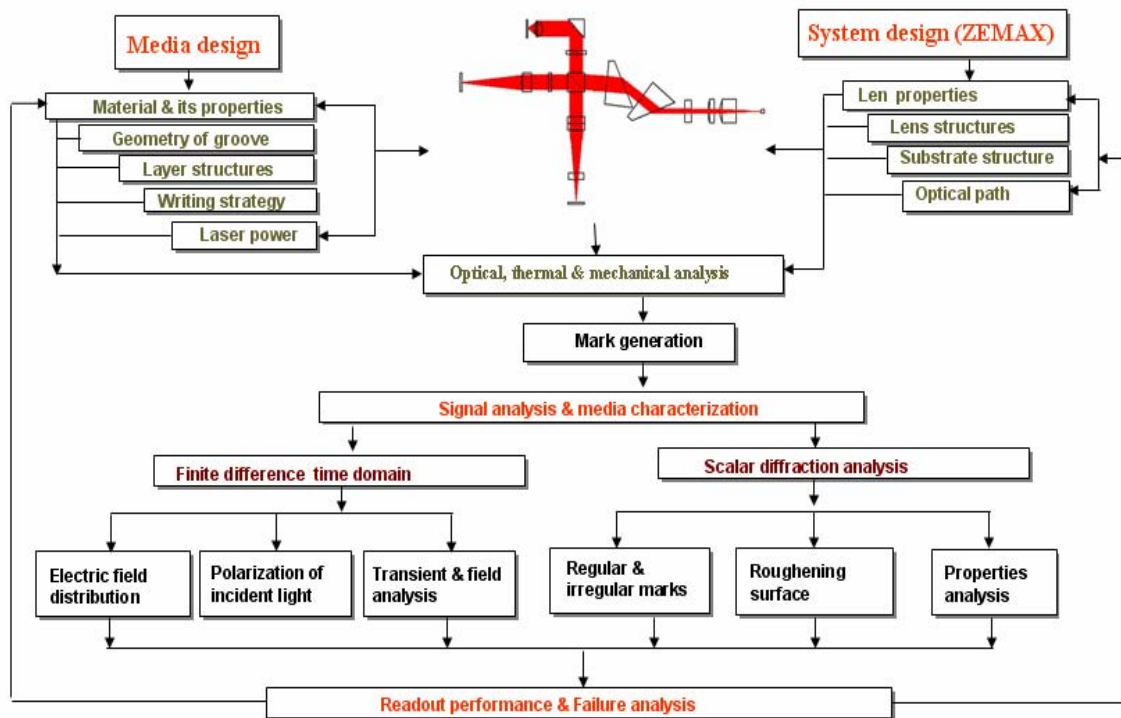


Figure 2.1 Main structure of the IOSMDS software

Table 2.1 Procedure in optical near-field and thermal analyses

Process	Optical near-field analysis	Thermal analysis
Pre-process	1) Disc geometry and material properties 2) Structure meshing for FDTD modeling	1) Disc geometry and material properties 2) Structure meshing for FEM modeling
Solver	3) Apply loads, boundary conditions and initial conditions 4) FDTD solver	3) Apply loads, boundary conditions and initial conditions 4) FEM solver
Post-process	5) Visualization and analysis of results	5) Visualization and analysis of results

2.3.1 Functions of optical near-field analysis and implementation

2.3.1.1 Main Interface of analysis

Figure 2.2 shows the main panel interface of optical near-field analysis. The main panel consists of three dimension structure view and view control bar. The disc structure designed by users will be displayed on the three dimension structure view. The view control bar is used to load and display the results file from simulation, also used to choose view paths and start or stop animation.

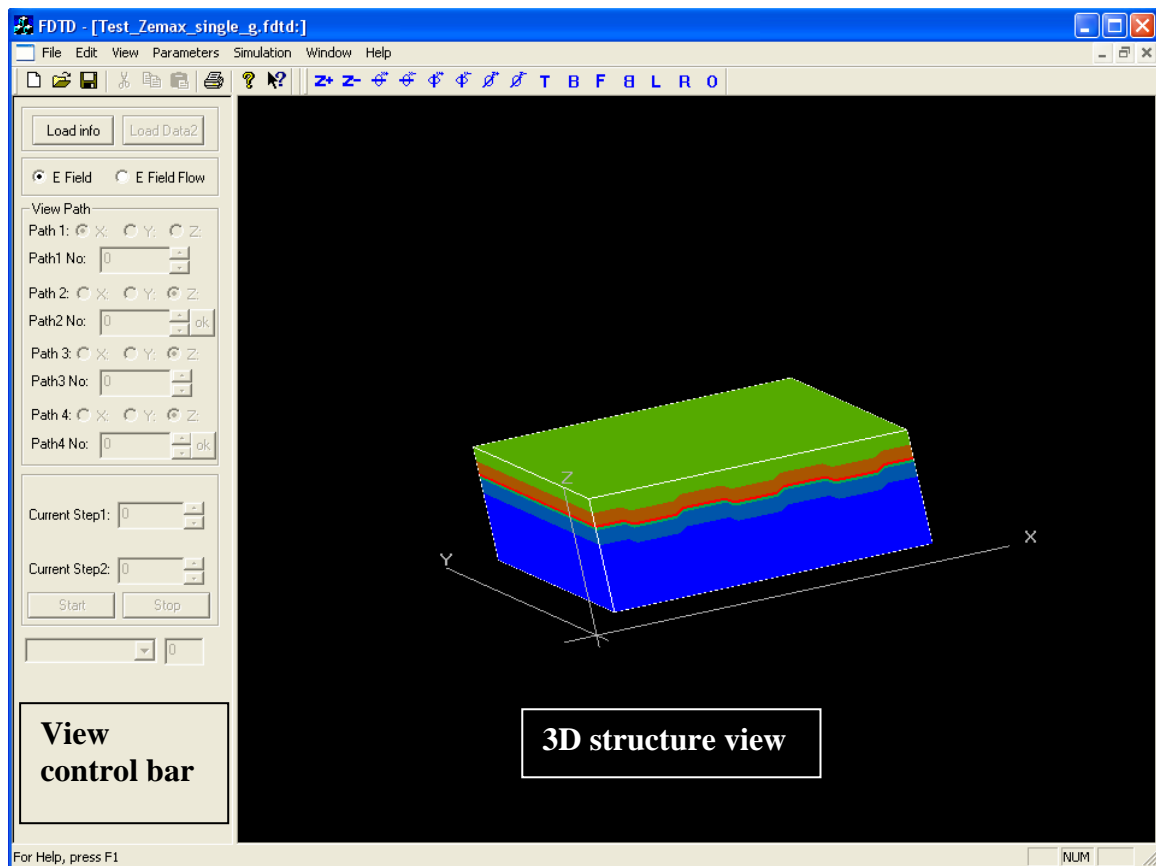


Figure 2.2 Main panel interface of optical near-field analysis

2.3.1.2 Interface of defining disc structure and material properties

Before constructing the disc structure, the material information is entered in the material dialog box as shown in Figure 2.3. The material properties can be entered by hand or loaded from the material library. The important C codes of material dialog box are listed in Appendix I. Figure 2.4 shows the database dialog box. The retrieve optical data files function codes of database dialog box is shown in Appendix II. The key feature of this retrieve function is that the program will automatically search the optical parameters according to the input wavelength. The data file format for optical properties library of phase-change materials and non phase-change materials are shown in Figure 2.5. With this feature, user can use this file format to add new materials information to the material library. Figure 2.6 depicts the disc geometry dialog box whereas Figure 2.7 shows the disc structure dialog box. After having

defined all material parameters, the disc geometry can be defined in the disc geometry dialog box and information of each layer and mesh size of element can be entered in the disc structure dialog box. The implementation for X-Z plane view in the disc structure dialog box in C code is shown in Appendix III. The purpose of X-Z plane view is to make the input function more interactive.

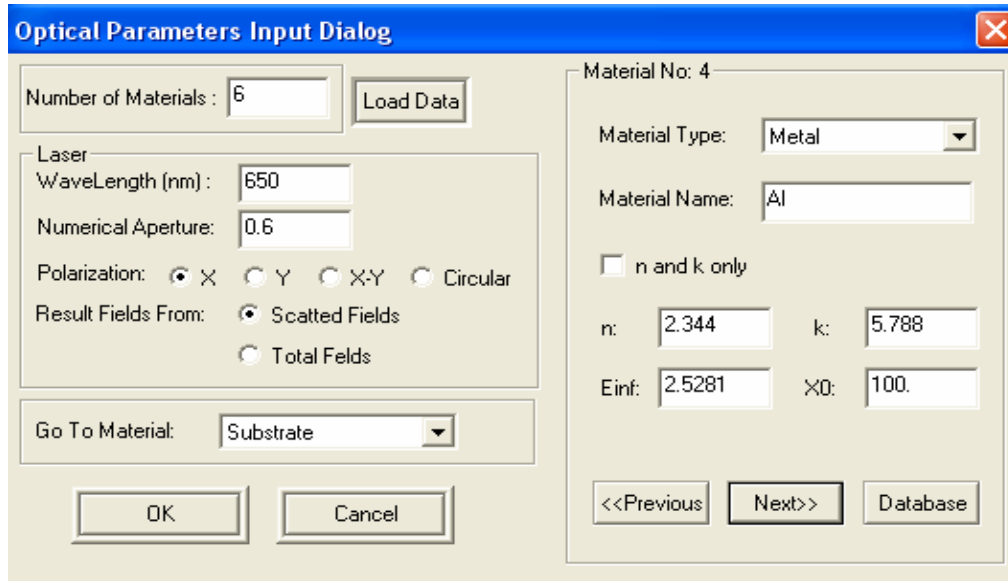


Figure 2.3 Material dialog box

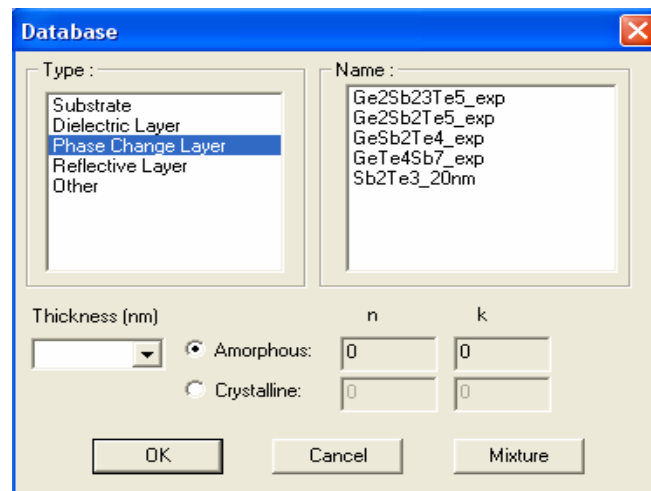


Figure 2.4 Database dialog box

Optical data file of phase-change material

	1st thickness (nm)	2nd thickness (nm)	3rd thickness (nm)	End of thickness list
Line 1	15	18	20	-1
Line 2	350 1.967 2.825 1.533 3.17	1.888 2.688 1.427 3.066	1.882 2.616 1.364 3.006	
-----	355 2.002 2.869 1.493 3.271	1.936 2.724 1.449 3.134	1.908 2.652 1.39 3.072	
-----	360 2.03 2.929 1.586 3.323	1.956 2.774 1.494 3.198	1.929 2.692 1.411 3.137	
-----	365 2.074 3.013 1.644 3.422	1.983 2.839 1.528 3.282	1.967 2.744 1.456 3.21	
Line n	370 2.148 3.108 1.735 3.516	2.049 2.912 1.586 3.37	2.006 2.813 1.506 3.289	

Labels for Figure 2.5 (top):
 Wave length (nm) points to the first column.
 n of amorphous state points to the second column.
 k of amorphous state points to the third column.
 n of crystalline state points to the fourth column.
 k of crystalline state points to the fifth column.

Optical data file of non phase-change material

	End of thickness list	n value	k value
Line 1	-1	2.273	0
Line 2	410	2.267	0
-----	415	2.261	0
-----	420	2.261	0
Line n	425	2.256	0

Labels for Figure 2.5 (bottom):
 Wave length (nm) points to the first column.
 n value points to the second column.
 k value points to the third column.

Figure 2.5 Data file format for optical properties library

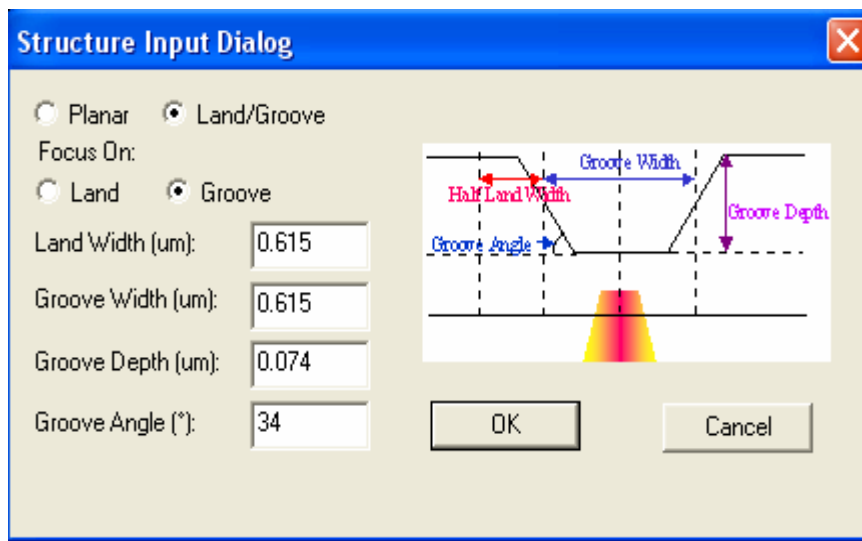


Figure 2.6 Disc geometry dialog box

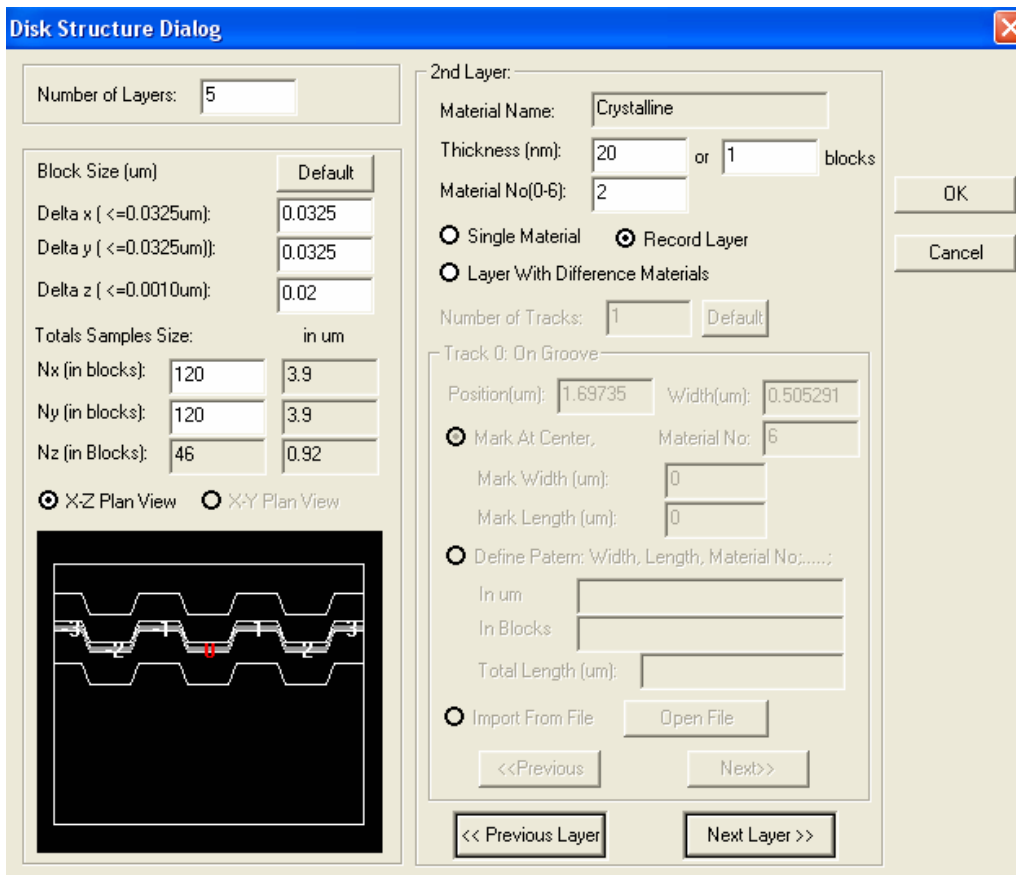


Figure 2.7 Disc structure dialog box

The laser beam profile used in the optical simulator can either be obtained from optical system solver through input beam file dialog box or one can use the default Gaussian beam profile from the simulator. Figure 2.8 shows the import beam file dialog box. All the output data and interactive cycles can be set in the output file setting dialog box shown in Figure 2.9. The file output file from the optical system solver, Physical Optics Propagation (POP), is shown in Figure 2.10. The source codes for reading optical system solver POP file are shown in Appendix IV.

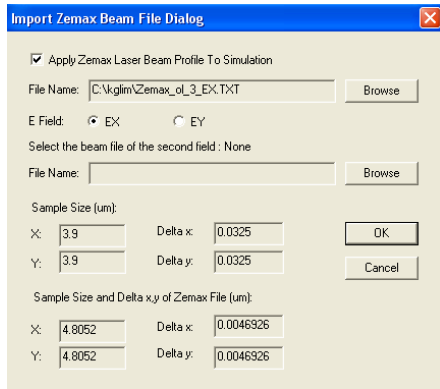


Figure 2.8 Input ZEMAX beam file dialog box

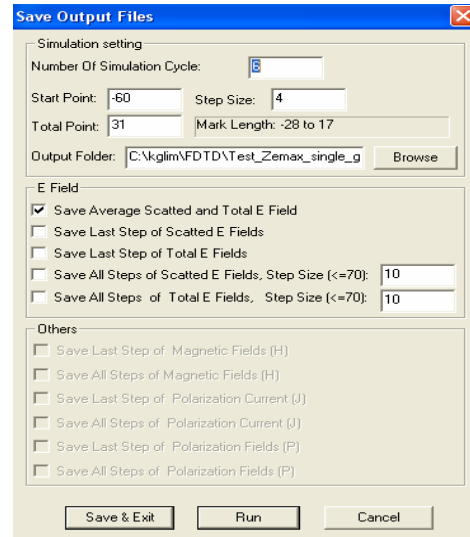


Figure 2.9 Output file setting dialog box

Listing of POP Irradiance Data

File : F:\MEng run\Blue Tilted\Blu-ray_new.ZMX
 Title: Lens has no title.
 Date : MON JAN 1 2007

Total Irradiance surface 5
 Grid size (X by Y): 512 by 512
 Point spacing (X by Y): 3.8952E-006 by 3.8952E-006 Millimeters
 Wavelength 0.4050 microns at 0.0000 deg
 Display X Width = 1.9943E-003, Y Height = 1.9943E-003 Millimeters
 Peak Irradiance = 6.9325E+005 Watts/Millimeters^2, Total Power = 3.9051E-001 Watts
 Pilot: Size= 6.22281E-004, Waist= 4.95952E-004, Pos= -2.28440E-003, Rayleigh= 3.01436E-003

2.470357E+002	2.471881E+002	2.476903E+002	2.484859E+002	2.497201E+002	2.512561E+002	2.531484E+002	2.554270E+002	2.580978E+002
2.471881E+002	2.473404E+002	2.478426E+002	2.486382E+002	2.498723E+002	2.514082E+002	2.533004E+002	2.555790E+002	2.582497E+002
2.476903E+002	2.478426E+002	2.483449E+002	2.491405E+002	2.503749E+002	2.519111E+002	2.538036E+002	2.560828E+002	2.587543E+002
2.484859E+002	2.486382E+002	2.491405E+002	2.499362E+002	2.511709E+002	2.527074E+002	2.546004E+002	2.568804E+002	2.595531E+002
2.497201E+002	2.498723E+002	2.503749E+002	2.511709E+002	2.524065E+002	2.539440E+002	2.558382E+002	2.581202E+002	2.607952E+002
2.512561E+002	2.514082E+002	2.519111E+002	2.527074E+002	2.539440E+002	2.554824E+002	2.573780E+002	2.596621E+002	2.623400E+002
2.531484E+002	2.533004E+002	2.538036E+002	2.546004E+002	2.558382E+002	2.573780E+002	2.592754E+002	2.615623E+002	2.642438E+002
2.554270E+002	2.555790E+002	2.560828E+002	2.568804E+002	2.581202E+002	2.596621E+002	2.615623E+002	2.638535E+002	2.665403E+002
2.580978E+002	2.582497E+002	2.587543E+002	2.595531E+002	2.607952E+002	2.623400E+002	2.642438E+002	2.665403E+002	2.692340E+002
2.610524E+002	2.612042E+002	2.617095E+002	2.625094E+002	2.637540E+002	2.653016E+002	2.672090E+002	2.695111E+002	2.722119E+002
2.642759E+002	2.644275E+002	2.649335E+002	2.657342E+002	2.669812E+002	2.685312E+002	2.704420E+002	2.727493E+002	2.754569E+002
2.677183E+002	2.678696E+002	2.683761E+002	2.691773E+002	2.704261E+002	2.719781E+002	2.738915E+002	2.762034E+002	2.789171E+002
2.714858E+002	2.716368E+002	2.721438E+002	2.729457E+002	2.741967E+002	2.757509E+002	2.776673E+002	2.799845E+002	2.827051E+002
2.754732E+002	2.756238E+002	2.761313E+002	2.769336E+002	2.781864E+002	2.797424E+002	2.816615E+002	2.839866E+002	2.867108E+002
2.796398E+002	2.797900E+002	2.802976E+002	2.811000E+002	2.823544E+002	2.839119E+002	2.858331E+002	2.881596E+002	2.908931E+002
2.841153E+002	2.842649E+002	2.847727E+002	2.855752E+002	2.868312E+002	2.883902E+002	2.903136E+002	2.926449E+002	2.953850E+002
2.888197E+002	2.889687E+002	2.894767E+002	2.902791E+002	2.915366E+002	2.930968E+002	2.950222E+002	2.973582E+002	3.001050E+002
2.936907E+002	2.938390E+002	2.943469E+002	2.951489E+002	2.964075E+002	2.979685E+002	2.998953E+002	3.022354E+002	3.049884E+002
2.988466E+002	2.989940E+002	2.995019E+002	3.003034E+002	3.015631E+002	3.031248E+002	3.050531E+002	3.073975E+002	3.101569E+002

Figure 2.10 Format of ZEMAX physical optics propagation output file

2.3.1.3 Visualization of simulation results

The results of optical analysis can be visualized as two dimensional contour displays for near-field analysis and detected signal plot. Beside visualization, the simulation data can also be extracted as in ASCII, which is a common file format. The output file format can then be exported to commercial spreadsheet software like Excel for analysis. Figure 2.11 and Figure 2.12 show near-field contour view of a selected plane of a disc and the two dimensional plot of detected signal from the results of optical

analysis, respectively. A section of source codes for two dimensional contour display and detected signal plot are shown in Appendix V and Appendix VI, respectively.

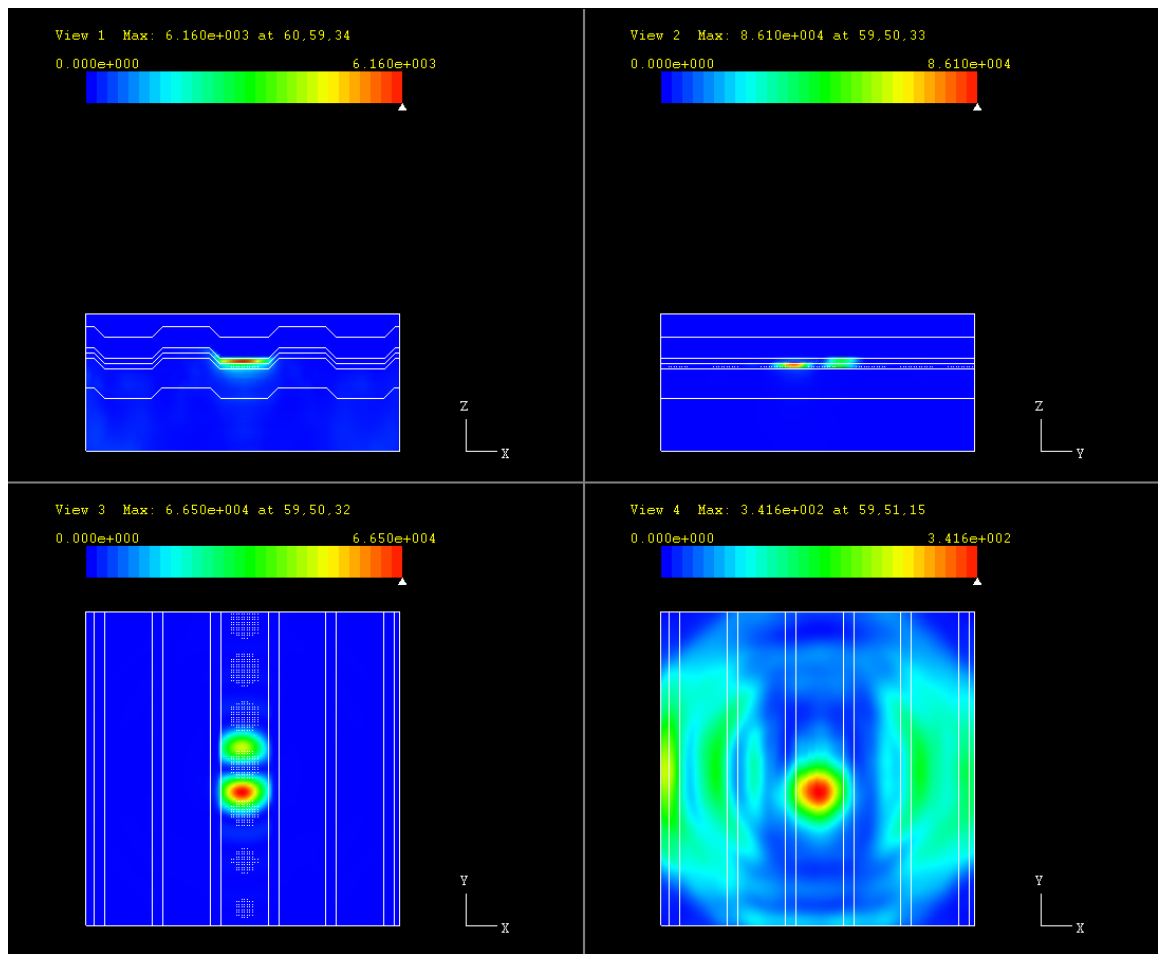


Figure 2.11 Near-field contour view of selected plane

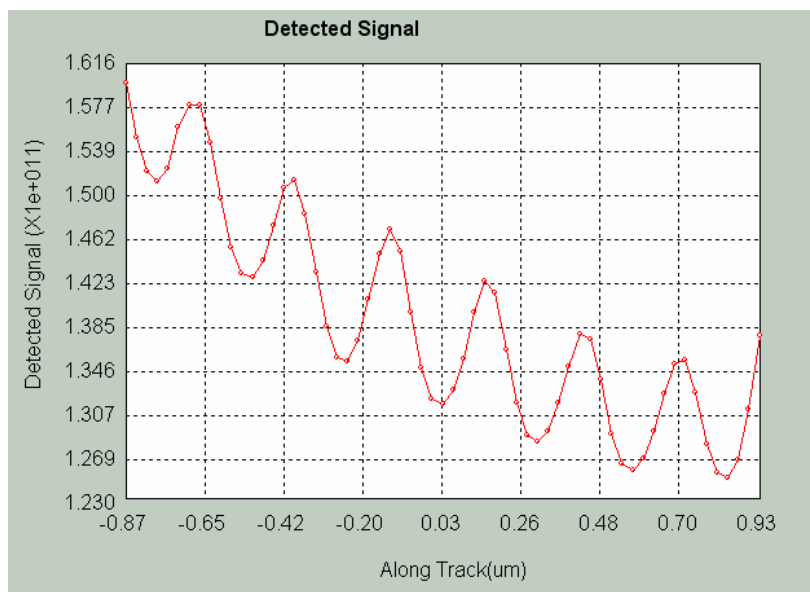


Figure 2.12 Two dimensional plot of detected signal

2.3.2 Functions of thermal analysis and implementation

2.3.2.1 Main interface of analysis

Figure 2.13 shows the main panel interface of thermal analysis. The main panel consists of three dimensional pre-process or post-process view and view control bar. The three dimensional pre-process or post-process view is used to display disc structure, temperature distribution and mark formation. The view control bar is implemented to rotate, zoom, move, start or stop animation of the three dimensions view.

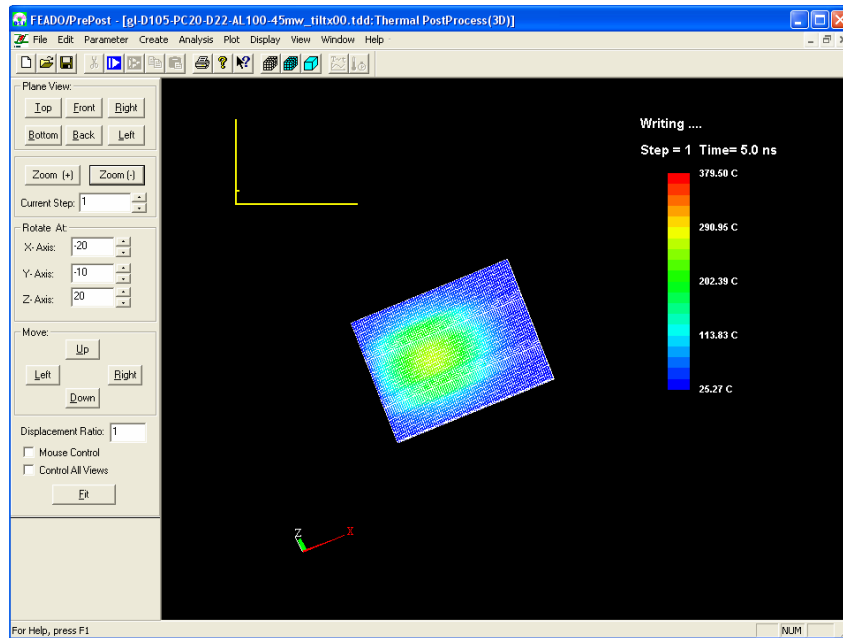


Figure 2.13 Main panel interface of thermal analysis

2.3.2.2 Interface of defining structure and material properties

Similar to optical analysis, the material properties and disc geometry are defined in the thermal parameters dialog box and the disc geometry dialog box, respectively. The material properties can also be loaded from the library. Figures 2.14, 2.15 and 2.16 show the thermal parameters dialog box, database dialog box and disc geometry dialog box, respectively. The source codes of main sections of thermal parameters dialog box and database dialog box are shown in Appendix VII and Appendix VIII,

respectively. Figure 2.17 shows the format of data file for the thermal properties library. After having defined the disc geometry and all others parameters, the FEM meshing of the disc structure is generated. The meshing setting dialog box is shown in Figure 2.18 and the disc structure after meshing is shown in Figure 2.19. A section of the implementation codes for meshing setting dialog box is shown in Appendix IX. For the FEM mesh, 8 node brick elements have been chosen in our FEM model. The numbering sequences of an 8 node brick element is shown in Figure 2.20.

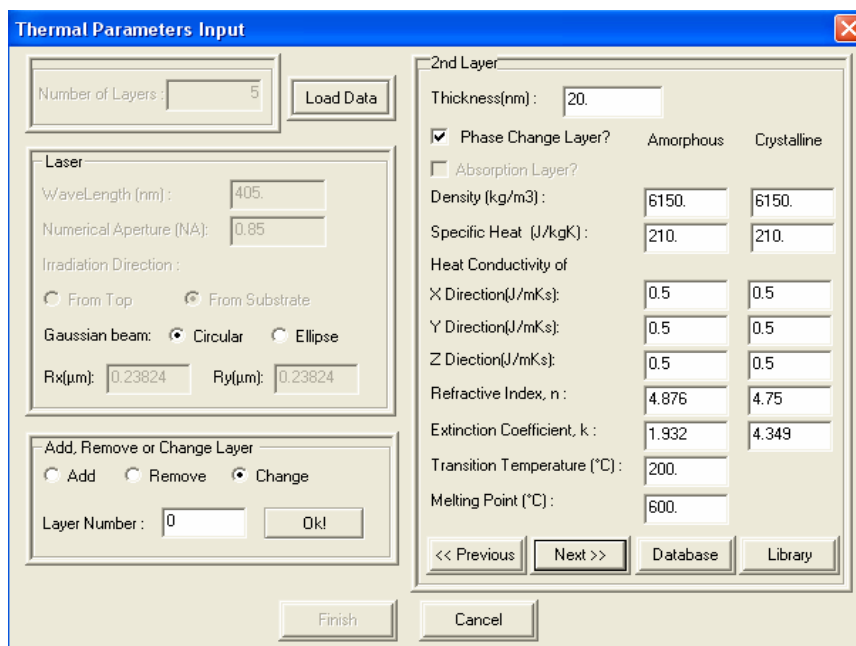


Figure 2.14 Thermal parameters dialog box

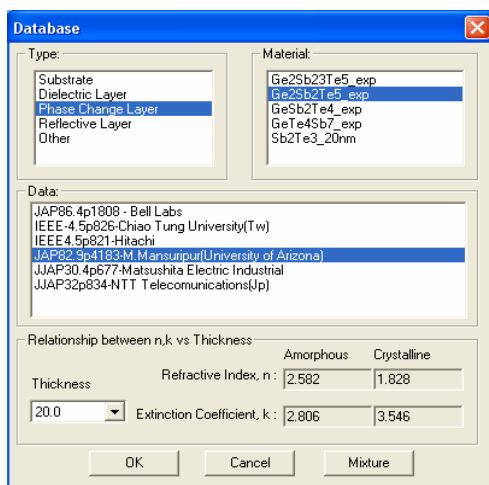


Figure 2.15 Database dialog box

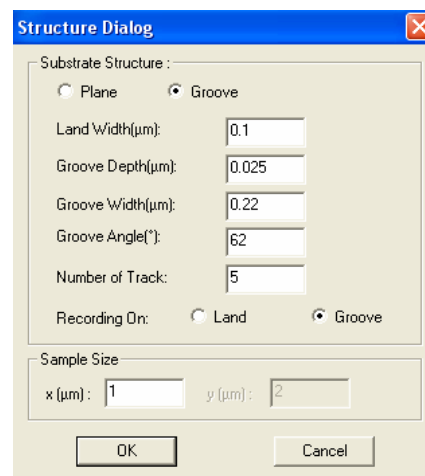


Figure 2.16 Disc geometry dialog box

Thermal data file of phase-change material

	Reference source	Heat conductivity ($Jm^{-1}K^{-1}s^{-1}$)	Specific heat ($Jkg^{-1}K^{-1}$)	Density (kgm^{-3})	Melting point ($^{\circ}C$)	Transition temperature ($^{\circ}C$)
Reference 1	JAP86.4p1808 - Bell Labs;	0.582	210	6150	600	200
Reference 2	IEEE-4.5p826-Chiao Tung University(Tw);	0.582	210	6150	600	200
-----	IEEE4.5p821-Hitachi;	0.58	210	6150	600	200
-----	JAP82.9p4183-M.Mansuripur(University of Arizona);		0.5	210	6150	600 200
-----	JJAP30.4p677-Matsushita Electric Industrial;		0.584	210	6150	600 200
Reference n	JJAP32p834-NTT Telecommunications(Jp);	0.462	210	6150	600	200

Thermal data file of non phase-change material

	Reference source	Heat conductivity ($Jm^{-1}K^{-1}s^{-1}$)	Specific heat ($Jkg^{-1}K^{-1}$)	Density (kgm^{-3})
Reference 1	JAP86.4p1808 - Bell Labs;	0.657	560	3650
Reference 2	IEEE-4.5p826-Chiao Tung University(Tw);	0.657	560	3650
-----	IEEE4.5p821-Hitachi;	0.628	560	3650
-----	JAP82.9p4183-M.Mansuripur(University of Arizona);		0.6	560 3650
-----	JJAP30.4p677-Matsushita Electric Industrial;		0.659	560 3650
Reference n	JJAP32p834-NTT Telecommunications(Jp);	2.604	560	3650

Figure 2.17 Format of thermal data file for optical property library

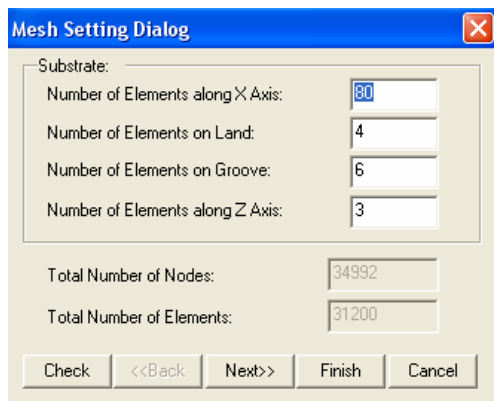


Figure 2.18 Mesh setting dialog box

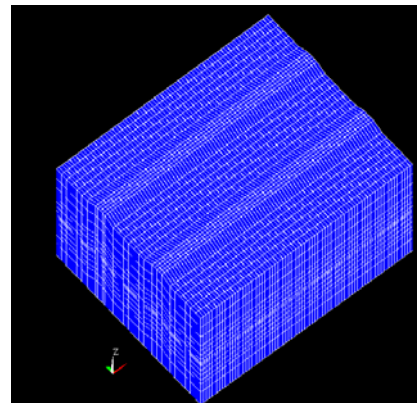


Figure 2.19 Mesh of a disc structure

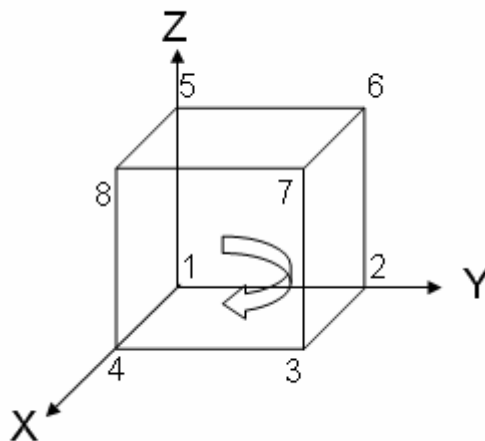


Figure 2.20 Nodes numbering sequence of a finite element

The applied pulse waveform, laser beam profile, initial conditions, boundary conditions, laser start position, laser velocity and time step are defined in the dialog box for defining simulation conditions which is shown in Figure 2.21. The solver will start when the “run solver” button is clicked. A section of the implemented source codes of pulse shape view for dialog box for defining simulation conditions are shown in Appendix X.

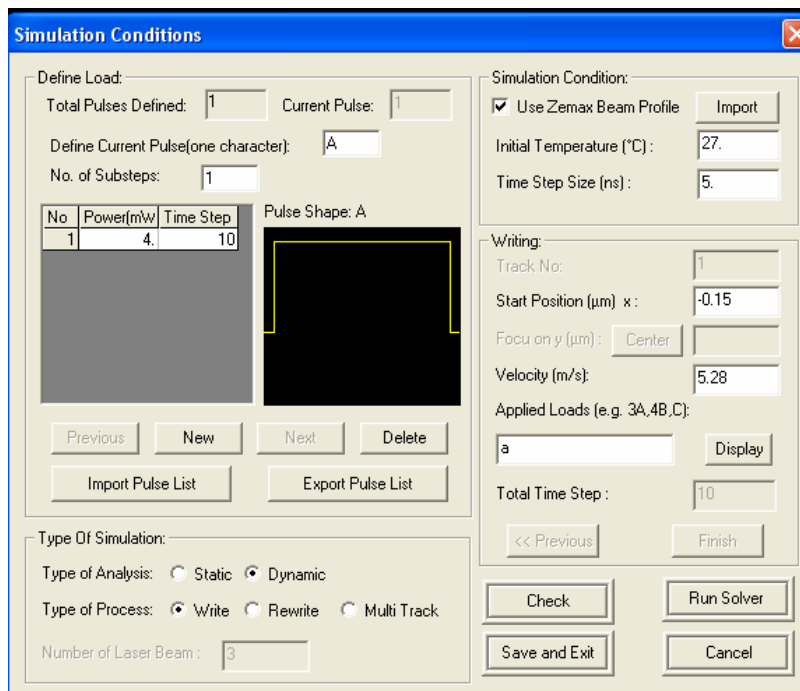


Figure 2.21 Dialog box for defining simulation conditions

2.3.2.3 Visualization of simulation results

The results of thermal analysis can be visualized in three dimensions. Figure 2.22 and Figure 2.23 demonstrate the three dimensions view of temperature profile and mark formation. The algorithms for three dimensional animation of mark formation have been implemented.

This feature will help user understand the physic behind mark formation better. Functions to display temperature along x , y or z direction, the time history of temperature and temperature changing rate of the disc are available. Figure 2.24 and Figure 2.25 present the plot of temperature along x , y or z direction and time history of

temperature of the disc, respectively. Also results of the analysis can be exported as in an ASCII data files. A section of source code for three dimensions view is shown in Appendix XI.

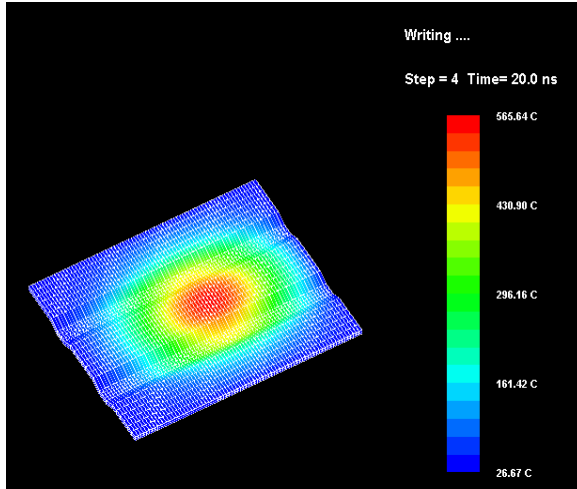


Figure 2.22 Temperature profile of the disc

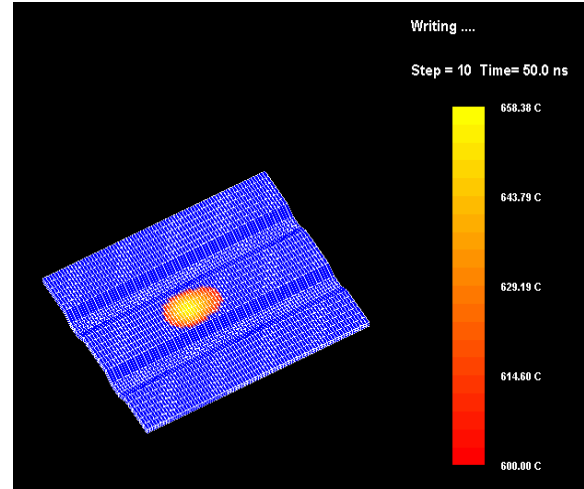


Figure 2.23 Mark formation on the disc

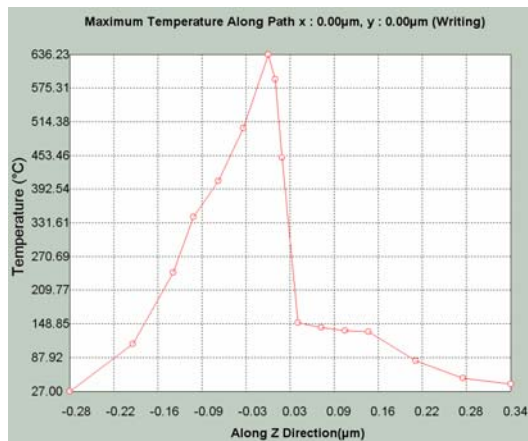


Figure 2.24 Temperature along x, y or z-direction of the disc

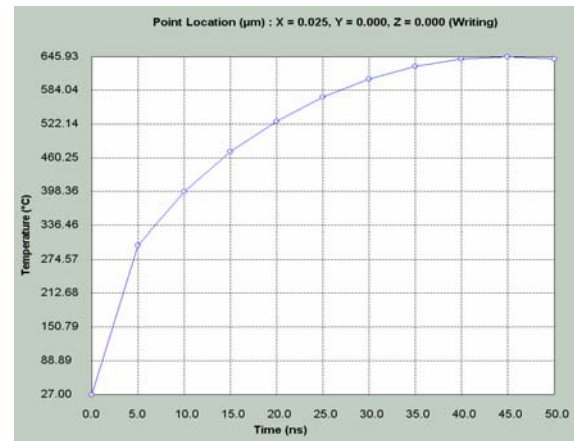


Figure 2.25 Time history of temperature of the disc

2.4 Summary

In this chapter, the objectives of developing of IOSMDS are further elaborated. The structure, function implementation and simulation process of the software are described. The interface and functions of the software are also introduced and illustrated.

Chapter 3 Optical system design

3.1 Working principle of the optical pick up head system

Figure 3.1 shows a schematic diagram of an optical pick-up head system. The collimator lens is used to collimate the laser beams from laser diode into a parallel beam. The laser beam passing through the collimator lens is transformed into a flat-top shape when passing through the beam shaper. The laser beam is then diverted to the objective lens. The objective lens is used to focus the laser beam onto the optical disc. The light reflected from the disc is transmitted through the polarizing beam splitter to the sensor lens. The sensor lens consists of both concave and cylindrical lenses. The sensor lens is used to create an astigmatic reflected laser beam which is use for focusing error signal detection. The detector is generally divided into four divisions namely A, B, C and D. Figure 3.2 shows the shapes of spots obtained from detector when the objective lens is placed near to the disc, focus on the disc and far from the disc respectively. By reading the signal from the A,B,C and D divisions, the focusing error signal can be obtained by the operation $(A+C) - (B+D)$. The $(A+C) - (B+D)$ signal is given the name of “S-curve”. When $(A+C) - (B+D) = 0$, the objective lens is on focus, on the other hand, if $(A+C) - (B+D) < 0$, the objective lens is close to the disc and if $(A+C) - (B+D) > 0$, the objective lens is away from the disc.

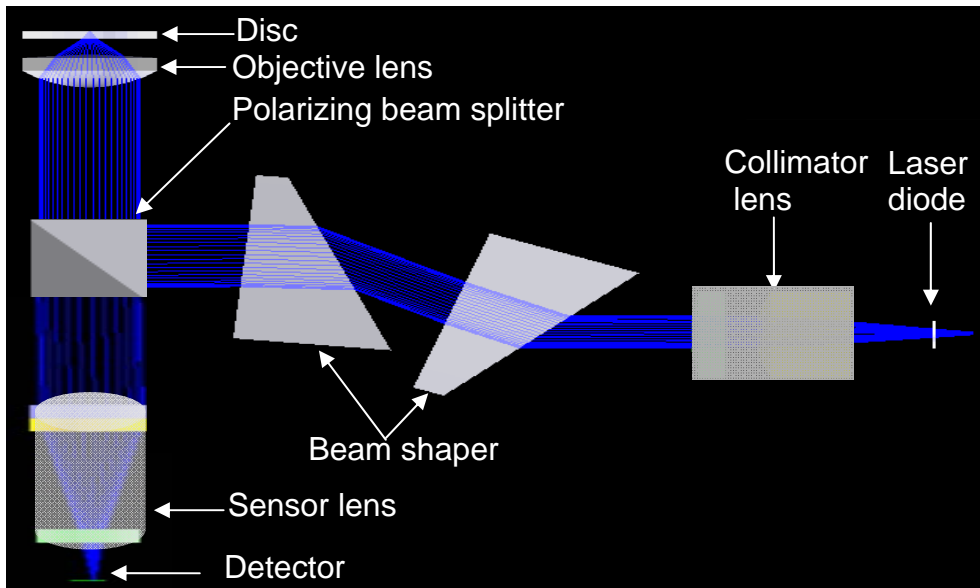


Figure 3.1 Schematic diagram of the optical pick-up head system

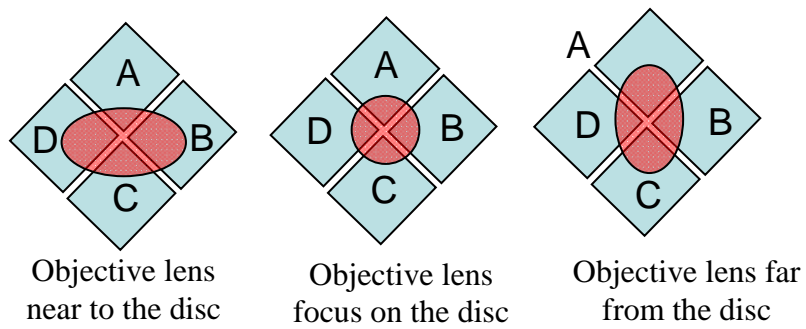


Figure 3.2 Light spots obtained from detector

3.2 System parameter comparison for optical discs

Comparison of the system parameters for CD, DVD and Blu-ray optical discs are shown in Table 3.1 [22].

Table 3.1 Optical disc and system parameters

Parameter	CD	DVD	Blu-Ray (BD)
Disc diameter	120mm	120mm	120mm
Read layer thickness	1.2mm	0.6mm	0.1mm
Number of recording layers	Single layer single side	Single layer single side to double layer double side (4 layers)	Single layer and double layer
Capacity of single layer	680MB	4.7GB	25GB
Track pitch	1.6um	0.74um	0.32um
Min pitch length	0.83um	0.4um	0.149um
Wavelength	780nm	650nm	405nm
N.A	0.45	0.6	0.85
RMS wave-front error	0.07λ	0.033λ	0.033λ
Video format	MPEG 1	MPEG 2	MPEG 2
Audio format	MPEG	MPEG 1 AC3 Dolby	MPEG 1 AC3 Dolby
Focusing method	Astigmatism	Astigmatism	Astigmatism
Movable focusing distance	+/-0.8mm	+/-0.6mm	+/-0.6mm
Tracking method	Three laser beam method	Differential phase detection	Differential phase detection
Movable tracking distance	+/-0.3mm	+/-0.3mm	+/-0.3mm

3.3 Optical system design parameter consideration

Large NA and shorter wavelength reduce the spot size of the light beam, contributing to higher density recording. The depth of focus will become shorter as NA increases according to the equation below:

$$\text{Depth of focus} = \lambda / (2 \times \text{NA}^2), \text{ where } \lambda \text{ is the wavelength} \quad (3.1)$$

The shorter depth of focus will increase the difficulty of servo control. The optimal value of NA has to be chosen based on the above consideration. The typical NA values of objective lens for several types of optical disc system are listed in Table 3.2.

Table 3.2 NA values of objective lens for different optical disc systems

Type	NA
CD-ROM	0.45
CD-RW	0.50
DVD-ROM	0.60
DVD-RW	0.65
HD-DVD	0.85

3.4 Optical pick up head design

An optical pick-up head design process consists of four stages [23]:

- 1) Objective lens-to-disc design
- 2) Optical path from laser diode-to-collimator lens design
- 3) Incident optical path design, from optical source-to-optical disc
- 4) Reflected optical path design, from beam splitter-to-detector

3.4.1 Objective lens-to-disc design

The objective lens is the main component for focusing and tracking servo control, therefore its accuracy is very critical. Moreover, since the objective lens is moved by a motor during the reading and writing processes, it has to be of small size and light weight for power saving and fast seeking purposes. The double aspheric surface glass or polycarbonate lens is used to reduce the lens size, weight and aberration.

The “sag” or z-coordinate of the aspheric surface [24] is given by

$$Z = \frac{cr^2}{1 + \sqrt{1 - (1+k)c^2r^2}} + \alpha_1 r^2 + \alpha_2 r^4 + \alpha_3 r^6 + \alpha_4 r^8 + \alpha_5 r^{10} + \alpha_6 r^{12} + \alpha_7 r^{14} + \alpha_8 r^{16}, \quad (3.2)$$

where c is the curvature (the reciprocal of the radius), r is the radial coordinate in lens unit, k is the conic constant and α_1 to α_8 are the parameter definitions for even aspheric surfaces. When $\alpha_1, \alpha_2, \alpha_3, \dots, \alpha_8 = 0$, the conic constant, k , assumes the following values: $k < -1$ for hyperbolas, $k = -1$ for parabolas, $-1 < k < 0$ for ellipses, $k=0$ for spheres and $k > 0$ for oblate ellipsoids.

3.4.1.1 DVD's objective lens-to-disc design

The NA is given by

$$NA = n \sin (\theta) = D / (2f), \quad (3.3)$$

where n is the refractive index, θ is the half-angle of the maximum cone of light picked up by objective lens, f is the effective focal length and D is the effective diameter of the objective lens, as shown in Figure 3.3.

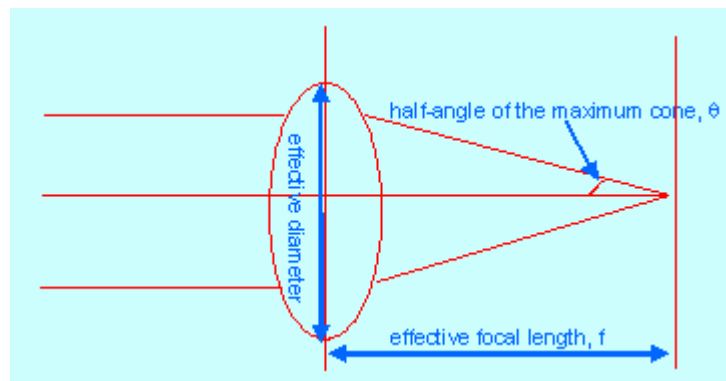


Figure 3.3 Definition of parameters for NA calculation

From Table 3.2, we know that the NA of DVD's objective lens is 0.6 is obtained by setting the effective focal length, f , to be 2.89mm, the effective diameter, D is found to be 3.468mm from equation 3.3. The design parameters and simulation results of the DVD's objective lens-to-disc design from an optical design software ZEMAX are shown in Figure 3.4 to Figure 3.6 and Table 3.3 to Table 3.5, respectively. The maximum value of the optical path difference is around 0.032λ after optimization.

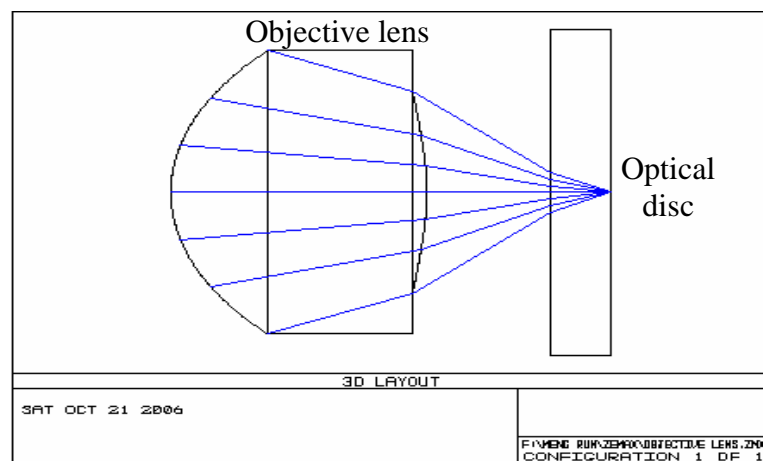


Figure 3.4 Three dimensional layout of DVD's objective lens-to-disc design

Table 3.3 Data of each defined surface for DVD's objective lens-to-disc design

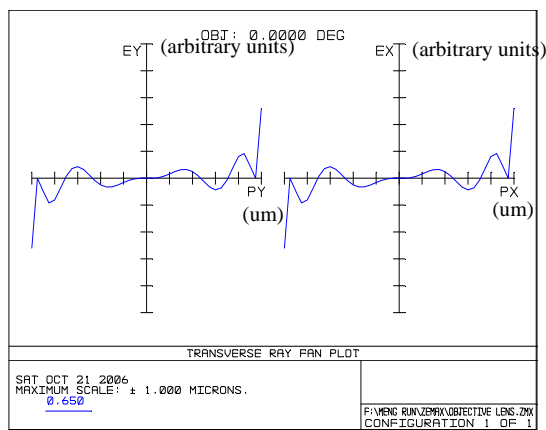
Surface type		Radius (mm)	Thickness(mm)	Glass type	Semi-diameter (mm)	Conic (mm)
OBJ	Standard	Infinity	Infinity		0.0	0.0
STO	Even Asphere	1.815	2.5	1.49,0.0	1.7366	-0.813278
2	Even Asphere	-3.52	1.2		1.238443	-30.184050
3	Standard	Infinity	0.6	1.56,0.0	2.0	0.0
IMA	Standard	Infinity		Pixels	0.000519	0.0

Table 3.4 Parameter definitions for even aspheric surfaces DVD's objective lens-to-disc design

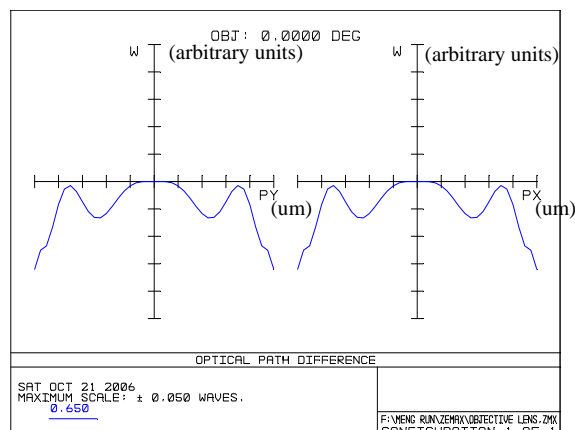
Surface	Stop (Even Asphere)	Surface 2 (Even Asphere)
Coefficient on r^2 (α_1)	0	0
Coefficient on r^4 (α_2)	0.008089	0
Coefficient on r^6 (α_3)	0	-0.000916
Coefficient on r^8 (α_4)	0	0.000347
Coefficient on r^{10} (α_5)	0	0
Coefficient on r^{12} (α_6)	0	0
Coefficient on r^{14} (α_7)	0	0
Coefficient on r^{16} (α_8)	0	0
Aperture	Floating aperture	Floating aperture
Maximum radius	1.7366	1.238443

Table 3.5 System data for DVD's objective lens-to-disc design

Surfaces	:	5
Stop	:	4
System Aperture	:	Entrance Pupil Diameter = 3
Glass Catalogs	:	Schott MISC
Ray Aiming	:	Off
Apodization	:	Uniform, factor = 0.00000E+000
Effective Focal Length	:	2.903286 (in air at system temperature and pressure)
Effective Focal Length	:	2.903286 (in image space)
Back Focal Length	:	-0.001084838
Total Track	:	14.3
Image Space F/#	:	0.9677619
Paraxial Working F/#	:	0.9677619
Working F/#	:	0.9786877
Image Space NA	:	0.4590126
Object Space NA	:	1.5e-010
Stop Radius	:	0.2076072
Paraxial Image Height	:	0
Paraxial Magnification	:	0
Entrance Pupil Diameter	:	3
Entrance Pupil Position	:	28.75743
Exit Pupil Diameter	:	0.4152143
Exit Pupil Position	:	-0.4029135
Field Type	:	Angle in degrees
Maximum Field	:	0
Primary Wave	:	0.65
Lens Units	:	Millimeters
Angular Magnification	:	0



(a) Ray aberration



(b) Optical path difference

Figure 3.5 Ray aberration and optical path difference of pupil's X and Y coordinates for DVD's objective lens-to-disc design

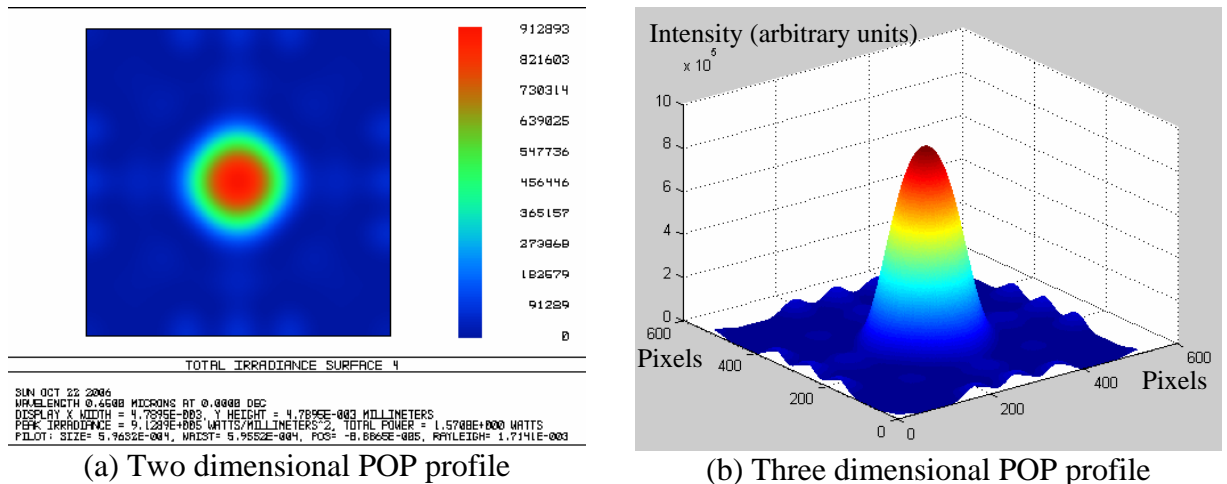


Figure 3.6 Two dimensional and three dimensional plot of physical optical propagation (POP) for DVD's objective lens-to-disc design

3.4.1.2 Blu-ray disc's objective lens-to-disc design

From Table 3.2, the NA of Blu-ray's objective lens is 0.85. By setting the effective focal length, f to be 1.9mm, the effective diameter, D , is found to be 3.23mm from Equation 3.3. The design parameters and simulation results of the Blu-Ray's objective lens by optical solver are shown in Figure 3.7 to Figure 3.9 and Table 3.6 to Table 3.8, respectively. The maximum value of the optical path difference is around 0.052λ after optimization.

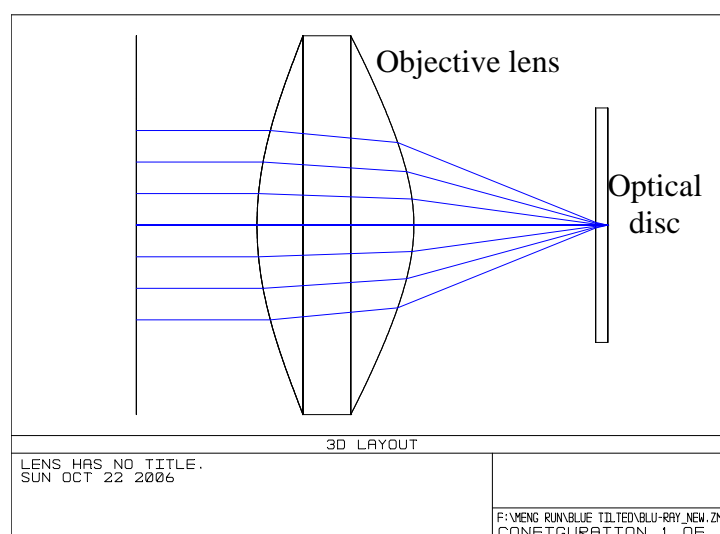


Figure 3.7 Three dimensional layout of Blu-ray disc's objective lens-to-disc design

Table 3.6 Data of each defined surface for Blu-ray disc's objective lens-to-disc design [22]

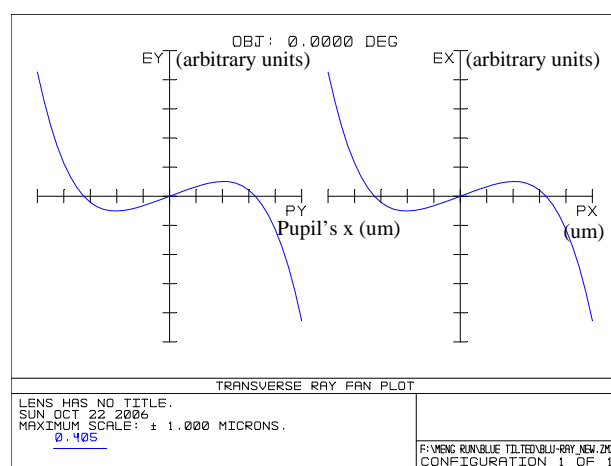
Surface type		Radius (mm)	Thickness (mm)	Glass type	Semi-diameter (mm)	Conic (mm)
OBJ	Standard	Infinity	Infinity		0.0	0.0
STO	Standard	Infinity	1.0		1.615	0.0
2	Even Asphere	2.828398	1.23	HMBACD-5N	1.615	-0.15773
3	Even Asphere	-1.602	1.5067		1.615	-5.1583
4	Standard	Infinity	0.1	1.57,90.0	1.0	0.0
IMA	Standard	Infinity		1.57,90.0	0.00002	0.0

Table 3.7 Parameter definitions for even aspheric surfaces Blu-ray disc's objective lens-to-disc design [22]

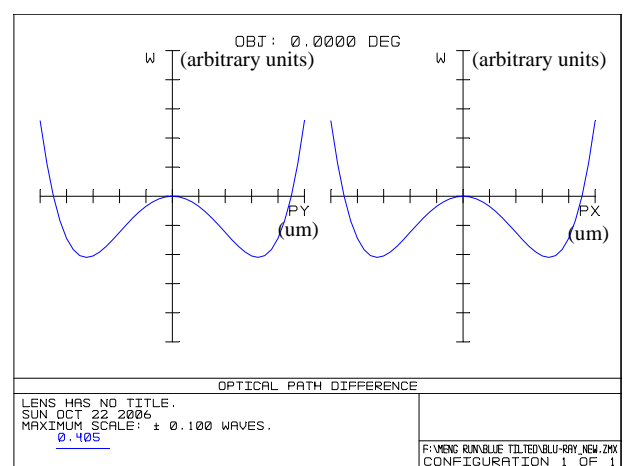
Surface	Surface 2 (Even Asphere)	Surface 3 (Even Asphere)
Coefficient on r^2 (α_1)	0	0
Coefficient on r^4 (α_2)	-0.1395	-0.0095
Coefficient on r^6 (α_3)	-0.004299	0.004021
Coefficient on r^8 (α_4)	0.002166	-0.00073
Coefficient on r^{10} (α_5)	-0.000385	-0.000013
Coefficient on r^{12} (α_6)	0	0
Coefficient on r^{14} (α_7)	0	0
Coefficient on r^{16} (α_8)	0	0
Aperture	Floating aperture	Floating aperture
Maximum radius	1.615	1.615

Table 3.8 System data for Blu-ray disc's objective lens-to-disc design

Surfaces	:	5
Stop	:	1
System Aperture	:	Entrance Pupil Diameter = 1.615
Glass Catalogs	:	Schott MISC
Ray Aiming	:	Off
Apodization	:	Uniform, factor = 0.00000E+000
Effective Focal Length	:	1.9 (in air at system temperature and pressure)
Effective Focal Length	:	3.001743 (in image space)
Back Focal Length	:	0.001264324
Total Track	:	3.906637
Image Space F/#	:	1.176471
Paraxial Working F/#	:	1.176471
Working F/#	:	1.305366
Image Space NA	:	0.4104094
Object Space NA	:	8.075E-011
Stop Radius	:	0.8075
Paraxial Image Height	:	0
Paraxial Magnification	:	0
Entrance Pupil Diameter	:	1.615
Entrance Pupil Position	:	0
Exit Pupil Diameter	:	9.63
Exit Pupil Position	:	-17.89772
Field Type	:	Angle in degrees
Maximum Field	:	0
Primary Wave	:	0.405
Lens Units	:	Millimeters
Angular Magnification	:	0



(a) Ray aberration



(b) Optical path difference

Figure 3.8 Ray aberrations and optical path difference of pupil's X and Y coordinates for Blu-ray's objective lens-to-disc design

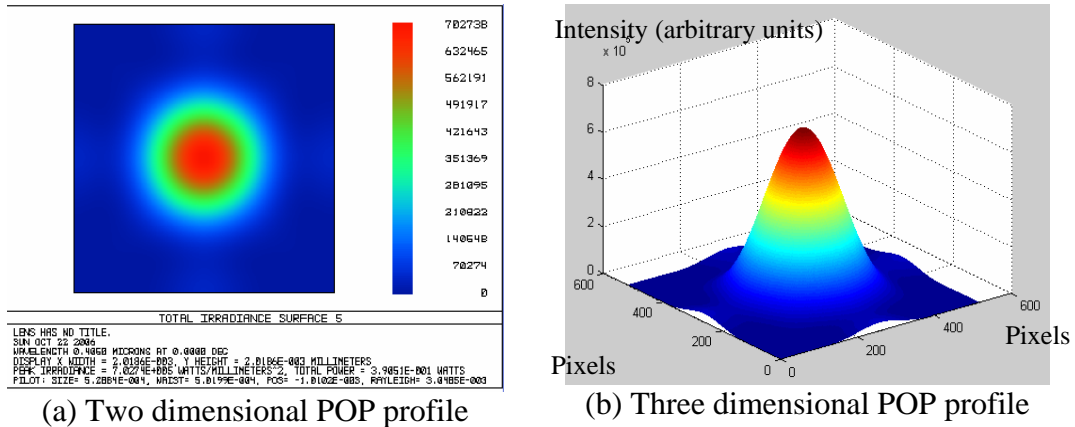


Figure 3.9 Two dimensional and three dimensional plots of physical optical propagation (POP) for Blu-ray's objective lens-to-disc design

3.4.2 Optical path design -- from laser diode-to-collimator lens

The purpose of the optical path design is to collimate the laser beams from laser diode into a parallel laser beam. The laser beam from the collimator lens is converted to a flat-top beam when it passes through the beam shaper. A flat-top beam is a laser beam with uniform intensity distribution over the cross section of working plane. The design parameters and simulation results of the DVD's optical path design (from optical source to collimator lens) are shown in Figure 3.10 and Table 3.9 to Table 3.11, respectively.

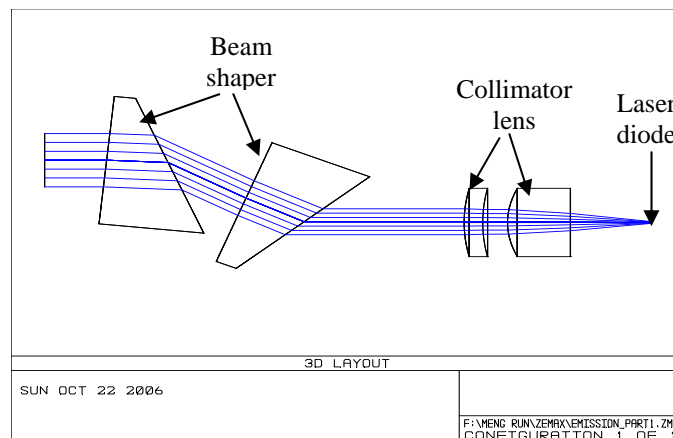


Figure 3.10 Three dimensional layout of for DVD's optical source-to-collimator lens design

Table 3.9 Data of each defined surface for DVD's optical source-to-collimator lens design

Surface type		Radius (mm)	Thickness (mm)	Glass type	Semi-diameter (mm)	Conic (mm)
OBJ	Standard	Infinity	Infinity	BK7	0.0	0.0
1	Standard	Infinity	5.0		2.5	0.0
2	Coord Break		0.0		0.0	
3	Tilted		5.1146	SF11	6.0	
4	Tilted		0.0		6.0	
5	Coord Break		6.0		0.0	
6	Coord Break		0.0		0.0	
7	Coord Break		0.0		0.0	
8	Tilted		5.1146	SF11	6.0	
9	Tilted		0.0		6.0	
STO	Coord Break		13.0		0.0	
11	Standard	12.48032	1.50	BK7	3.2	0.0
12	Standard	13.50582	2.0		3.2	0.0
13	Even Asphere	6.628	5.07	C05-50	3.2	-0.554366
14	Standard	Infinity	4.35637		3.2	0.0
15	Standard	Infinity	1.18		0.0	0.0
16	Standard	Infinity	0.25		0.0	0.0
17	Standard	Infinity	0.6		0.0	0.0
IMA	Standard	Infinity			0.0	0.0

Table 3.10 Parameter definitions for even aspheric surfaces DVD's optical source-to-collimator lens design

Surface	Surface 13 (Even Asphere)
Coefficient on r^2 (α_1)	0
Coefficient on r^4 (α_2)	0
Coefficient on r^6 (α_3)	-0.3186E-7
Coefficient on r^8 (α_4)	0
Coefficient on r^{10} (α_5)	0
Coefficient on r^{12} (α_6)	0
Coefficient on r^{14} (α_7)	0
Coefficient on r^{16} (α_8)	0
Aperture	Floating aperture
Maximum radius	3.2

Table 3.11 System data for DVD's optical source-to-collimator lens design

Surfaces	:	18
Stop	:	10
System Aperture	:	Entrance Pupil Diameter = 5
Glass Catalogs	:	Schott CORNING
Ray Aiming	:	Off
Apodization	:	Uniform, factor = 0.00000E+000
Effective Focal Length	:	11 (in air at system temperature and pressure)
Effective Focal Length	:	11 (in image space)
Back Focal Length	:	7.282369
Total Track	:	49.18557
Image Space F/#	:	2.2
Paraxial Working F/#	:	2.2
Working F/#	:	2.79103
Image Space NA	:	0.2216211
Object Space NA	:	3.786301E-10
Stop Radius	:	2.5
Paraxial Image Height	:	0
Paraxial Magnification	:	0
Entrance Pupil Diameter	:	5.0
Entrance Pupil Position	:	25.37963
Exit Pupil Diameter	:	11.83685
Exit Pupil Position	:	26.93707
Field Type	:	Angle in degrees
Maximum Field	:	0
Primary Wave	:	0.65
Lens Units	:	Millimeters
Angular Magnification	:	0

3.4.3 Incident optical path design-- from optical source to optical disc

Incident optical path is formed by placing the polarizing beam splitter between the optical lens and the beam shaper as shown in Figure 3.11.

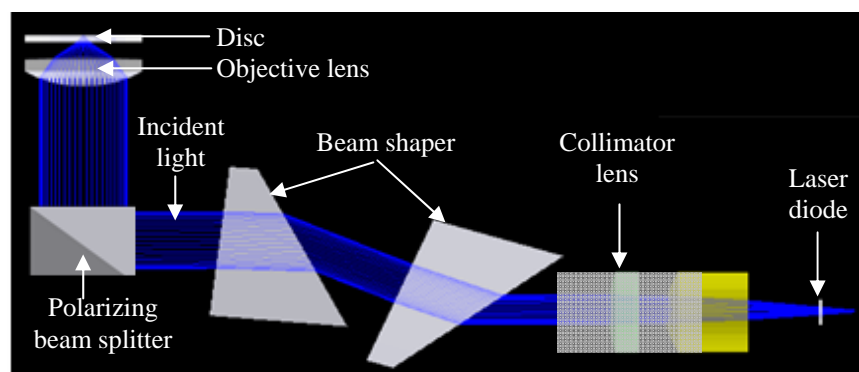


Figure 3.11 Schematic diagram of the incident optical path

3.4.4 Reflected optical path design -- from beam splitter to detector

In the reflected optical path design, the cylindrical lens is used to create an astigmatic reflected laser beam for error signal detection. The design parameters and simulation results of the DVD's Reflected optical path design from optical solver are shown in Table 3.12 and Figure 3.12, respectively.

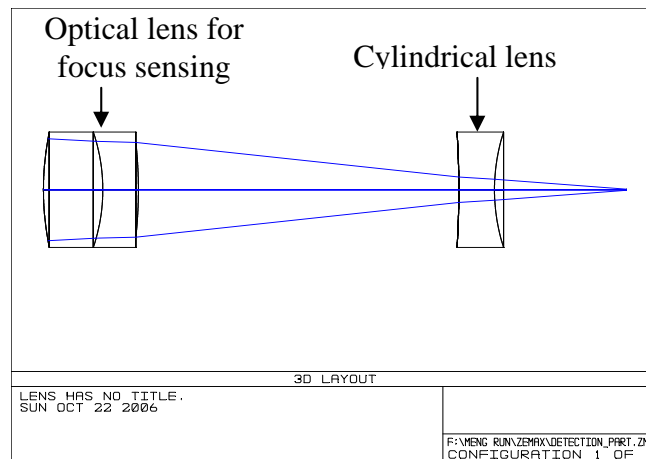


Figure 3.12 Three dimensional layout of for DVD's reflected optical path design

Table 3.12 Parameters of each defined surface for DVD's reflected optical path design

Surface type	Radius (mm)	Thickness (mm)	Glass type	Semi-diameter (mm)	Conic (mm)	
OBJ	Standard	Infinity	Infinity	0.0	0.0	
1	Standard	13.76	2.5	BK7	2.6	0.0
2	Standard	-8.65	1.5	DF5	2.6	0.0
3	Standard	-21.45	13.5		2.136950	0.0
4	Toroidal	-44.0	1.5	BK7	2.6	0.0
STO	Standard	9.0	5.56		2.6	0.0
IMA	Standard	Infinity			0.023329	0.0

3.4.5 Full optical path of optical pickup head design

By combining all the optical paths of Section 3.4.1 to Section 3.4.4, the schematic diagram of the full optical path is shown in Figure 3.1. Figure 3.13 illustrates the steps involved in the design of an system.

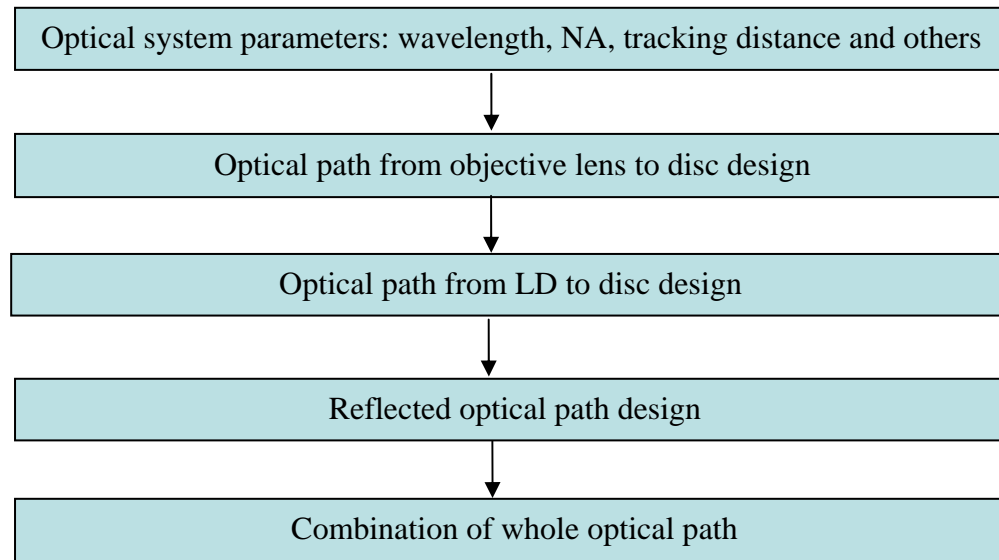


Figure 3.13 Flow chart of optical system design

3.5 Summary

In this chapter, The DVD pickup head with low OPD is designed. The Blu-ray pickup head with a low OPD is also designed. The beam profiles of both optical pickup heads are obtained.

Chapter 4 Fundamentals of optical and thermal analyses

4.1 Optical modeling: FDTD method

With the development of high storage density optical disc, the track pitch and the marks size are becoming comparable to the wavelength of the incident light which is used to write and read the disc. In this electromagnetic resonance region, the conventional first-order scalar approximation diffraction theory is no longer adequate [11][25]. In addition, the use of multilayer structure and high-numerical-aperture optical systems in current optical recording technology makes the situation even more complex. In order to fully understand the interaction of a focused beam with a multilayer disc, rigorous vector diffraction theories have been proposed. It is believed that finite methods are necessary for treating the aperiodic problem. Finite methods, such as boundary element method [26] and the finite-difference time-domain (FDTD) method [27-31], can be considered. But because of the complexity of the disc structures, the application of electromagnetic boundary conditions is difficult, making the first method less attractive because it requires numerous sub-domain divisions and a fine mesh. Therefore, the three-dimensional FDTD method for anisotropic media with non-diagonal tensors has been applied to analyze the near-field effect of optical storage in the present study, because of its small memory requirement, freedom from numerical issues of matrix inversion and the ease in treating complex materials and structures.

4.1.1 Generalized FDTD algorithm

The basis of the FDTD method is to solve the two time-domain Maxwell curl equations in the derivative form. The separate field formula of the Maxwell curl

equations are used [32] for the high-numerical-aperture incident focusing beam. In the nonmagnetic media of permeability μ_0 and permittivity $\bar{\epsilon}$, the two Maxwell curl equations can be written as

$$\frac{\partial \mathbf{H}^{scat}}{\partial t} = -\frac{1}{\mu_0} (\nabla \times \mathbf{E}^{scat}) \quad (4.1.1),$$

and

$$\bar{\epsilon} \frac{\partial \mathbf{E}^{scat}}{\partial t} = -\mathbf{J} - \left(\bar{\epsilon} - \epsilon_0 \right) \frac{\partial \mathbf{E}^{inc}}{\partial t} + \nabla \times \mathbf{H}^{scat} \quad (4.1.2),$$

where \mathbf{E}^{scat} and \mathbf{H}^{scat} are the scattered electric and magnetic fields, respectively, while \mathbf{E}^{inc} is the incident electric field, and \mathbf{J} is the polarization current. Note that the optical recording materials, also known as phase change materials, are nonmagnetic materials.

To implement the FDTD method, we discretize a space into a cubic mesh of Yee cells as shown in Figure 4.1. Material parameters are attributed to each cell of the mesh to create a discrete block representation of the optical disc structure. Maxwell's time-domain equations in derivative form are solved directly at the points within the cells with central finite differencing technique.

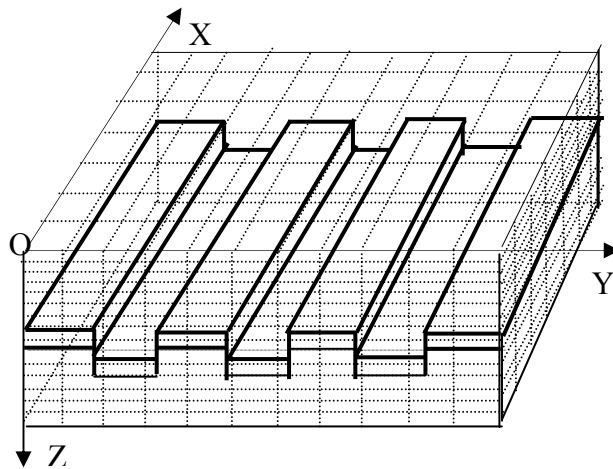


Figure 4.1 Disc Structure with FDTD grid

The generalized FDTD update equations for different scalar components will be presented in the following section while the update equations for magnetic field are the same as the original FDTD equations,

$$H_x^{scat,n+\frac{1}{2}} = H_x^{scat,n-\frac{1}{2}} + \frac{\Delta t}{\mu_0} \left[\frac{\Delta E_y^{scat,n}}{\Delta z} - \frac{\Delta E_z^{scat,n}}{\Delta y} \right] \quad (4.1.3-a),$$

$$H_y^{scat,n+\frac{1}{2}} = H_y^{scat,n-\frac{1}{2}} + \frac{\Delta t}{\mu_0} \left[\frac{\Delta E_z^{scat,n}}{\Delta x} - \frac{\Delta E_x^{scat,n}}{\Delta z} \right] \quad (4.1.3-b),$$

$$H_z^{scat,n+\frac{1}{2}} = H_z^{scat,n-\frac{1}{2}} + \frac{\Delta t}{\mu_0} \left[\frac{\Delta E_x^{scat,n}}{\Delta y} - \frac{\Delta E_y^{scat,n}}{\Delta x} \right] \quad (4.1.3-c),$$

For materials used in optical disc system, the permittivity $\bar{\varepsilon}$ can be expressed as

$$\bar{\varepsilon} = \begin{bmatrix} \varepsilon_1 & 0 & 0 \\ 0 & \varepsilon_2 & 0 \\ 0 & 0 & \varepsilon_3 \end{bmatrix} \quad (4.1.4),$$

The electric field update equations shown below can be obtained by substituting Equation (4.1.4) into Equation (4.1.2),

$$E_x^{scat,n} = E_x^{scat,n-1} - \frac{\varepsilon_2 \Delta t}{A} J_x^{n-\frac{1}{2}} - \varepsilon_2 (\varepsilon_1 - \varepsilon_0) \frac{\Delta t}{A} \frac{\partial E_x^{inc}}{\partial t} + \varepsilon_2 \frac{\Delta t}{A} \frac{\Delta H_z^{scat,n-\frac{1}{2}}}{\Delta y} - \varepsilon_2 \frac{\Delta t}{A} \frac{\Delta H_y^{scat,n-\frac{1}{2}}}{\Delta z} \quad (4.1.5-a),$$

$$E_y^{scat,n} = E_y^{scat,n-1} - \frac{\varepsilon_1 \Delta t}{A} J_y^{n-\frac{1}{2}} - \varepsilon_1 (\varepsilon_2 - \varepsilon_0) \frac{\Delta t}{A} \frac{\partial E_y^{inc}}{\partial t} + \varepsilon_1 \frac{\Delta t}{A} \frac{\Delta H_x^{scat,n-\frac{1}{2}}}{\Delta z} - \varepsilon_1 \frac{\Delta t}{A} \frac{\Delta H_z^{scat,n-\frac{1}{2}}}{\Delta x} \quad (4.1.5-b),$$

$$E_z^{scat,n} = E_z^{scat,n-1} - \frac{\Delta t}{\varepsilon_3} J_z^{n-\frac{1}{2}} - \frac{(\varepsilon_3 - \varepsilon_0) \Delta t}{\varepsilon_3} \frac{\partial E_z^{inc}}{\partial t} + \frac{\Delta t}{\varepsilon_3} \left[\frac{\Delta H_y^{scat,n-\frac{1}{2}}}{\Delta x} - \frac{\Delta H_x^{scat,n-\frac{1}{2}}}{\Delta y} \right] \quad (4.1.5-c),$$

For most lossy dielectric materials, a simple conductivity σ model is adequate to describe the polarization current [33], i.e,

$$\mathbf{J} = \overline{\overline{\sigma}}(\mathbf{E}^{scat} + \mathbf{E}^{inc}) \quad (4.1.6),$$

However, this conductivity model does not work well for metals and those phase change materials which have a larger extinction coefficient (k) compared with the refractive index (n) at the frequencies of visible light. This is because the values of field components calculated tend to infinity quickly and make the computation instable. Thus, these kinds of materials should be modeled using an appropriate phenomenological relationship between the electric field and the polarization. The Lorentz-linear dispersion model is chosen to model such materials [33]. With the Lorentz-linear dispersion model, the polarization current, \mathbf{J} , can be obtained by solving the following equations

$$\frac{\partial \mathbf{J}}{\partial t} = -\Gamma \mathbf{J} + \omega_0^2 [\varepsilon_0 \chi_0 (\mathbf{E}^{scat} + \mathbf{E}^{inc}) - \mathbf{P}] \quad (4.1.7),$$

and

$$\frac{\partial \mathbf{P}}{\partial t} = \mathbf{J} \quad (4.1.8),$$

where \mathbf{P} is the polarization, χ_0 is the low frequency to dc response of the polarization to the electric field, ω_0 is the resonant frequency and Γ is the damping coefficient. ω_0 and Γ can be obtained as shown below:

$$\omega_0 = \frac{w}{\left\{ 1 - \frac{\chi_0 (\varepsilon_r - \varepsilon_\infty / \varepsilon_0)}{(\varepsilon_r - \varepsilon_\infty / \varepsilon_0)^2 + \varepsilon_i^2} \right\}^2} \quad (4.1.9),$$

$$\Gamma = \frac{w \chi_0 \varepsilon_i}{(\varepsilon_r - \varepsilon_\infty / \varepsilon_0)^2 + \varepsilon_i^2 - \chi_0 (\varepsilon_r - \varepsilon_\infty / \varepsilon_0)}. \quad (4.1.10),$$

The complex permittivity ε is defined to be $\varepsilon_r - j\varepsilon_i = (n^2 - k^2) - j2nk$, where ε_0 is the permittivity of vacuum, ε_∞ is the permittivity of a medium versus an infinite frequency and w is the incident laser beam frequency.

It is found that it is advantageous to choose the polarization field \mathbf{P} and the polarization current \mathbf{J} to be volume quantities uniform over each cell, hence, they can be evaluated at the cell centers conveniently. At the same time, the polarization current \mathbf{J} must be evaluated at half-integer time steps along with the magnetic field \mathbf{H} , while the electric field \mathbf{E} and the polarization field \mathbf{P} are evaluated at integer time steps to achieve a proper interleaving of the discrete unknowns.

In the following, the discrete equations are given for two materials. The lossy dielectric materials can be described by the conductivity σ model,

$$\sigma = \begin{bmatrix} \sigma_1 & 0 & 0 \\ 0 & \sigma_2 & 0 \\ 0 & 0 & \sigma_3 \end{bmatrix} \quad (4.1.11),$$

and the update equations become

$$J_x^{n+\frac{1}{2}} = \sigma_1 (E_x^{scat,n} + E_x^{inc,n}) \quad (4.1.12-a),$$

$$J_y^{n+\frac{1}{2}} = \sigma_2 (E_y^{scat,n} + E_y^{inc,n}) \quad (4.1.12-b),$$

$$J_z^{n+\frac{1}{2}} = \sigma_3 (E_z^{scat,n} + E_z^{inc,n}) \quad (4.1.12-c),$$

For metals and phase change materials, they are modeled by the Lorentz-linear dispersion model and according to Equation (4.1.7), the update equations are

$$J_x^{n+\frac{1}{2}} = \frac{1}{1 + \Gamma\Delta t} J_x^{n-\frac{1}{2}} + \frac{1}{1 + \Gamma\Delta t} \left\{ \Delta t \omega_0^2 \left[\varepsilon_0 \chi_0 (E_x^{scat,n} + E_x^{inc,n}) - P_x^n \right] \right\} \quad (4.1.13-a),$$

$$J_y^{n+\frac{1}{2}} = \frac{1}{1 + \Gamma\Delta t} J_y^{n-\frac{1}{2}} + \frac{1}{1 + \Gamma\Delta t} \left\{ \Delta t \omega_0^2 \left[\varepsilon_0 \chi_0 (E_y^{scat,n} + E_y^{inc,n}) - P_y^n \right] \right\} \quad (4.1.13-b),$$

$$J_z^{n+\frac{1}{2}} = \frac{1}{1 + \Gamma\Delta t} J_z^{n-\frac{1}{2}} + \frac{1}{1 + \Gamma\Delta t} \left\{ \Delta t \omega_0^2 \left[\varepsilon_0 \chi_0 (E_z^{scat,n} + E_z^{inc,n}) - P_z^n \right] \right\} \quad (4.1.13-c),$$

Accordingly, the polarization fields for the metals can be updated by the following equations,

$$P_x^n = P_x^{n-1} + \Delta t J_x^{n-\frac{1}{2}} \quad (4.1.14-a),$$

$$P_y^n = P_y^{n-1} + \Delta t J_y^{n-\frac{1}{2}} \quad (4.1.14-b),$$

$$P_z^n = P_z^{n-1} + \Delta t J_z^{n-\frac{1}{2}} \quad (4.1.14-c),$$

The system will be in steady condition after enough rounds of iterations (about 5 to 6 optical cycles). The near field time-averaged fields are calculated by time-averaging all field components over the last optical cycle. The phases of them are found by checking at which the crossing from a positive value to zero. The light distribution on the far field detection pupil can then be obtained using the Fraunhofer diffraction method [25].

The far-field vector $E_{far}(x_0, y_0)$ of a pupil plane can be found by the Fourier transform,

$$E_{far}(x_0, y_0) = \iint_{pupil} E_{near}(x, y) \exp[-i2\pi(xx_0 + yy_0)] dx dy \quad (4.1.15),$$

The intensity of the far-field electric field is given by

$$I = E_{far}^2 = [|E_{far,x}(x_0, y_0)|^2 + |E_{far,y}(x_0, y_0)|^2 + |E_{far,z}(x_0, y_0)|^2] \quad (4.1.16),$$

4.1.2 Numerical solution

4.1.2.1 Updating the field components

In order to implement the update equations for various field components in C, we quantize space as $x=I \Delta x$, $y=J \Delta y$, $z=K \Delta z$, and time, $t=n \Delta t$. Then we define uniform Yee cells in space and indicate them as I, J and K . Within each Yee cell we choose to locate the field components at an offset that results in spatially centered differencing as shown in Figure 4.2.

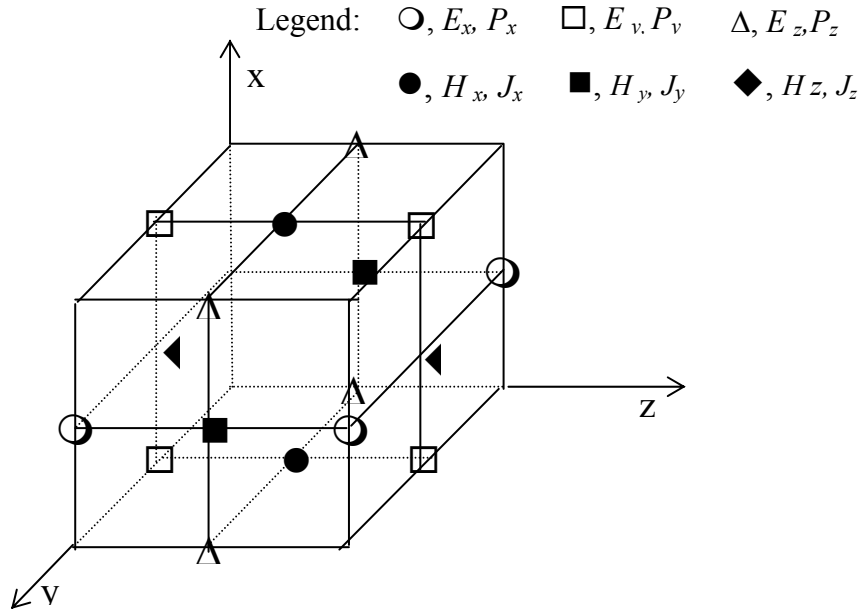


Figure 4.2. Unit Yee Cell in FDTD algorithm

The scattered electric field component $E_x^{scat,n}$ is written as subscripted array variable EXS[I][J][K] in the C source code, with the time step determined by an index (integer variable) N in the C code. It is the same for other electric field components and polarization components. Similarly, $H_x^{scat,n+\frac{1}{2}}$ can be written as HXS[I][J][K] and the spatial offset, different from the offset for EXS, is determined by H_x in the Yee cell. The temporal offset is also considered, so that the time index variable N in the C code corresponds to time step number $n=N$ for electrical fields and polarization and $n=N+1/2$ for magnetic field and the polarization current. This means that \mathbf{E} and \mathbf{P} at time corresponding to $n=N$ are updated from their prior values at time $n=N-1$ and \mathbf{J} , curl of \mathbf{H} at time $n=N-1/2$, where the time step is Δt . Next \mathbf{H} and \mathbf{J} are evaluated at $n=N+1/2$ from their earlier values at $n=N-1/2$ and \mathbf{P} and curl of \mathbf{E} at $n=N$. This interleaves \mathbf{E} , \mathbf{P} and \mathbf{H} , \mathbf{J} temporally and results in a centered difference or “leapfrog in time” approach. After each update of \mathbf{E} , \mathbf{P} and \mathbf{H} , \mathbf{J} , the index of N is increased by 1 and the process is repeated. The spatial indices in the update equations are

determined by the Yee cell geometry. The update equations are also center differenced, indicating that nearest-neighbor interactions are involved.

4.1.2.2 Building the disc structure in Yee cells

The fundamental constraint in Yee cells is that the cell size must be much smaller than the smallest wavelength to ensure accurate results. A constraint often used is “10 cells per wavelength”, meaning that the side of each cell should have a length of at least $1/10\lambda$. In our software, user can select uniform cells of difference sizes in different directions. For example, $\Delta x=(1/20)\lambda$, $\Delta y=(1/20)\lambda$, and in z direction, $\Delta z=(1/65)\lambda$.

4.1.2.3 Size of time step

After the cell size is determined, the maximum size of the time step can be obtained immediately from the Courant condition to ensure stability of the numerical solution. To understand the Courant condition, we consider a plane wave propagate through an FDTD grid. In any time step every point on this wave must not pass through more than one cell, because during one time step FDTD can propagate the wave only from one cell to its nearest neighbors. For a 3-D rectangular grid,

$$v\Delta t \leq 1 / \sqrt{\frac{1}{(\Delta x)^2} + \frac{1}{(\Delta y)^2} + \frac{1}{(\Delta z)^2}} \quad (4.1.17),$$

where v is the velocity of propagation. In order to ensure stability, we use the velocity of light, c , in free space instead.

4.1.2.4 Radiation boundary condition

The FDTD computational space is necessarily bounded due to the memory limitation. When the scattered light arrives at the boundary, it will be reflected back into the computational space if we do not take preventive measures. One useful measure is to apply the outer radiation boundary condition (ORBC) to absorb the scatted light when it arrives at the boundary of the FDTD space so that scattering into boundless far

space is at least approximately simulated. The Second order Mur absorbing boundary is adopted in our simulation.

4.1.2.5 Near field to far field transformation

After enough iterative cycles (about 5 to 6 optical cycles), the system will be in steady condition. The near field time-averaged electric field will assume values that are calculated by time-averaging all electrical field components over the last optical cycle. The phase of them are found by checking at what time step positive zero-crossing occurs in the last one optical cycle (see Figure 4.3).

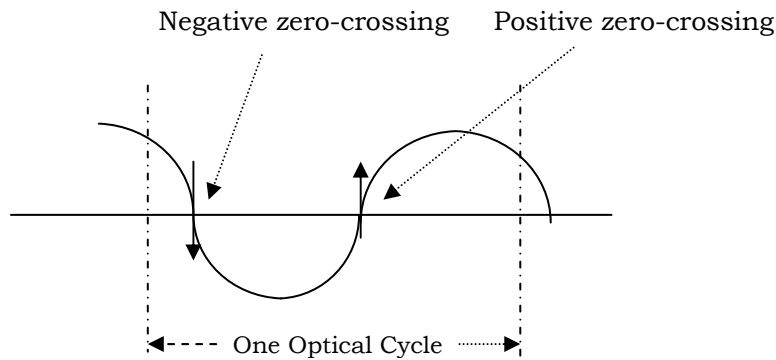


Figure 4.3 Scheme to find the phase of electric field

After obtaining the phase of the near field electric field, Fraunhofer diffraction is used to propagate the near field light into the far field detection pupil. The Fraunhofer diffraction can be numerically computed from the FFT algorithm. Suppose that the size of the range for FFT computation is N by N (see Figure 4.4), with N being the canonical coordinate, the unit scale is then given by

$$Scale = \frac{N}{N_s} \frac{\lambda}{NA} \quad (4.1.18),$$

where N_s is the number of sampling points (usually taking the values of 256, 512, 1024), λ is the incident wavelength and NA is the numerical aperture of the optical system. This results from the relationship between the real space unit scale and the canonical coordinate unit scale,

$$u_{real} = \frac{\lambda}{NA} u_c \quad (4.1.19),$$

where u_c is the canonical unit scale and u_{real} is that in real space.

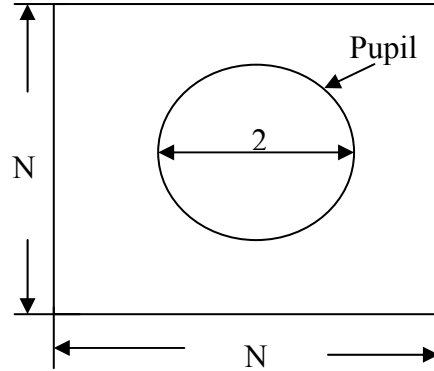


Figure 4.4 Diagram of the pupil in the FFT range

4.2 Thermal modeling: FEM method

The thermal model is expressed by the fundamental equations based on linear transient thermal conduction, as shown below [25]:

$$\rho c \frac{\partial T}{\partial t} - \frac{\partial}{\partial x} \left(k_x \frac{\partial T}{\partial x} \right) - \frac{\partial}{\partial y} \left(k_y \frac{\partial T}{\partial y} \right) - \frac{\partial}{\partial z} \left(k_z \frac{\partial T}{\partial z} \right) - Q = 0 \quad (4.2.1),$$

where ρ is the density, c is specific heat, T is temperature, k_x , k_y , k_z are thermal conductivities in three orthogonal dimensions and Q is the heat density due to the irradiation of the incident laser beam. Also, t is time variable, x , y and z are the space variables. For heat density calculation, all modeling and analysis of rewritable phase change optical disc are based on Gaussian distribution and exponential declining function along the direction of thickness. These models ignore the thermal effects caused by the laser light reflected by the reflective layer. Research done by *Shi et al* has shown that the thermal effects caused by the reflected laser light are significant. The differences have been found to be dependent on factors like the wavelength, power, spot size of the laser light and the thickness of the phase change layer. Therefore *Shi et al* have proposed the thermal model taking into consideration of both

the incident and reflected laser beams [34][35]. In this model, both the incident and reflected laser beams are taken into consideration for the heating source. Then the heat generated in the phase change layer $g(r, t)$ by laser irradiation can be decomposed into two parts written as follows:

$$I_1 = A_1 I_0 s(t) \beta \exp\left[-\frac{(x-vt)^2 + y^2}{r_0^2}\right] \exp[-\beta(z-z_2)] \quad (4.2.2),$$

$$I_2 = A_2 I_0 s(t) \beta \exp\left[-\frac{(x-vt)^2 + y^2}{r_0^2}\right] \exp[-\beta(z_3-z)] \exp[-\beta(z_3-z_2)] \quad (4.2.3),$$

$$g(r, t) = \frac{I_1 + I_2}{\pi r_0^2} \quad (4.2.4),$$

where I_1 and I_2 represent the contributions from the propagating and reflected light in the phase change layer, respectively; A_1 and A_2 are the attenuation factors, which can be calculated by optical method; β is the absorption coefficient given by $\beta=4\pi k/\lambda$; k is the optical extinction coefficient and λ is the wavelength of the laser. Also, while z is the distance into the phase change disc measured from the surface of the substrate layer, z_2 represents the distance to the interface of the phase change and first dielectric layer from the surface of the substrate; z_3 is then the distance from substrate to the interface of the phase change and second dielectric layer.

Li et al studied the multiples thin films of the optical disc using characteristic matrix method with the consideration of the absorption of laser beam by all layers in the disc, as well as multiple calorific and multi-track effects [25]. Considering the interface effect of the thin films, k_z (z refers to the thickness or z -direction of the thin films) is related to the bulk thermal conductivity, k , as shown below:

$$k_z = \alpha k \quad (4.2.5),$$

where α is a ratio within the range of [0, 1]. The ratio may be approximately estimated by the comparison of the readout waveforms of the marks from the experiment with the simulated marks.

Different recording technologies yield different amount of heat generation. The heat generated, Q , is determined by the light intensity distribution. For a Gaussian laser beam, the heat density distribution $Q(x, y, z, t)$ in the recording layer at a point (x, y, z) and time t with a focus point (x_0, y_0, z_0) on the incident interface of the phase-change layer is given by:

$$Q(x,y,z,t) = \frac{\gamma\beta I_0(t)}{\pi r^2} \exp\left[-\frac{(x-x_0-vt)^2 + (y-y_0)^2}{r^2}\right] \exp[-\beta(z-z_0)] \quad (4.2.6),$$

where I_0 is the incident light intensity at the center of the laser beam, given by

$$I_0 = \frac{P}{\pi r^2} \quad (4.2.7),$$

where P is the laser power. In Equation (4.2.6) and Equation (4.2.7), r is the laser beam radius, β is the absorption coefficient given by $\beta=4\pi k/\lambda$, k is the optical extinction coefficient, λ is the wavelength of the laser, γ is ratio of the energy of the incident light reaching the incident interface of the phase change layer.

The parameter γ may be determined by the optical characteristic matrix method as follows:

$$\begin{bmatrix} B \\ C \end{bmatrix} = \left(\prod_j^l \begin{bmatrix} \cos \delta_j & \frac{i}{\eta_j} \sin \delta_j \\ i\eta_j \sin \delta_j & \cos \delta_j \end{bmatrix} \right) \begin{bmatrix} 1 \\ \eta_{l+1} \end{bmatrix} \quad (4.2.8),$$

where B and C are parameters for determining the admittance of the thin film assembly. η_j and η_{l+1} are the complex refractive indices of the thin film media and outgoing medium, respectively, while δ_j is defined as follows:

$$\delta_j = \frac{2\pi}{\lambda}(n_j - ik_j)d_j \quad (4.2.9),$$

The energy reflectance R and transmittance T of the incident light can be characterized in terms of B and C as follows:

$$R = \left(\frac{\eta_0 B - C}{\eta_0 B + C} \right) \left(\frac{\eta_0 B - C}{\eta_0 B + C} \right)^* \quad (4.2.10),$$

$$T = \frac{4\eta_0\eta_{l+1}}{(\eta_0 B + C)(\eta_0 B + C)^*} \quad (4.2.11),$$

where * stands for a conjugated complex number. The energy absorbance A is therefore calculated from $A=1-R-T$. As an illustration, for the standard four-layer structure (dielectric/phase change layer/dielectric/reflective layer), the phase change layer mainly absorbs the energy of the incident laser beam. Thus it is reasonable to assume that the value of parameter γ is equal to A .

In the present study, the Gaussian beam profile as given in equation (4.2.6) will be replaced by the real beam profile obtained from ZEMAX using FEM modeling.

4.2.1 Initial and boundary conditions

4.2.1.1 Boundary condition at the disc surface

The heat source and heat generating area are on opposite sides of the disc. Both of which are also far away from the disc. To simplify the modeling, the effects caused by convection at the surface of the disc are neglected. Thus the temperature on the top and bottom surfaces of the optical disc is fixed at constant room temperature 27°C.

4.2.1.2 Initial condition

The initial temperature in the optical disc is specified to be the room temperature and the room temperature is assumed to be 27°C.

$$T_0 = T_{room} = 27^\circ\text{C}. \quad (4.2.12),$$

4.2.2 FEM solutions for 3D thermal conduction

4.2.2.1 Galerkin weighted residual method

In transient state, temperature at given points in the spatial domain varies with time.

The transient heat conduction equation is shown as below:

$$\rho c \frac{\partial T}{\partial t} = \frac{\partial}{\partial x} \left(k_x \frac{\partial T}{\partial x} \right) + \frac{\partial}{\partial y} \left(k_y \frac{\partial T}{\partial y} \right) + \frac{\partial}{\partial z} \left(k_z \frac{\partial T}{\partial z} \right) + Q \quad (4.2.13),$$

Residual R_Ω for the transient heat conduction equation in the domain Ω can be defined as:

$$R_\Omega = \frac{\partial}{\partial x} \left(k_x \frac{\partial T}{\partial x} \right) + \frac{\partial}{\partial y} \left(k_y \frac{\partial T}{\partial y} \right) + \frac{\partial}{\partial z} \left(k_z \frac{\partial T}{\partial z} \right) + \rho Q - \rho c \frac{\partial T}{\partial t} \quad (4.2.14),$$

where R_Ω is a function of position Ω and time t .

If the residual R_Ω is reduced to as close to zero as possible, as shown in Equation (4.2.15) below, the solution is exact.

$$\int_{\Omega} R_\Omega w_i d\Omega = 0 \quad (4.2.15),$$

The Galerkin weighted functions shown below are used in the numerical solution

$$w_i = N_i (i = 1, 2, \dots, 8) \quad (4.2.16),$$

Therefore we can obtain the following equation

$$\mathbf{CT} + \mathbf{KT} = \mathbf{P} \quad (4.2.17),$$

where \mathbf{C} is thermal capacity matrix and \mathbf{K} is thermal conduction matrix. Both of which are symmetrical positive definitely. Also \mathbf{P} is the temperature load vector and \mathbf{T} is the node temperature vector.

Note that

$$\begin{aligned} K_{ij} &= \sum_e K_{ij}^e + \sum_e H_{ij}^e \\ C_{ij} &= \sum_e C_{ij}^e \\ P_{ij} &= \sum_e P_{Q_e}^e + \sum_e P_{q_i}^e + \sum_e P_{H_i}^e \end{aligned} \quad (4.2.18),$$

where

$$\begin{aligned} C_{ij}^e &= \int_{\Omega^e} \rho c N_i N_j d\Omega \\ P_{Q_i}^e &= \int_{\Omega^e} \rho Q N_i d\Omega \end{aligned} \quad (4.2.19),$$

We then need to solve the one variable and one-degree differential equation,

$$\begin{aligned} C(T_{n+\alpha}, t_{n+\alpha}) \dot{T}_{n+\alpha} + K(T_{n+\alpha}, t_{n+\alpha}) T_{n+\alpha} &= P(T_{n+\alpha}, t_{n+\alpha}) \\ \text{Where} \quad C_{n+\alpha} &= C(T_{n+\alpha}, t_{n+\alpha}) \\ K_{n+\alpha} &= K(T_{n+\alpha}, t_{n+\alpha}) \\ P_{n+\alpha} &= P(T_{n+\alpha}, t_{n+\alpha}) \\ T_{n+\alpha} &= (1-\alpha)T_n + \alpha T_{n+1} \\ T_{n+\alpha} &= (T_{n+1} - T_n) / \Delta t = \Delta T / \Delta t \\ t_{n+\alpha} &= t_n + \alpha \Delta t \end{aligned} \quad (4.2.20),$$

Substituting these equations into the matrix equation, we obtain

$$\left[\frac{C_{n+\alpha}}{\Delta t} + \alpha K_{n+\alpha} \right] \Delta T = P_{n+\alpha} - K_{n+\alpha} T_n \quad (4.2.21),$$

If we define

$$\begin{aligned} K' &= \left[\frac{C_{n+\alpha}}{\Delta t} + \alpha K_{n+\alpha} \right] \\ P' &= P_{n+\alpha} - K_{n+\alpha} T_n \end{aligned} \quad (4.2.22),$$

then

$$\mathbf{K}' \cdot \Delta \mathbf{T} = \mathbf{P} \quad (4.2.23),$$

The method of Triangle decomposition method is used to solve the equations and ΔT is obtained. Then by using the equation

$$T_{n+1} = T_n + \Delta T \quad (4.2.24),$$

The temperature T_{n+1} at $t+\Delta t$ can be solved for.

4.2.2.2 Element chosen for thermal conduction problem

The temperature in an element can be expressed by a polynomial of coordinates. For 8-node element, the degree of the polynomial should be eight. The 3D 8-node isoparametric element as shown in Figure 4.5 is chosen to perform the thermal analysis. The shape functions for this element are listed as below

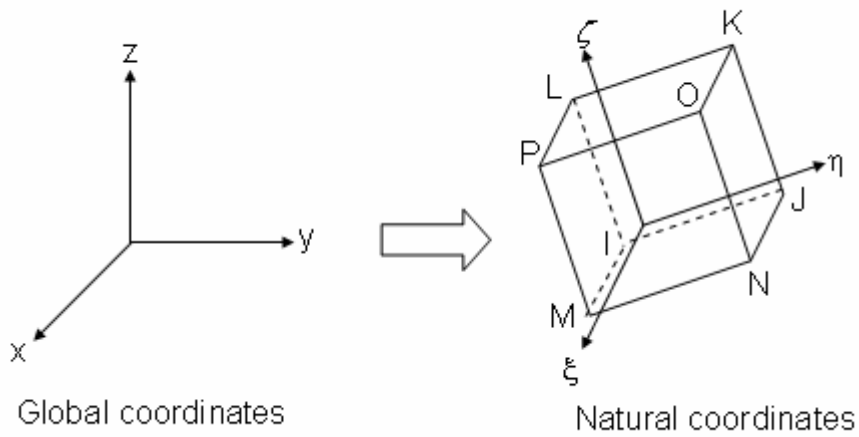


Figure 4.5 An 8-node 3D solid brick element for thermal analysis

The shape functions are defined

$$\begin{aligned} N_1 &= \frac{1}{8}(1-\xi)(1-\eta)(1-\zeta) & N_2 &= \frac{1}{8}(1+\xi)(1-\eta)(1-\zeta) \\ N_3 &= \frac{1}{8}(1+\xi)(1+\eta)(1-\zeta) & N_4 &= \frac{1}{8}(1-\xi)(1+\eta)(1-\zeta) \\ N_5 &= \frac{1}{8}(1-\xi)(1-\eta)(1+\zeta) & N_6 &= \frac{1}{8}(1+\xi)(1-\eta)(1+\zeta) \\ N_7 &= \frac{1}{8}(1+\xi)(1+\eta)(1+\zeta) & N_8 &= \frac{1}{8}(1-\xi)(1+\eta)(1+\zeta) \end{aligned} \quad (4.2.25),$$

where ξ, η, ζ are the natural coordinates.

The interpolation functions can write as follows:

$$x = \sum_{i=1}^8 N_i \cdot x_i \quad y = \sum_{i=1}^8 N_i \cdot y_i \quad z = \sum_{i=1}^8 N_i \cdot z_i \quad (4.2.26),$$

where x, y, z are global coordinates, then

$$\begin{Bmatrix} \frac{\partial N_i}{\partial \xi} \\ \frac{\partial N_i}{\partial \eta} \\ \frac{\partial N_i}{\partial \zeta} \end{Bmatrix} = \begin{bmatrix} \frac{\partial x}{\partial \xi} & \frac{\partial y}{\partial \xi} & \frac{\partial z}{\partial \xi} \\ \frac{\partial x}{\partial \eta} & \frac{\partial y}{\partial \eta} & \frac{\partial z}{\partial \eta} \\ \frac{\partial x}{\partial \zeta} & \frac{\partial y}{\partial \zeta} & \frac{\partial z}{\partial \zeta} \end{bmatrix} \cdot \begin{Bmatrix} \frac{\partial N_i}{\partial x} \\ \frac{\partial N_i}{\partial y} \\ \frac{\partial N_i}{\partial z} \end{Bmatrix} = \mathbf{J} \cdot \begin{Bmatrix} \frac{\partial N_i}{\partial x} \\ \frac{\partial N_i}{\partial y} \\ \frac{\partial N_i}{\partial z} \end{Bmatrix} \quad (4.2.27),$$

and Jacobian matrix \mathbf{J} can be calculated by the derivative of shape function in natural coordinates multiplied with node coordinates in global coordinates as follows:

$$\begin{aligned} \mathbf{J} &\equiv \begin{bmatrix} \frac{\partial x}{\partial \xi} & \frac{\partial y}{\partial \xi} & \frac{\partial z}{\partial \xi} \\ \frac{\partial x}{\partial \eta} & \frac{\partial y}{\partial \eta} & \frac{\partial z}{\partial \eta} \\ \frac{\partial x}{\partial \zeta} & \frac{\partial y}{\partial \zeta} & \frac{\partial z}{\partial \zeta} \end{bmatrix} = \begin{bmatrix} \sum_{i=1}^8 \frac{\partial N_i}{\partial \xi} x_i & \sum_{i=1}^8 \frac{\partial N_i}{\partial \xi} y_i & \sum_{i=1}^8 \frac{\partial N_i}{\partial \xi} z_i \\ \sum_{i=1}^8 \frac{\partial N_i}{\partial \eta} x_i & \sum_{i=1}^8 \frac{\partial N_i}{\partial \eta} y_i & \sum_{i=1}^8 \frac{\partial N_i}{\partial \eta} z_i \\ \sum_{i=1}^8 \frac{\partial N_i}{\partial \zeta} x_i & \sum_{i=1}^8 \frac{\partial N_i}{\partial \zeta} y_i & \sum_{i=1}^8 \frac{\partial N_i}{\partial \zeta} z_i \end{bmatrix} \\ &= \begin{bmatrix} \frac{\partial N_1}{\partial \xi} & \frac{\partial N_2}{\partial \xi} & \Lambda & \frac{\partial N_8}{\partial \xi} \\ \frac{\partial N_1}{\partial \eta} & \frac{\partial N_2}{\partial \eta} & \Lambda & \frac{\partial N_8}{\partial \eta} \\ \frac{\partial N_1}{\partial \zeta} & \frac{\partial N_2}{\partial \zeta} & \Lambda & \frac{\partial N_8}{\partial \zeta} \end{bmatrix} \cdot \begin{bmatrix} x_1 & y_1 & z_1 \\ x_2 & y_2 & z_2 \\ \mathbf{M} & \mathbf{M} & \mathbf{M} \\ x_8 & y_8 & z_8 \end{bmatrix} \end{aligned} \quad (4.2.28),$$

Finally the derivative of shape functions in global coordinates can be express as

$$\begin{Bmatrix} \frac{\partial N_i}{\partial x} \\ \frac{\partial N_i}{\partial y} \\ \frac{\partial N_i}{\partial z} \end{Bmatrix} = \mathbf{J}^{-1} \cdot \begin{Bmatrix} \frac{\partial N_i}{\partial \xi} \\ \frac{\partial N_i}{\partial \eta} \\ \frac{\partial N_i}{\partial \zeta} \end{Bmatrix} \quad (4.2.29),$$

For integration, the relationship between the global coordinate system and the natural coordinate system can be described as

$$dV = \begin{vmatrix} \frac{\partial x}{\partial \xi} & \frac{\partial y}{\partial \xi} & \frac{\partial z}{\partial \xi} \\ \frac{\partial x}{\partial \eta} & \frac{\partial y}{\partial \eta} & \frac{\partial z}{\partial \eta} \\ \frac{\partial x}{\partial \zeta} & \frac{\partial y}{\partial \zeta} & \frac{\partial z}{\partial \zeta} \end{vmatrix} \cdot d\xi d\eta d\zeta = |\mathbf{J}| \cdot d\xi d\eta d\zeta \quad (4.2.30),$$

The temperature can then be written in the following form:

$$T = \sum_{i=1}^8 N_i(x, y, z) \cdot T_i \quad (4.2.31),$$

4.2.2.3 Element stiffness matrix

The element stiffness matrix is given by

$$[\mathbf{K}]^e = \iiint_V [\mathbf{B}]^T [\mathbf{D}] [\mathbf{B}] dV \quad (4.2.32),$$

As the $[\mathbf{D}]$ matrix is only dependent on material properties and independent on the coordinates, the $[\mathbf{B}]$ matrix should be solved first to obtain the $[\mathbf{K}]$ matrix. The $[\mathbf{B}]$ matrix is given by

$$[\mathbf{B}] = \begin{bmatrix} \frac{\partial N_1}{\partial x} & & \frac{\partial N_2}{\partial x} & & \Lambda & \frac{\partial N_8}{\partial x} & & \\ & \frac{\partial N_1}{\partial y} & & \frac{\partial N_2}{\partial y} & \Lambda & & \frac{\partial N_8}{\partial y} & \\ & & \frac{\partial N_1}{\partial z} & & \frac{\partial N_2}{\partial z} & \Lambda & & \frac{\partial N_8}{\partial z} \\ \frac{\partial N_1}{\partial y} & \frac{\partial N_1}{\partial x} & & \frac{\partial N_2}{\partial y} & \frac{\partial N_2}{\partial x} & \Lambda & \frac{\partial N_8}{\partial y} & \frac{\partial N_8}{\partial x} \\ \frac{\partial N_1}{\partial z} & & \frac{\partial N_1}{\partial x} & \frac{\partial N_2}{\partial z} & & \frac{\partial N_2}{\partial x} & \Lambda & \frac{\partial N_8}{\partial z} & \frac{\partial N_8}{\partial x} \\ & \frac{\partial N_1}{\partial z} & \frac{\partial N_1}{\partial y} & & \frac{\partial N_2}{\partial z} & \frac{\partial N_2}{\partial y} & \Lambda & & \frac{\partial N_8}{\partial z} & \frac{\partial N_8}{\partial y} \end{bmatrix}_{6 \times 24} \quad (4.2.33),$$

The derivative of the shape functions in global coordinates can be found by multiplying the inverse of Jacobian matrix with the derivative of the shape function in natural coordinates as shown in Equation (4.2.34). Then $[\mathbf{B}]$ can be solved.

$$\begin{bmatrix} \frac{\partial N_1}{\partial x} & \frac{\partial N_2}{\partial x} & \frac{\partial N_3}{\partial x} & \frac{\partial N_4}{\partial x} & \frac{\partial N_5}{\partial x} & \frac{\partial N_6}{\partial x} & \frac{\partial N_7}{\partial x} & \frac{\partial N_8}{\partial x} \\ \frac{\partial N_1}{\partial y} & \frac{\partial N_2}{\partial y} & \frac{\partial N_3}{\partial y} & \frac{\partial N_4}{\partial y} & \frac{\partial N_5}{\partial y} & \frac{\partial N_6}{\partial y} & \frac{\partial N_7}{\partial y} & \frac{\partial N_8}{\partial y} \\ \frac{\partial N_1}{\partial z} & \frac{\partial N_2}{\partial z} & \frac{\partial N_3}{\partial z} & \frac{\partial N_4}{\partial z} & \frac{\partial N_5}{\partial z} & \frac{\partial N_6}{\partial z} & \frac{\partial N_7}{\partial z} & \frac{\partial N_8}{\partial z} \end{bmatrix} = \mathbf{J}^{-1} \cdot \begin{bmatrix} \frac{\partial N_1}{\partial \xi} & \frac{\partial N_2}{\partial \xi} & \frac{\partial N_3}{\partial \xi} & \frac{\partial N_4}{\partial \xi} & \frac{\partial N_5}{\partial \xi} & \frac{\partial N_6}{\partial \xi} & \frac{\partial N_7}{\partial \xi} & \frac{\partial N_8}{\partial \xi} \\ \frac{\partial N_1}{\partial \eta} & \frac{\partial N_2}{\partial \eta} & \frac{\partial N_3}{\partial \eta} & \frac{\partial N_4}{\partial \eta} & \frac{\partial N_5}{\partial \eta} & \frac{\partial N_6}{\partial \eta} & \frac{\partial N_7}{\partial \eta} & \frac{\partial N_8}{\partial \eta} \\ \frac{\partial N_1}{\partial \zeta} & \frac{\partial N_2}{\partial \zeta} & \frac{\partial N_3}{\partial \zeta} & \frac{\partial N_4}{\partial \zeta} & \frac{\partial N_5}{\partial \zeta} & \frac{\partial N_6}{\partial \zeta} & \frac{\partial N_7}{\partial \zeta} & \frac{\partial N_8}{\partial \zeta} \end{bmatrix} \quad (4.2.34),$$

And subsequently the element stiffness matrix, $[\mathbf{K}]$, can be calculated

$$[\mathbf{K}]^e = \iiint_V [\mathbf{B}]^T [\mathbf{D}][\mathbf{B}] dV = \iiint_V [\mathbf{B}]^T [\mathbf{D}][\mathbf{B}] \cdot |\mathbf{J}| \cdot d\xi d\eta d\zeta \quad (4.2.35),$$

Gauss Integration method is applied to transform the integration into numerical computation. The following function is assumed

$$G(\xi, \eta, \zeta) = [\mathbf{B}]^T \cdot [\mathbf{D}] \cdot [\mathbf{B}] \cdot |\mathbf{J}| \quad (4.2.36),$$

The 3 Gauss points integration technique is then used to calculate $[\mathbf{K}]^e$, as illustrated below.

The Gauss points ξ_i, η_j, ζ_m are given by

$$-0.7745966692415, 0, 0.7745966692415$$

While the corresponding weight function value H_i, H_j, H_m are given by

$$5/9, 8/9, 5/9$$

Then element stiffness matrix $[\mathbf{K}]^e$ can then be obtained as

$$\begin{aligned} [\mathbf{K}]^e &= \iiint_V [\mathbf{B}]^T [\mathbf{D}][\mathbf{B}] dV = \iiint_V [\mathbf{B}]^T [\mathbf{D}][\mathbf{B}] \cdot |\mathbf{J}| \cdot d\xi d\eta d\zeta \\ &= \sum_{m=1}^8 \sum_{j=1}^8 \sum_{i=1}^8 H_i H_j H_m \cdot G(\xi_i, \eta_j, \zeta_m) \end{aligned} \quad (4.2.37),$$

4.2.2.4 Global stiffness matrix

All the element stiffness matrices are assembled to form the global stiffness matrix, $[\mathbf{K}]$ as shown below

$$[\mathbf{K}] = \sum_N^e [\mathbf{G}]^T \cdot [\mathbf{K}]^e \cdot [\mathbf{G}] \quad (4.2.38),$$

where N is number of elements. $[\mathbf{G}]$ is the assemble matrix, given by the expression shown below

$$[\mathbf{G}]^T = \begin{matrix} 1 \\ M \\ i \\ M \\ j \\ M \\ k \\ M \\ l \\ M \\ m \\ M \\ n \\ M \\ o \\ M \\ p \\ M \\ N \end{matrix} \begin{bmatrix} 0 & 0 & 0 & 0 & 0 & 0 & 0 & 0 \\ 0 & 0 & 0 & 0 & 0 & 0 & 0 & 0 \\ I & 0 & 0 & 0 & 0 & 0 & 0 & 0 \\ 0 & 0 & 0 & 0 & 0 & 0 & 0 & 0 \\ 0 & I & 0 & 0 & 0 & 0 & 0 & 0 \\ M & M & 0 & 0 & & & & \\ & 0 & I & 0 & & & & \\ & & 0 & 0 & & & & \\ & & 0 & I & 0 & & & \\ & & & 0 & 0 & & & \\ & & & 0 & I & 0 & & \\ & & & & 0 & 0 & & \\ & & & & 0 & I & 0 & \\ & & & & & 0 & 0 & \\ & & & & & 0 & I & \\ & & & & & & & 0 \end{bmatrix} \quad (4.2.39),$$

4.2.3 Solving the linear equations

Generally speaking, there are two methods for solving linear equations, namely direct and iterative methods [36]. Direct methods include Gauss elimination method, Gauss and Jordan elimination method, Triangle decomposition method, Chase method, Divide into block method and Wavefront method. Iterative methods include Jacobi

iterative method, Gauss-Sidel iterative method and Over relaxation method. Direct methods are more efficient while iterative methods are more precise when the equations are huge.

In this research, the method of Triangular factorization [37] is used to solve the linear equations, as the coefficient matrices are symmetric. The algorithm is described below. It is given

$$\mathbf{K} \cdot \boldsymbol{\delta} = \mathbf{P} \quad (4.2.40),$$

where \mathbf{K} is the global stiffness matrix, $\boldsymbol{\delta}$ is the vector to be solved and \mathbf{P} is the global load vector.

Based on matrix decomposition theory,

$$\mathbf{K} = \mathbf{L} \cdot \mathbf{S}, \quad (4.2.41),$$

where \mathbf{S} is up-triangle matrix and \mathbf{L} is sub-triangle matrix defined as follows

$$L = \begin{bmatrix} 1 & & & & \\ l_{21} & 1 & & & \\ M & O & O & & \\ l_{n1} & l_{n2} & L & & 1 \end{bmatrix} \quad S = \begin{bmatrix} S_{11} & S_{12} & L & S_{1n} \\ & S_{22} & O & S_{2n} \\ & & O & M \\ & & & S_{nn} \end{bmatrix}. \quad (4.2.42),$$

Then decomposition of \mathbf{K} by \mathbf{L} and \mathbf{S} is done, leading to

$$L \cdot S \cdot \boldsymbol{\delta} = P \quad (4.2.43),$$

and then multiply the inverse of \mathbf{L} on both side, we obtain

$$S \cdot \boldsymbol{\delta} = L^{-1} \cdot P. \quad (4.2.44),$$

Setting $L^{-1} \cdot P = V$, we arrive at

$$S \cdot \boldsymbol{\delta} = V. \quad (4.2.45),$$

Therefore the two steps described below can be used to solve Equation (4.2.44)

(1) Solving for V

As $L \cdot V = P$ and L is sub-triangle matrix, V can be obtained after solving the following equations.

$$\text{Substituting forwards} \quad \begin{matrix} \triangle \\ \text{L} \end{matrix} \quad \begin{matrix} \square \\ \text{V} \end{matrix} = \begin{matrix} \square \\ \text{P} \end{matrix} \quad (4.2.46),$$

(2) Solving for δ

As $S \cdot \delta = V$ and S is the up-triangle matrix, so δ can be obtained after solving the following equations.

$$\text{Substituting backwards} \quad \begin{matrix} \triangle \\ \text{S} \end{matrix} \quad \begin{matrix} \square \\ \delta \end{matrix} = \begin{matrix} \square \\ \text{V} \end{matrix} \quad (4.2.47),$$

Next, by setting $D \cdot L^T = S$, $K = L \cdot D \cdot L^T$. Therefore

$$K_{ij} = \sum_{r=1}^i l_{ri}^T d_{rr} l_{rj}^T = \sum_{r=1}^{i-1} l_{ri}^T d_{rr} l_{rj}^T + l_{ii}^T d_{ii} l_{ij}^T, \quad (4.2.48),$$

Noted that

$$l_{ii}^T = 1, \quad D = \begin{bmatrix} d_{11} & 0 & L & 0 \\ 0 & d_{22} & O & M \\ M & O & O & 0 \\ 0 & L & 0 & d_{NN} \end{bmatrix}, \quad (4.2.49),$$

Then

$$d_{ii}l_{rj}^T = S_{ij} = K_{ij} - \sum_{r=1}^{i-1} l_{ri}^T d_{rr}l_{rj}^T$$

$$l_{ij} = S_{ij} / d_{ii}$$

$$d_{ii} = S_{ii}$$
(4.2.50),

The following procedure is carried out in the implementation of the algorithm

$$i = 1$$

$$S_{1j} = K_{1j} (j \geq 1)$$

$$d_{11} = S_{11} = K_{11}$$

$$l_{1j}^T = S_{1j} / d_{11} (j > 1)$$

... ..,

(4.2.51),

$$i = i$$

$$S_{ij} = K_{ij} (j \geq i)$$

$$d_{ii} = S_{ii}$$

$$l_{ij}^T = S_{ij} / d_{ii} (j > i)$$

4.2.4 Flow chart of finite element solution for thermal analysis

Figure 4.6 shows the steps involved in the finite element method for thermal analysis of optical discs. The thermal analysis simulator is designed according to the flow chart shows in Figure 4.6.

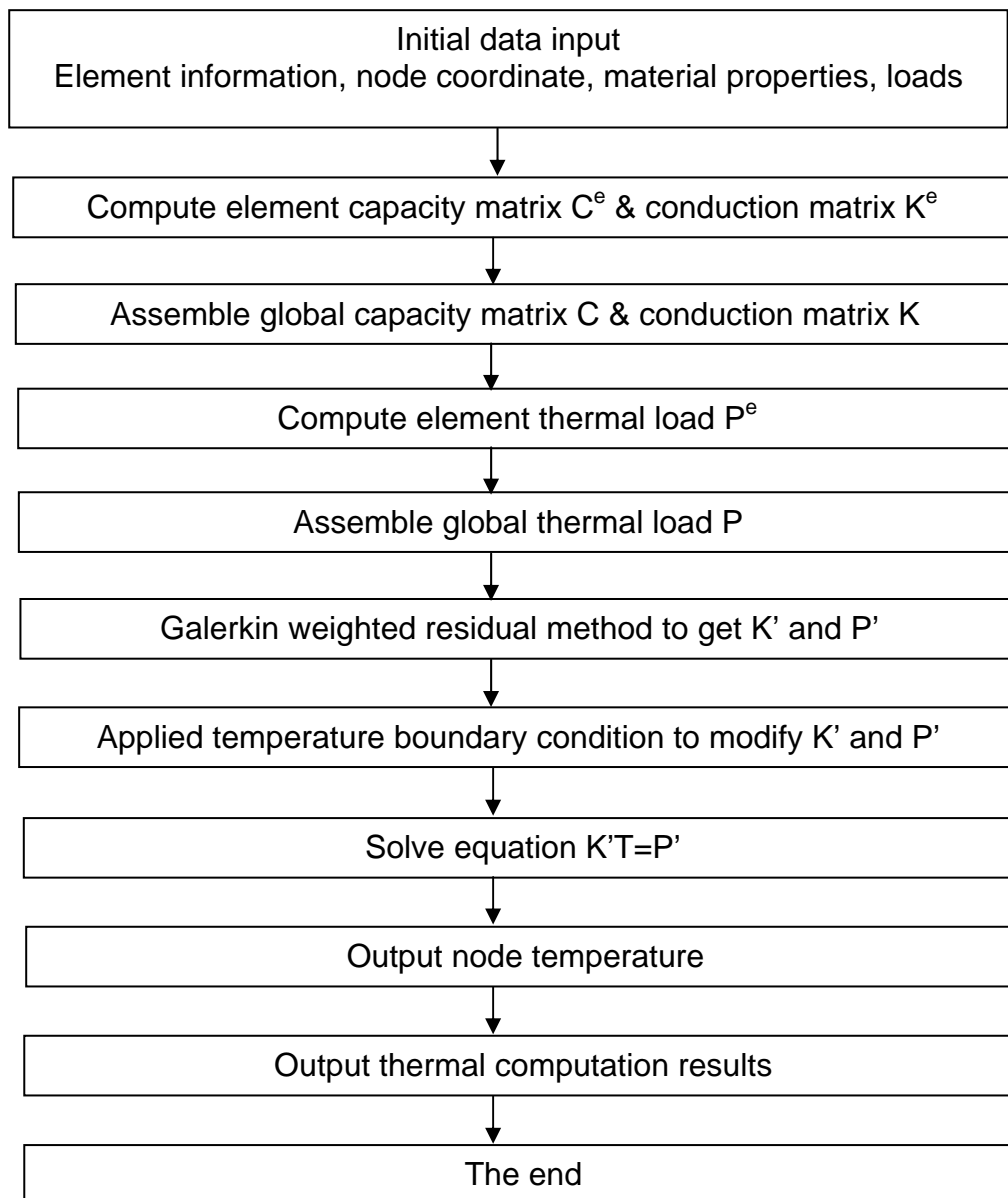


Figure 4.6 Flow chart of thermal analysis using finite element method

4.3 Crystallization modeling: JMA model

In the mark formation simulation, the Johnson-Mehl-Avrami (JMA) model [29] is applied to calculate the crystallization fraction X . The numerical crystallization fraction is expressed as

$$X = 1 - \exp \left[- \left(\int_0^t (1/\tau) dt \right)^n \right], \quad (4.3.1),$$

where n is the Avrami parameter and τ is the crystallization time. τ can be expressed as

$$\tau = \tau_0 \exp \left[\frac{E_a}{k_B T} + \left(\frac{A}{(T_m - T)^2 T} \right) \right] \quad (4.3.2),$$

where T is the temperature, T_m is the melting point, E_a is the activation energy, k_B is the Boltzmann constant and τ_0 is the minimum crystallization time. The minimum crystallization time, τ_0 , is given by

$$\tau_0 = \tau_{\min} \exp \left[- \left(\frac{E_a}{k_B T_N} + \frac{A}{(T_m - T_N)^2 T_N} \right) \right] \quad (4.3.3),$$

where τ_{\min} is the minimum crystallization, T_N is the nose temperature of isothermal time-temperature-transformation (TTT) diagram and the constant A is given by

$$A = \frac{E_a (T_m - T_N)}{k_B (3T_N - T_m)}. \quad (4.3.4),$$

4.4 Summary

In this chapter, the basic theories and governing equations for optical, thermal and crystallization analyses of optical storage are presented. The numerical methods for solving the optical and thermal models are also explained.

Chapter 5 Design of Blu-ray disc using the developed software

In this chapter, it is illustrated how the software is used to design a Blue-ray disc. Five cases is selected and simulated in order to study the performance of a Blu-ray disc.

5.1 Optical analyses of Blu-ray disc

In this section, the optical modeling of Blu-ray disc is described. The influence of black dot on Blu-ray discs is then investigated.

5.1.1 Geometry modeling of Blu-ray disc

The Blu-ray disc is modeled as a rectangular stack with a length of 0.7 μm and a width of 0.7 μm . It is made of thin film materials, namely the polycarbonate substrate, the ZnS-SiO₂ dielectric, the Ge₂Sb₂Te₅ phase change layer, the reflective layer and the polycarbonate cover layer. The sample size in the simulation has been chosen based on the assumption that a beam radius of 0.5 μm will be well contained within the perimeter of the chosen dimension.

One important point to note is that the substrate is modeled as having a thickness of 0.2 μm instead of its actual thickness of 0.1mm. The simplification is made because of huge difference in the order of magnitude between the thickness of the deposited thin films (10^{-9}m) and that of the substrate (10^{-3}m), which leads to large amount of elements for cover layer. Large amount of elements consume huge of memory and cause a long simulation time, therefore the number of elements is limited to 300,000.

Figure 5.1 shows the geometry of the Blu-ray disc used in the simulation and Table 5.1 shows the optical properties of the materials involved.

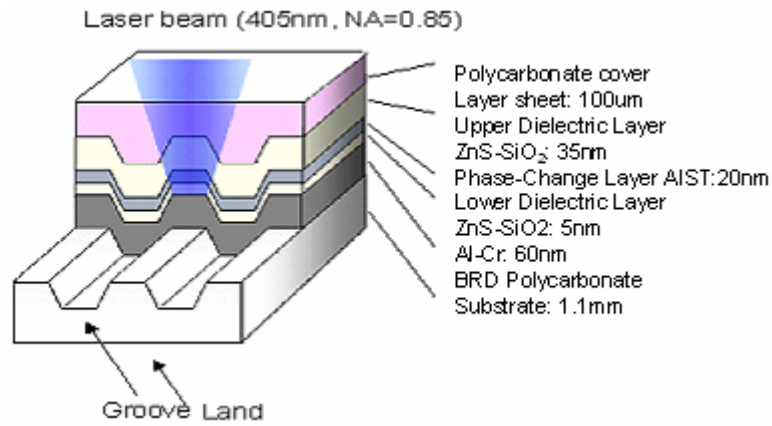


Figure 5.1 Blu-ray disc structure

Table 5.1 Optical properties of Materials

Material type	Refractive Index n	Extinction Coefficient K	DC response of the polarization χ_0	Permittivity of infinity frequency ϵ_∞
Cover layer	1.569	0.03	-	-
Dielectric	2.129	0.00	-	-
Phase change	Amorphous	4.8756	1.932	-
	Crystalline	4.75	4.349	-
Reflective layer - Al-Ar	1.438	5.035	80	2.5281
UV Resin	1.569	0.03	-	-
Substrate	1.569	0.03	-	-

5.1.2 Simulation conditions and FDTD meshing

In our simulation, we use $\Delta x = 0.01\mu\text{m}$, $\Delta y = 0.01\mu\text{m}$ and $\Delta z = 0.0062\mu\text{m}$. While meshing the disc, a balance has to be struck between having a fine mesh and having a short computation time. The mesh details are shown in Table 5.2. Figure 5.2 shows the disc geometry while Table 5.3 gives the simulation parameters.

Table 5.2 FDTD mesh details

Number of elements along x axis	60				
Number of elements along y axis	60				
Number of elements along z axis	Cover layer	Dielectric	Phase Change	Dielectric	Reflective layer
	32	17	3	4	16
Total nodes	60x60x76=273,600				

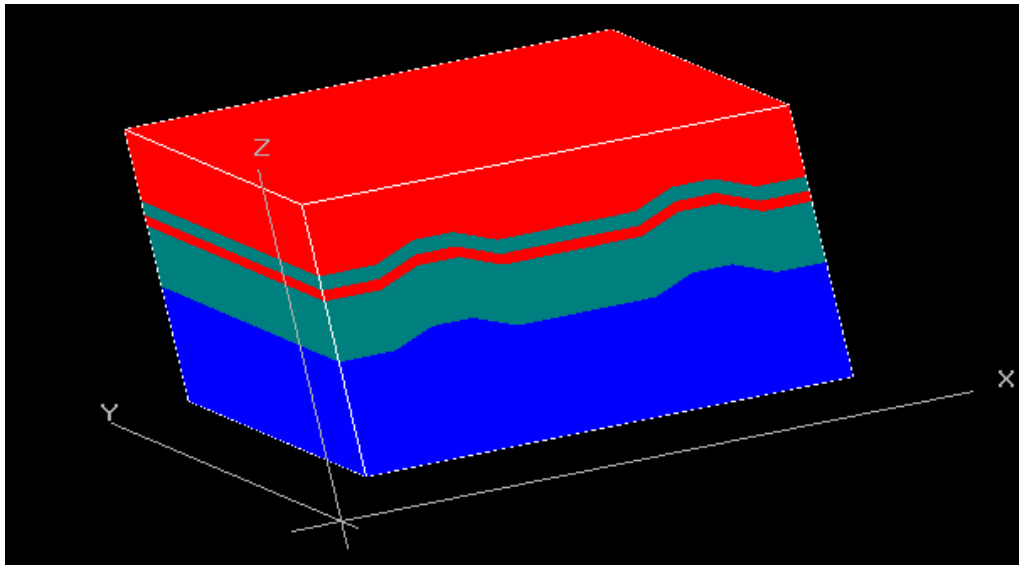


Figure 5.2 Disc model for FDTD analysis

Table 5.3 Simulation parameters

Simulation conditions	
Optical Parameters	
Laser Wavelength (nm)	405
Numerical Aperture	0.85
Disk Parameters	
Track pitch (μm)	0.32
1 st dielectric thickness (nm)	105
Phase change thickness (nm)	20
2 nd dielectric thickness (nm)	22
Reflective thickness (nm)	100
Groove depth (nm)	20~30
Sidewall angle ($^{\circ}$)	25~35

5.1.3 The effects of black dot on Blu-ray discs

The black dot is assumed to be a circular obscuration with a radius of 0.2mm, a thickness of 0.01mm and an offset of 0.16mm from the center of recording track on

the cover layer surface. Figure 5.3(a) and Figure 5.3(b) show the beam profile without black dot and one with a black dot with 0.01mm offset from the center of the recording track, respectively. It can be seen that the beam profile is distorted from circular shape to rectangle shape in the latter and the peak intensity decreased from 70.3% to 55.7%. Figure 5.4 and Figure 5.5 show the near field intensity distribution with written mark at center of the disc without black dot and the disc with de-centered black dot, respectively. It can be seen that the disc with de-centered black dot has lower intensity compared with the disc without black dot. The disc with black dot also shows asymmetry intensity distribution along cross track with the left side having higher intensity compared with the right as shown in Figure 5.5(b). Similar results are obtained at the same position for disc with de-centered mark as shown in Figure 5.6 and Figure 5.7, respectively. The disc without de-centered black dot has higher intensity than that with black dot and the disc with de-centered black dot also shows asymmetric intensity distribution.

Figure 5.8 shows the read back signal obtained from the disc without black dot and the disc with de-centered black dot. The modulated amplitude of the disc without black dot is 0.0866 while the disc with de-centered black dot is 0.049. It is clear that the disc with de-centered black dot has lower modulated amplitude. Here modulated amplitude is defined as $(\text{maximum read out signal} - \text{minimum read out signal}) / \text{maximum read out signal}$.

The full width at the half maximum (FWHM) of the read back signal for the disc without black dot is 0.36 μm and the disc with de-centered black dot, 0.4 μm . It shows that the disc with de-centered black dot has a broader FWHM of read back signal.

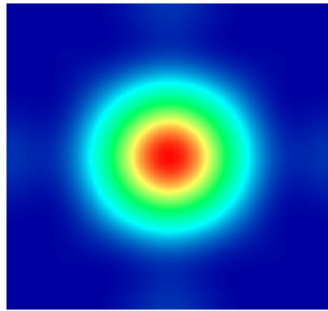
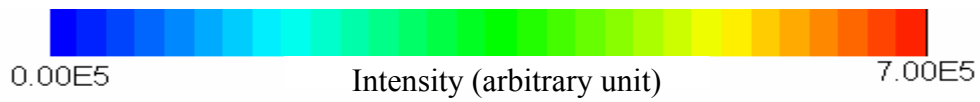


Figure 5.3(a) Beam profile of the disc without black dot

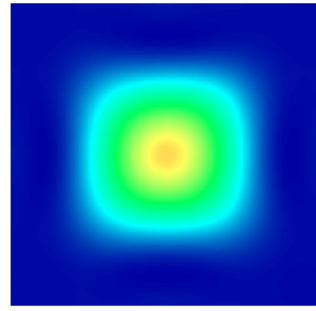
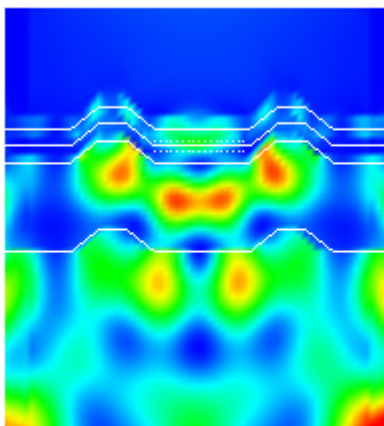
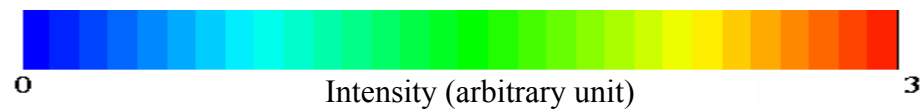
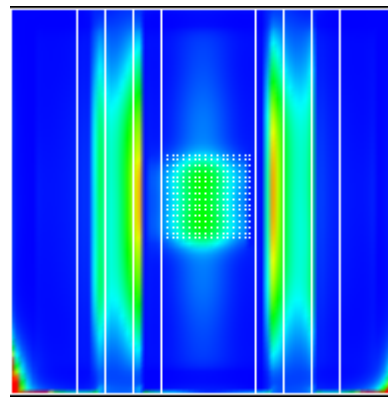


Figure 5.3(b) Beam profile of disc with black dot (0.01mm offset from center of the recording track)

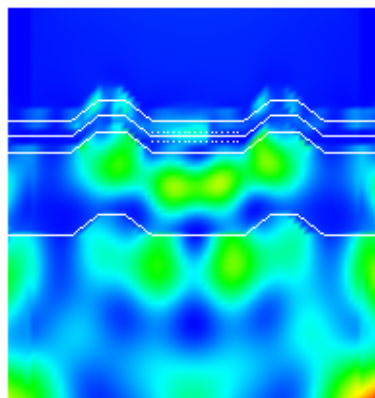


(a) Side view

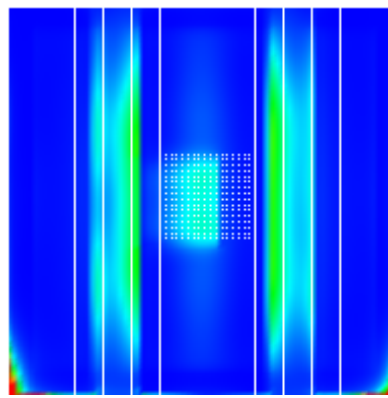


(b) Top view

Figure 5.4 Near field intensity distribution of the mark at the center of disc without black dot



(a) Side view



(b) Top view

Figure 5.5 Near field intensity distribution of the mark at the center of disc with black dot

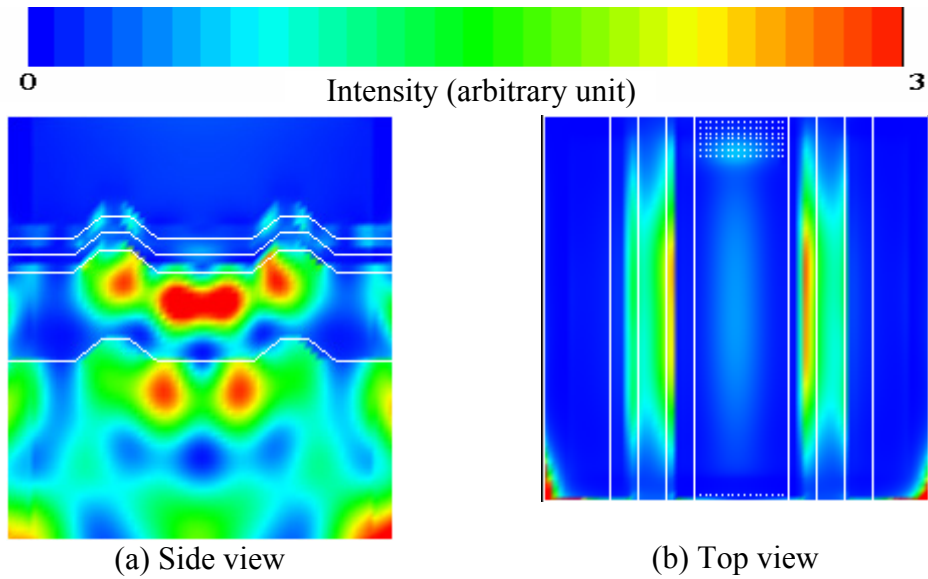


Figure 5.6 Near field intensity distribution of the disc without black dot

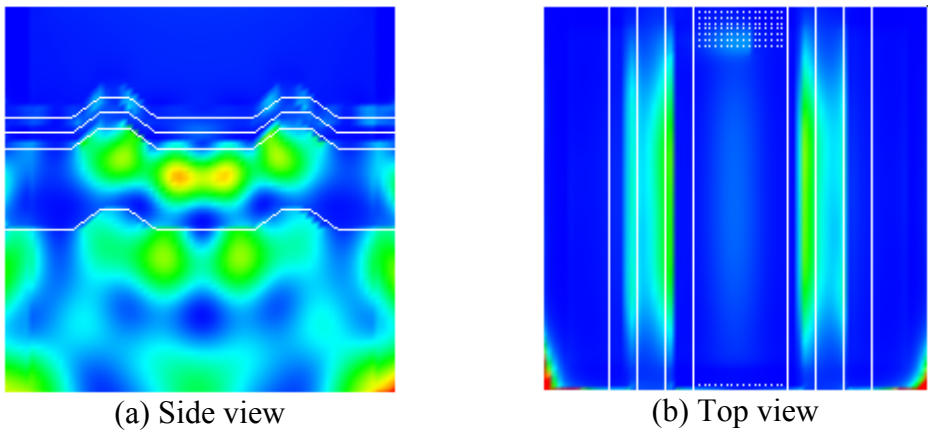


Figure 5.7 Near field intensity distribution of the disc with black dot

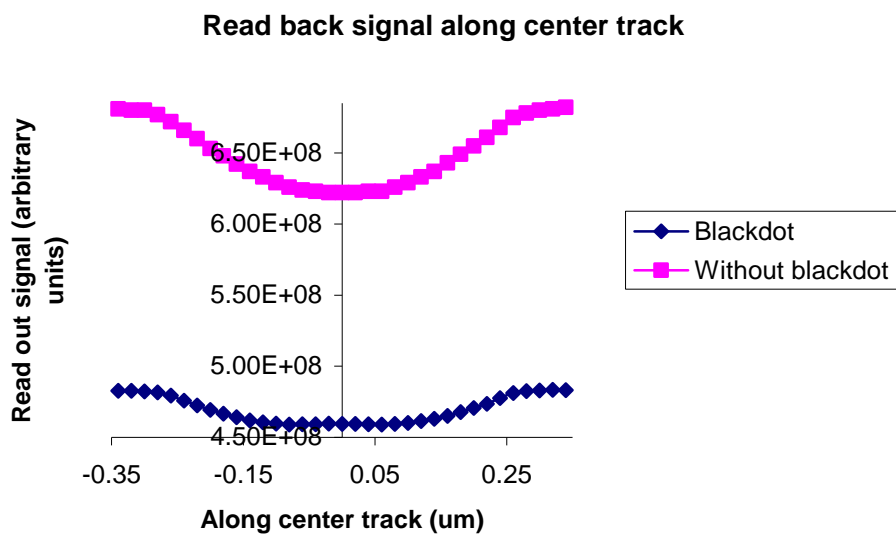


Figure 5.8 Read back signal along center track

5.2 Thermal analyses of Blu-ray disc

In this section, the thermal modeling of Blu-ray disc is be described. The influence of disc tilt, cover layer thickness, surface scratches and black dot on the thermal effects of laser beam is investigated.

5.2.1 Geometry modeling of Blu-ray disc

The Blu-ray disc is modeled as a rectangular stack with a length of $1\mu\text{m}$ and a width of approximately $0.8\mu\text{m}$. It is made up of thin film materials, namely the polycarbonate substrate, the ZnS-SiO_2 dielectric, the AgInSbTe phase change layer, the reflective layer and the polycarbonate cover layer. The sample size in the simulations has been chosen based on the assumption that the heating effect caused by an incident laser beam is confined within a radius of $0.5\mu\text{m}$, therefore, the laser beam is well contained within the perimeter of the chosen dimension.

One important point to note is that the substrate is modeled as having a thickness of $0.2\mu\text{m}$ instead of its actual thickness of 0.1mm . The reasons for the simplification are as follows:

- 1) Through numerous simulations, it has been found that the thermal effects within the disc do not extend beyond $0.5\mu\text{m}$ into the substrate and cover layer.
- 2) Huge difference in the order of magnitude between the thickness of the deposited thin films (10^{-9}m) and that of the substrate (10^{-3}m) would affected the accuracy of calculation.

Based on the two aforementioned considerations, it is decided that a $0.2\mu\text{m}$ thick substrate can be used to obtain reliable results. Figure 5.1 shows the geometry of a

Blu-ray disc used in the simulation and Table 5.4 shows the material properties of various layers in a Blu-ray disc.

Table 5.4 Material properties of various layers in a Blu-ray disc

Material type	Density (Kg/m ³)	Heat Conductivity (J/mKs)	Heat Capacity (J/KgK)	Refractive Index n	Extinction Coefficient k	
Cover layer	1200	0.22	1172	1.569	0.03	
Dielectric	3650	0.6	560	2.129	0	
Phase change	Amorphous	6150	0.5	210	4.8756	1.932
	Crystalline	6150	0.5	210	4.75	4.349
Reflective layer - Al-Ar	2750	25	890	1.438	5.035	
UV Resin	1200	0.22	1172	1.569	0.03	
Substrate	1200	0.22	1172	1.569	0.03	

5.2.2 FEM meshing

While meshing the disc, a balance has to be struck between a fine mesh and a short computation time. Thus the layers within the geometric model, namely the phase change and dielectric layers, which are of greater interest, are finely meshed, while those which are far away from the phase change layer-substrate such as the reflective layer and the cover layer, are meshed more coarsely. Table 5.5 shows the mesh details of the Blu-ray disc and Figure 5.9 shows the finite element model of the Blu-ray disc mesh.

Table 5.5 Blu-ray disc mesh details

Number of elements at x axis	80					
Number of elements at land track	4					
Number of elements at groove track	6					
Number of elements at z axis	Cover layer	Dielectric	Phase Change	Dielectric	Reflective layer	Substrate
	3	3	2	1	3	3
Total nodes	34,992					
Total elements	31,200					

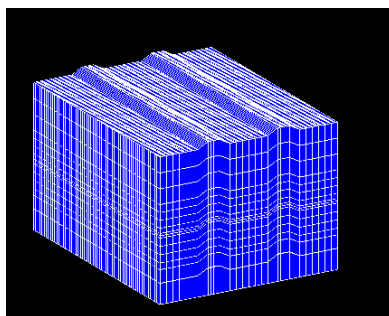


Figure 5.9 Finite element model of Blu-ray disc

5.2.3 Simulation conditions

The simulation conditions defined in for the thermal analyses of the Blu-ray disc are listed in Table 5.6. We divide the parameters into three categories namely optical, system and disc parameters. The values of these parameters are chosen carefully to meet the phase change optical disc standards so that the results obtained from this research can be compared with that of commercial Blu-ray discs.

Table 5.6 Simulation conditions

Simulation conditions	
Optical Parameters	
Laser Wavelength (nm)	405
Numerical Aperture	0.85
Laser power (mW)	1~8
System Parameters	
Rotation speed (m/s)	5.28
Disk Parameters	
Track pitch (μm)	0.32
1 st dielectric thickness (nm)	105
Phase change thickness (nm)	20
2 nd dielectric thickness (nm)	22
Reflective thickness (nm)	100
Groove depth (nm)	20~30
Sidewall angle ($^{\circ}$)	25~35

In all simulations, the disc material is assumed to be isotropic, homogenous and non-temperature dependent. It is assumed that the laser energy is only absorbed in the phase change layer, which means that heat is only generated in that layer. A 50ns

rectangular laser pulse is applied. The initial and boundary temperature is set at room temperature 27°C.

5.2.4 The effects of disc tilt on thermal behavior of Blu-ray disc

Large optical path difference (OPD) along pupil's X coordinate (in tangential direction) is induced by tangential tilt as shown in Figure 5.10. The OPD represents the phase error of the wave front forming an image. Any deviations from zero OPD contribute to a degradation of the diffraction image formed by the optical system. As a result of large OPD of pupil's X coordinate, the beam spot shifts to the right when the tangential tilts as illustrated in Figure 5.11. Figure 5.12 shows the effect of tangential tilt on the position of the mark, while Figure 5.13(a) and Figure 5.13(b) show the temperature profile along center track (mark length) direction and along cross track (mark width) direction, respectively, for tangential tilt angles of 0.0°, 2.0° and 4.0°.

From the results of Figure 5.13(a) and Figure 5.13(b), it can be seen that tangential tilt contributes more thermal distortions along track direction compared with cross track direction, which will affect the mark length formation compared with along cross track. Figure 5.13(a) shows that the whole thermal profile shifts toward positive direction when tangential tilt angles increases, which corresponds to the mark shifting to the right as the tangential tilt angle increases as shown in Figure 5.12. The peak temperature of a disc with a tangential tilt of 2.0° shifts about 5nm which is almost 9% of an1T Blu-ray mark length from its original position (when the disc does not tilt) and the peak temperature in the case of a tangential tilt of 4.0° shifts about 10nm. This will cause timing jitter when signal is read back. The temperature profile along cross track direction for the disc with a tangential tilt of 2.0° and a tangential tilt of 4.0° are almost similar with the case without tilt as shown in Figure 5.13(b).

In contrast to tangential tilt, the radial tilt induced a large OPD of pupil's Y coordinate (in radial direction) as shown in Figure 5.14. Figure 5.15 illustrates the beam profiles of radial tilts obtained from ZEMAX. Consequence of a large OPD along pupil's Y coordinate is that the beam spot shift slightly towards the bottom of the track when the radial tilt increases. Figure 5.16 shows the location of the mark with the radial tilt angles of 0.0° , 2.0° and 4.0° , respectively, while Figure 5.17(a) and Figure 5.17(b) show temperature profile along center track and cross track for radial tilt angles of 0.0° , 2.0° and 4.0° , respectively. The temperature profile is shifted to the negative direction when the radial tilt increases as shown in Figure 5.17(b). This causes the mark to shift slightly away from the center track as shown in Figure 5.16. The peak temperature of the disc shifts about 10nm from center track for a radial tilt of 2.0° and about 20nm for a radial tilt of 4.0° .

From the results depicted in Figure 5.12 to Figure 5.13 and Figure 5.16 to Figure 5.17, the tangential tilt produces a more significant shifting of the peak temperature along the center track direction than the radial tilt while the radial tilt produced a more significant shifting of the peak temperature along the cross track direction than the tangential tilt.

Optical path difference along pupil's Y coordinate

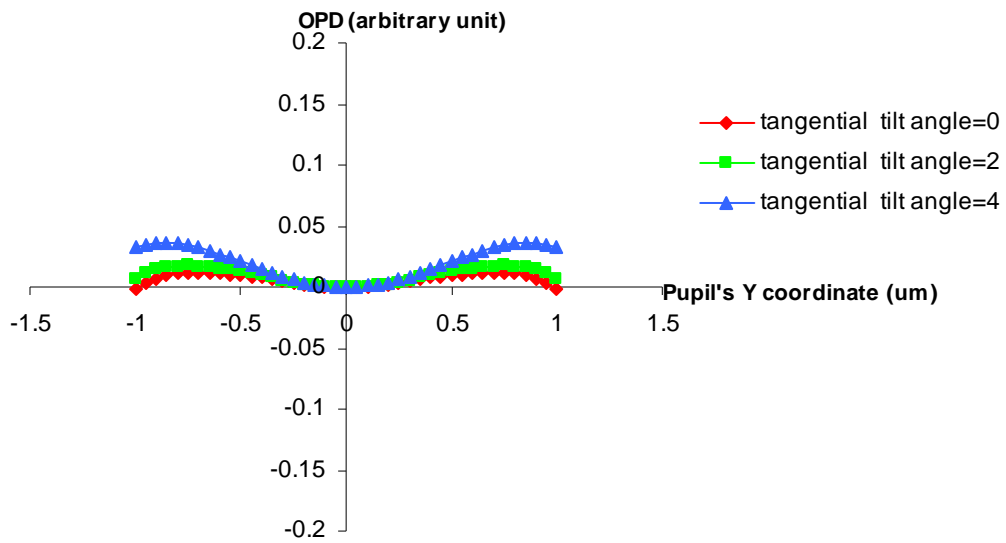


Figure 5.10(a) OPD along pupil's Y coordinate for disc with tangential tilt angles of 0.0°, 2.0° and 4.0°

Optical path difference along pupil's X coordinate

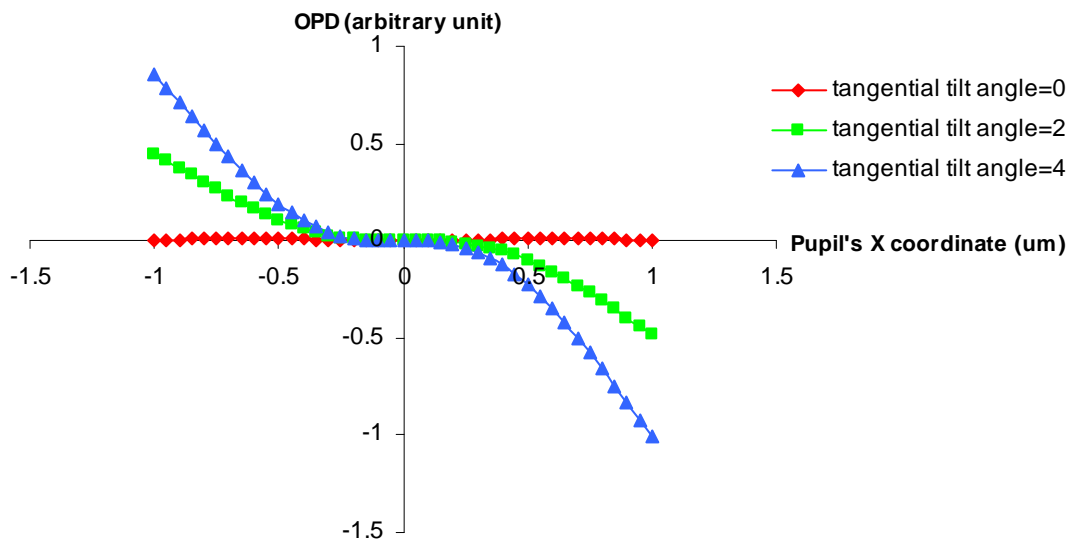


Figure 5.10(b) OPD along pupil's X coordinate for disc with tangential tilt angles of 0.0°, 2.0° and 4.0°

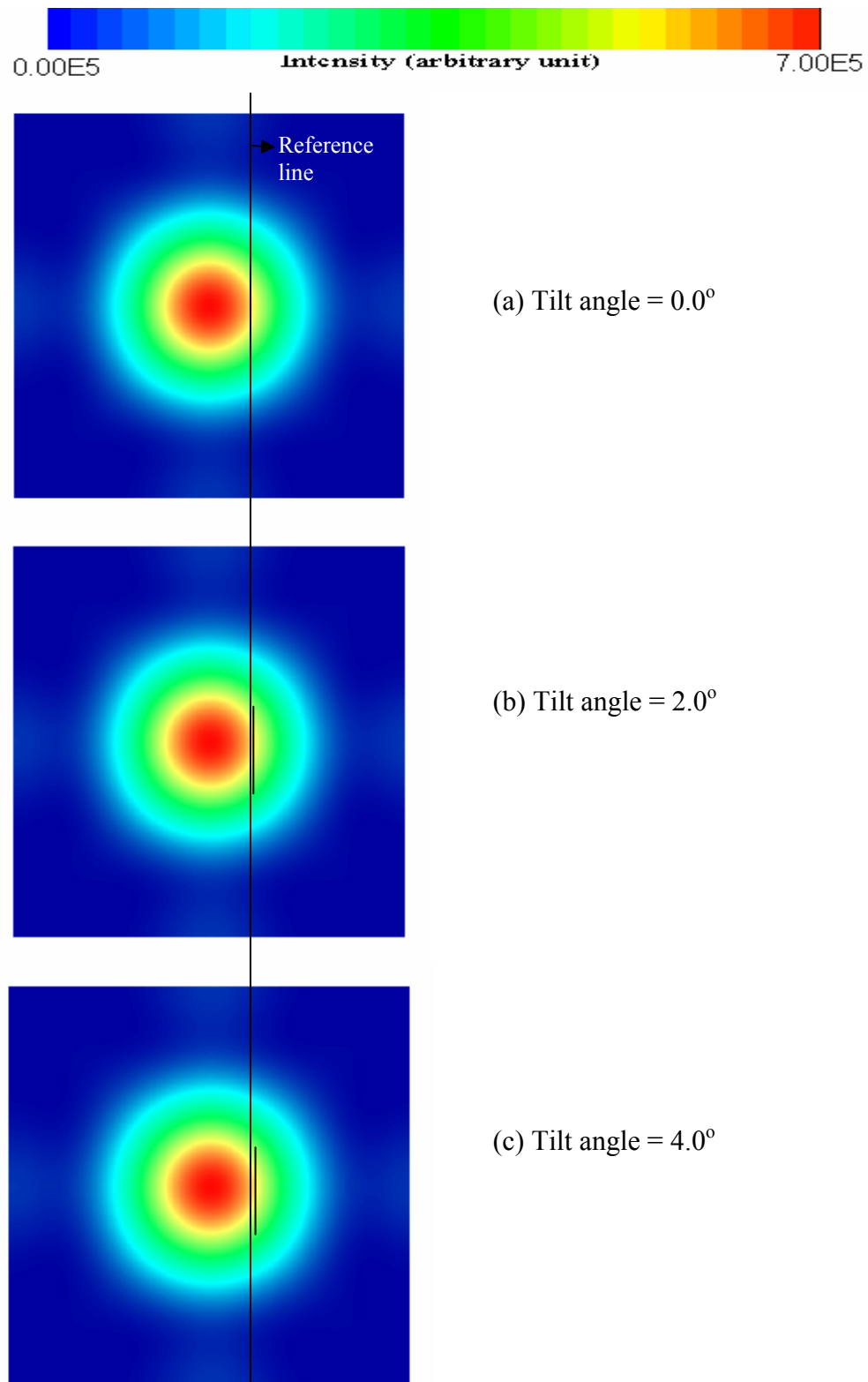


Figure 5.11 The beam profile on Blu-ray disc with tangential tilt angles of 0.0°, 2.0°, 4.0°

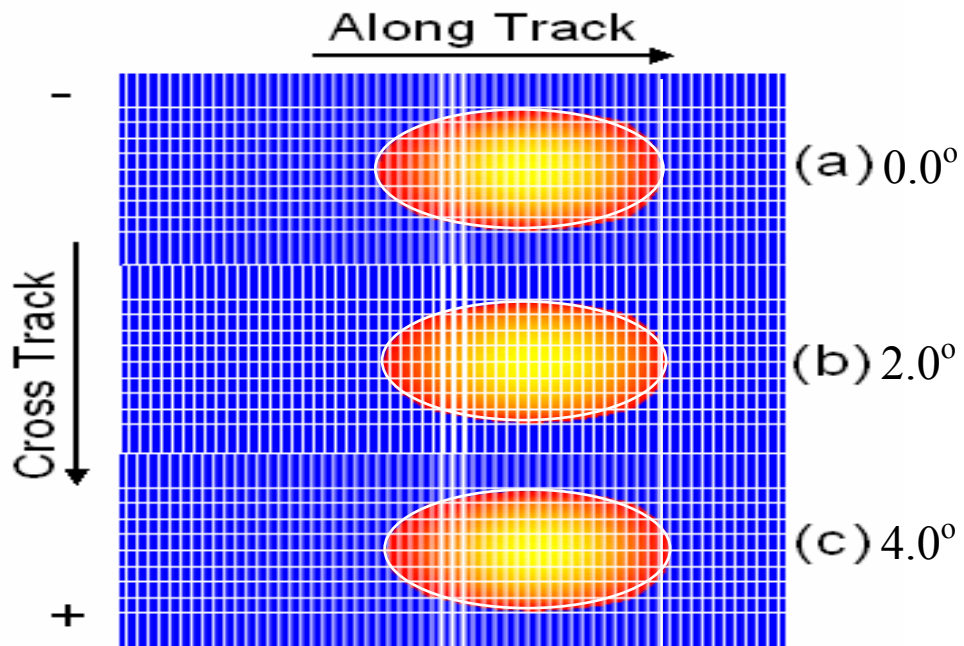


Figure 5.12 Marks shifted with tangential tilt angles of 0.0° , 2.0° and 4.0°

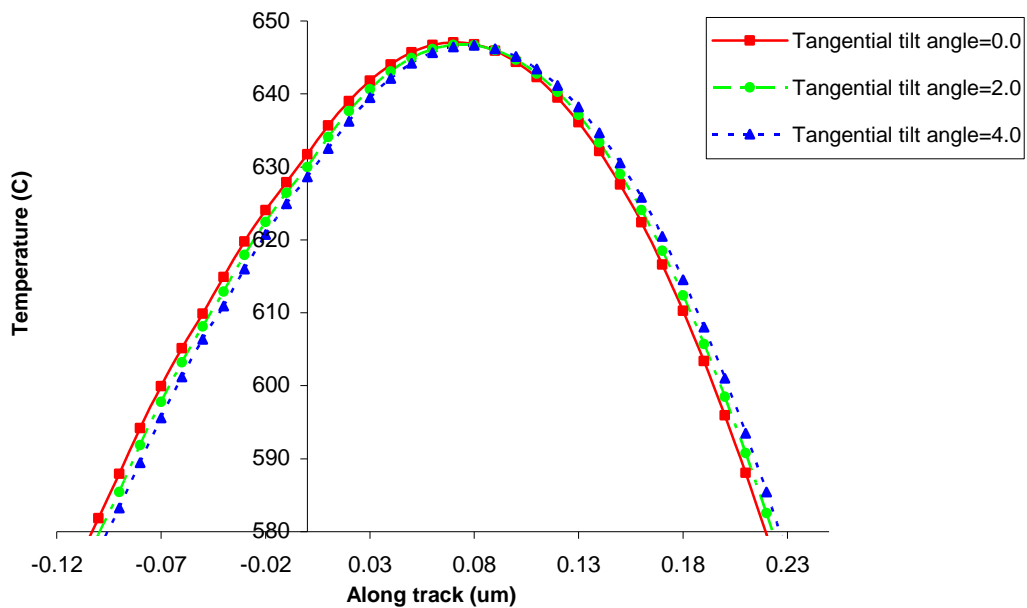


Figure 5.13(a) Temperature along the center tracks with tangential tilt angles of 0.0° , 2.0° and 4.0°

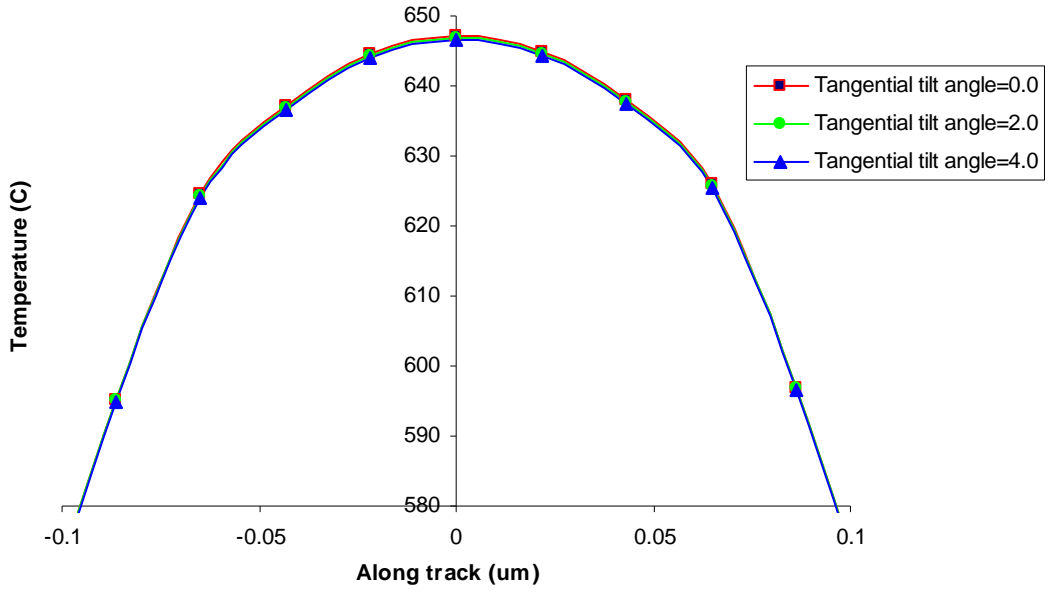


Figure 5.13(b) Temperature along the cross tracks direction with tangential tilt of 0.0° , 2.0° and 4.0°

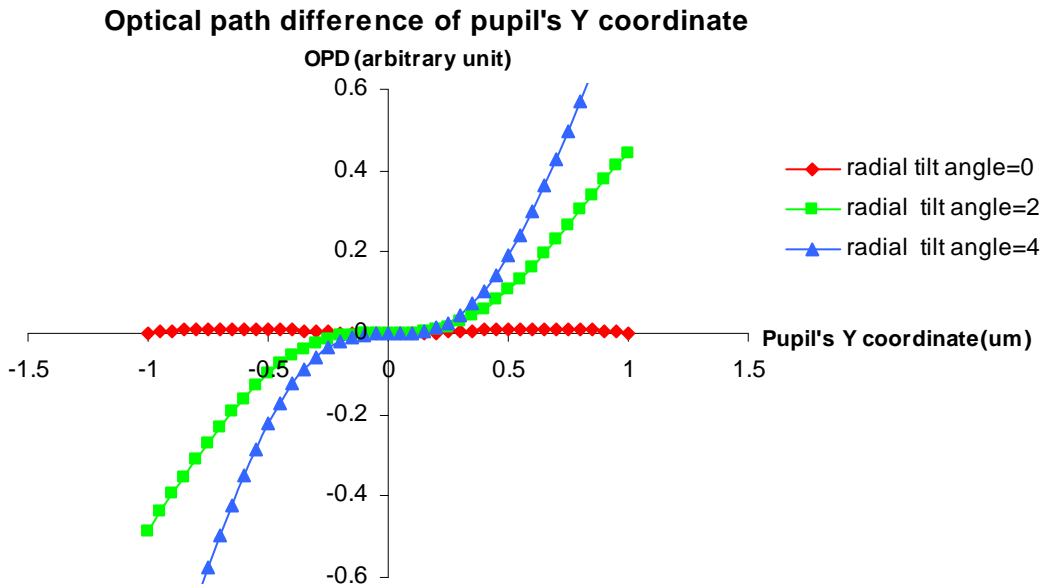


Figure 5.14(a) OPD along pupil's Y coordinate for disc with radial tilt angles of 0.0° , 2.0° and 4.0°

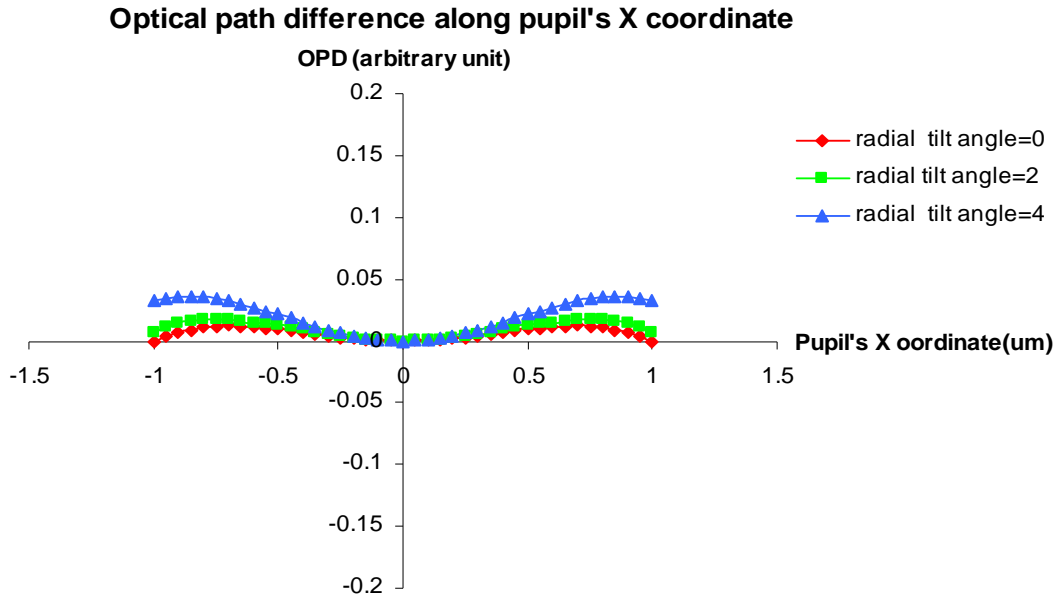


Figure 5.14(b) OPD of pupil's X coordinate for the disc with radial tilt angles of 0.0° , 2.0° and 4.0°

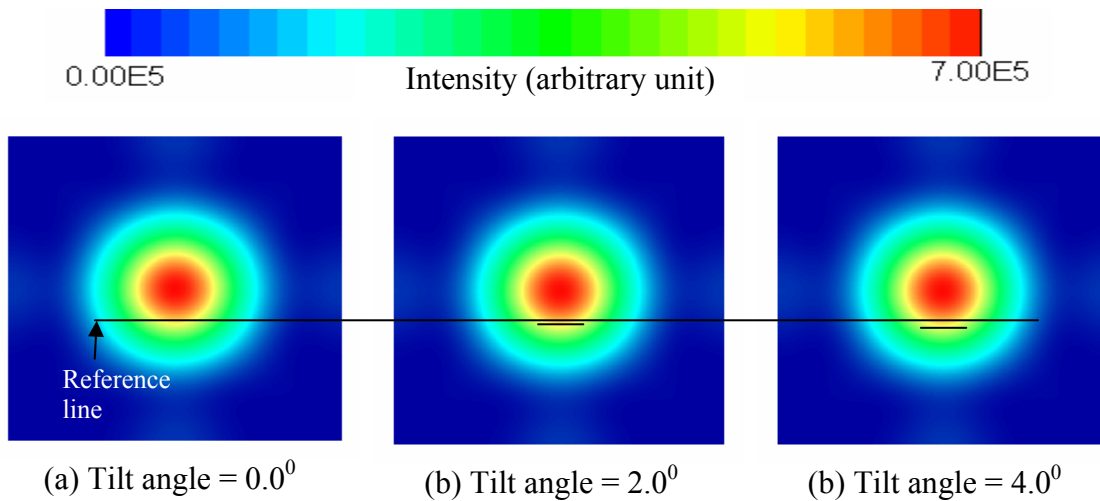


Figure 5.15 The beam profile on Blu-ray disc with radial tilt angles of 0.0° , 2.0° , 4.0°
 Note: X-axis: tangential direction (along track) and Y-axis: radial direction (cross track)

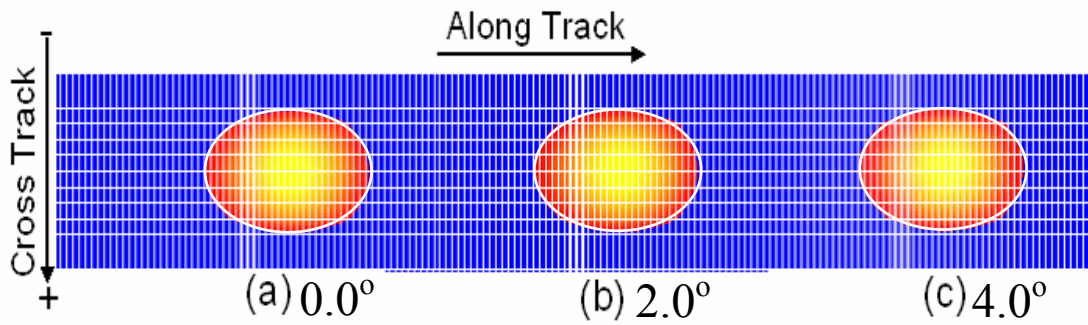


Figure 5.16 Mark shifted with radial tilt angles of 0.0° , 2.0° and 4.0°

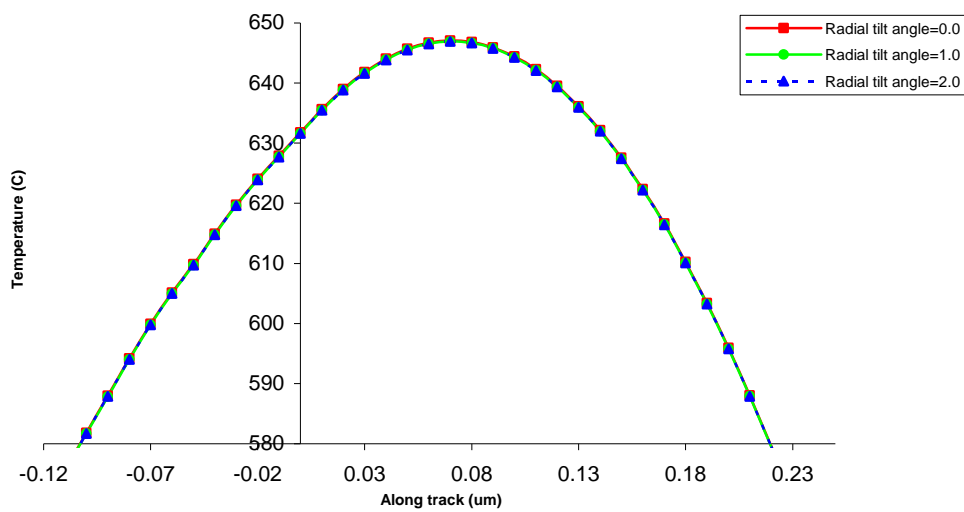


Figure 5.17(a) Temperature along the center track with radial tilt angles of 0.0° , 2.0° and 4.0°

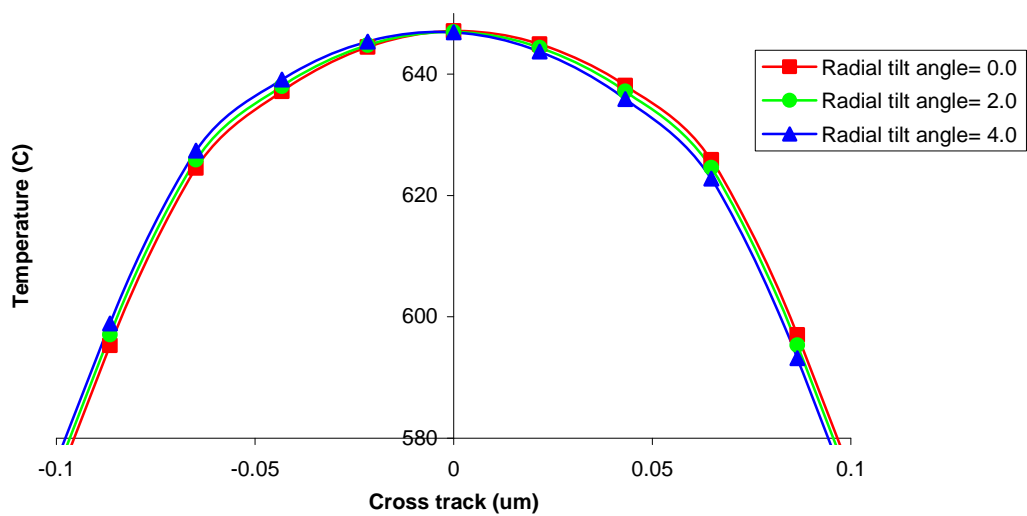


Figure 5.17(b) Temperature along the cross track direction with radial tilt angles of 0.0° , 2.0° and 4.0°

5.2.5 The effects of disc thickness on thermal behavior of Blu-ray disc

Figure 5.18 shows the OPD in both pupil's X and Y coordinates. It can be seen that an increase in the cover layer thickness lead to an increase OPD in both pupil's X and Y coordinates. The beam profiles for different cover layer thicknesses are presented in Figure 5.19. As a result of increasing OPD in both pupil's X and Y coordinates, the beam profile is distorted and the intensity is decreased as the cover layer thickness is increased, as shown in Figure 5.19. Figure 5.20 shows the temperature profile for different cover layer thicknesses. It has been observed that the full width at half maximum (FWHM) of the temperature profile and the temperature are both reduced as the cover layer thickness is increased as shown in Figure 5.20. Consequently, the mark size becomes smaller or no mark is written at all when the thickness of cover layer is increased further as shown in Figure 5.21.

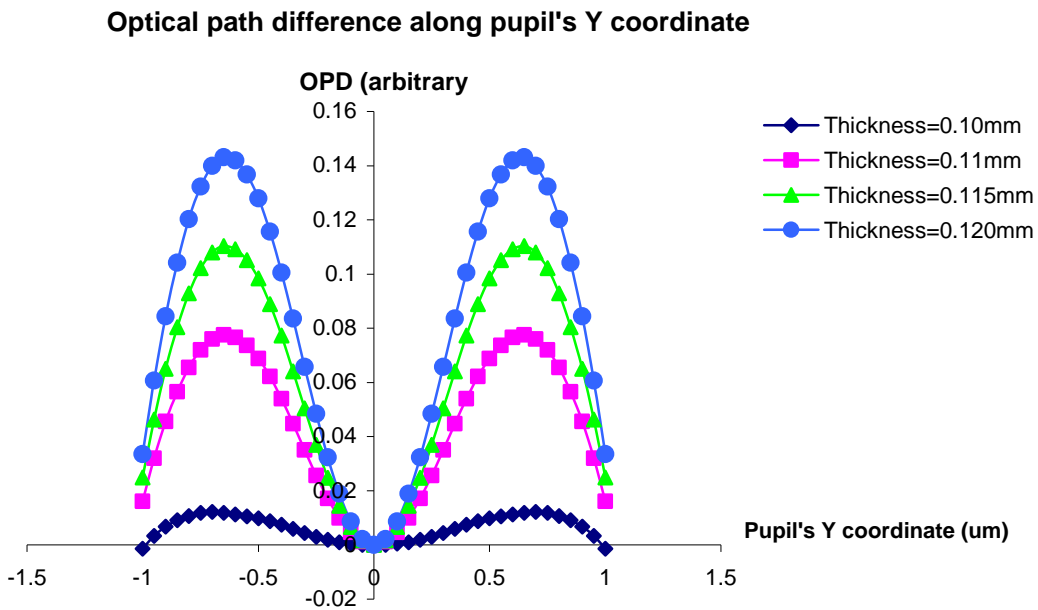


Figure 5.18(a) OPD along pupil's Y coordinate for disc with cover layer thickness of 0.1, 0.11, 0.115 and 0.12mm

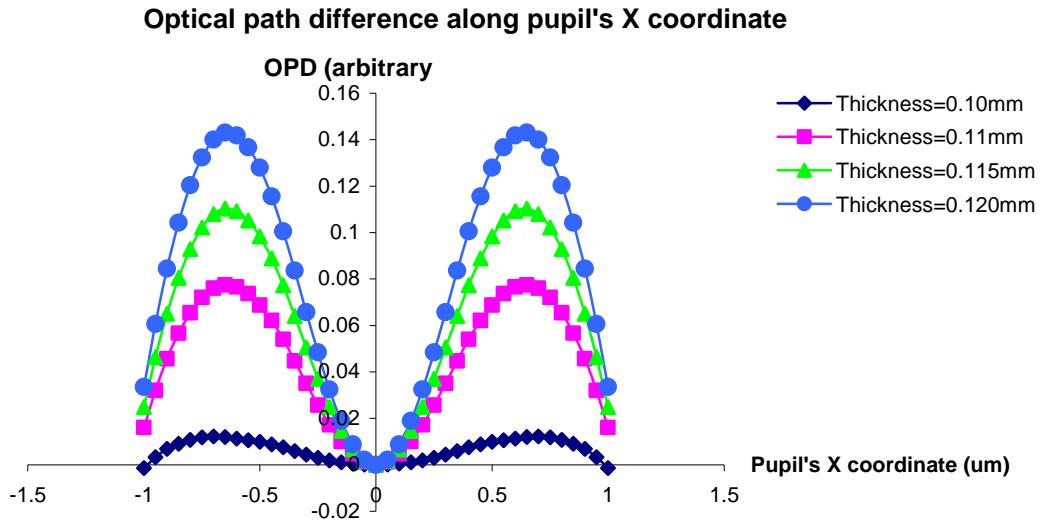


Figure 5.18(b) OPD along pupil's X coordinate for disc with cover layer thickness of 0.1, 0.11, 0.115 and 0.12mm

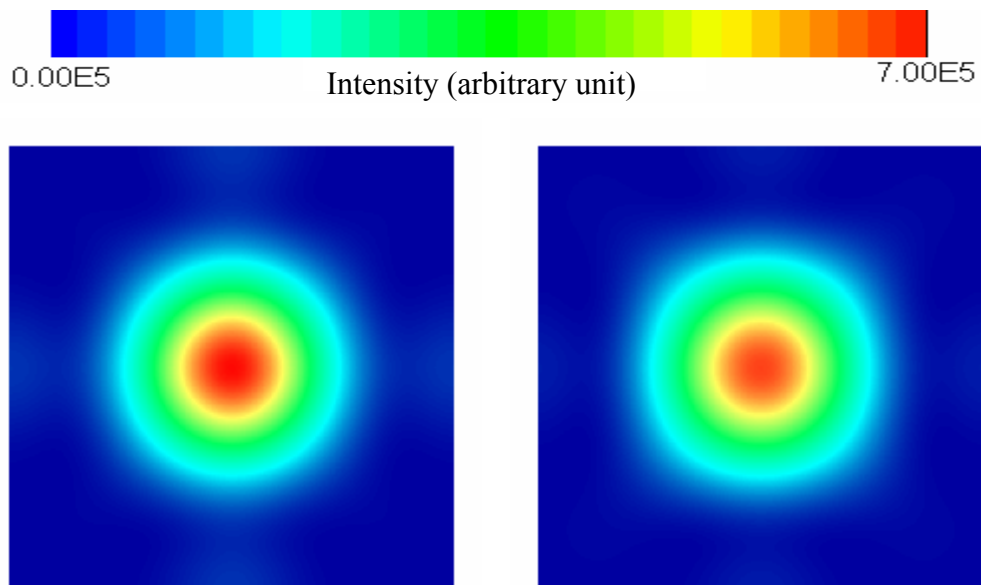


Figure 5.19(a) Beam profile on the disc with cover layer of thickness 0.1mm

Figure 5.19(b) Beam profile on the disc with cover layer of thickness 0.1mm

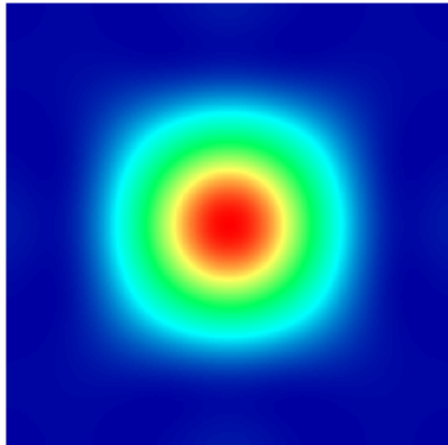


Figure 5.19(c) Beam profile on the disc with cover layer of thickness 0.115mm

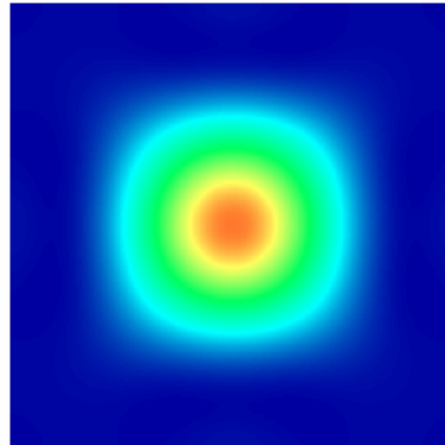


Figure 5.19(d) Beam profile on the disc of thickness 0.12mm

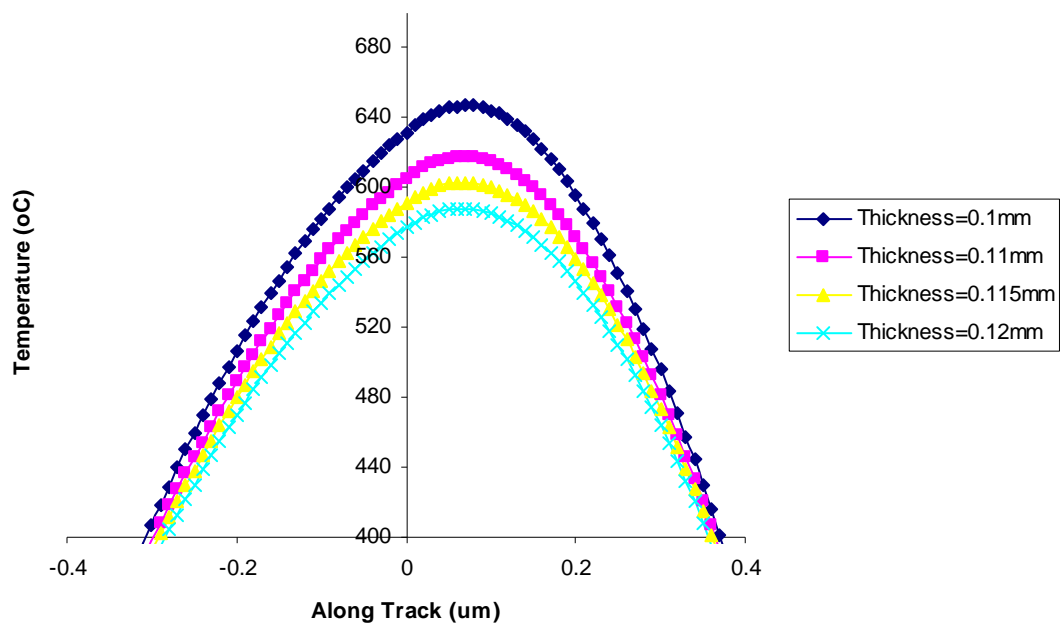


Figure 5.20 Temperature profile along the center track of the disc with cover layer of thicknesses 0.1, 0.11, 0.115 and 0.12mm

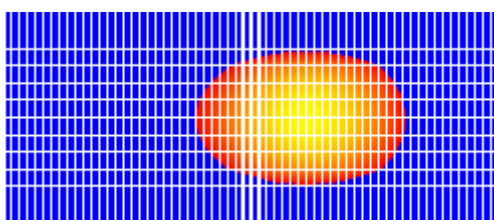


Figure 5.21(a) Mark on the disc with cover layer of thickness 0.10mm

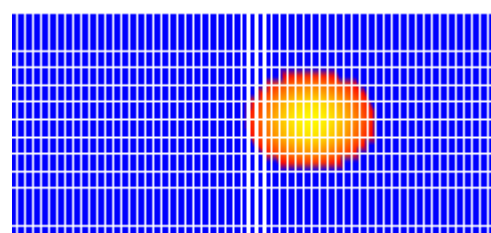
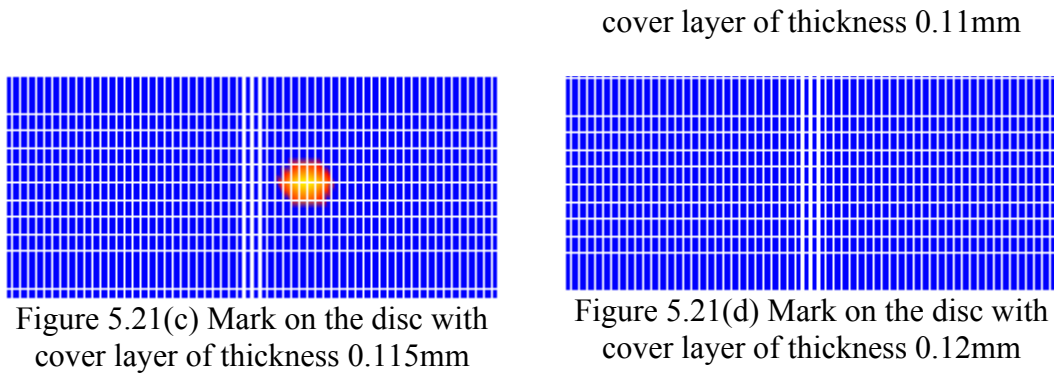


Figure 5.21(b) Mark on the disc with cover layer of thickness 0.12mm



5.2.6 The effects of surface scratches on Blu-ray disc

The scratch is assumed to be a rectangle aperture with 0.8mm length (along track direction) and 0.03mm width (cross track direction) on the cover layer surface. A large aperture size has been chosen to avoid the occurrence of serious diffraction.

Figure 5.22 shows the OPD of the disc without scratch, with scratch and with de-centered scratch (position offset 0.01mm along cross track), respectively. It can be seen that the disc with a scratch at the center has a symmetrical increase in OPD of pupil's Y coordinate. On the other hand, the disc with a de-centered scratch induces an OPD in positive direction of pupil's Y coordinate and deviated from center in negative direction of pupil's Y coordinate. The Three dimensional view of optical path for the lens-to-the disc and beam profile of the disc without scratch, with scratch and with de-centered scratch are illustrated in Figure 5.23, Figure 5.24 and Figure 5.25, respectively. From Figure 5.24, it can be seen that there are slight intensity drop and shape distortion for the beam in the case of a disc with scratch, while the beams shape for the disc with a de-centered scratch is seriously distorted as shown in Figure 5.25. Also, the peak intensity of beam in the case of a de-centered scratch drops drastically from 70.3% (without a scratch) to 31%. The temperature profiles for disc without scratch, with scratch and with de-centered scratch (with an offset of 0.01mm along cross track) are shown in Figure 5.26. It can be seen that for the disc with a

scratch at its center, laser beam causes the peak temperature to drop from 647°C to 634°C . As a result from the temperature drop, the mark written on the disc is smaller than that of the disc without a scratch. The disc with de-centered scratch has the peak temperature drops significantly from 647.08°C to 365.7°C . No mark is therefore written as shown in Figure 5.27 due to the fact that the temperature is lower than the melting point of phase change materials.

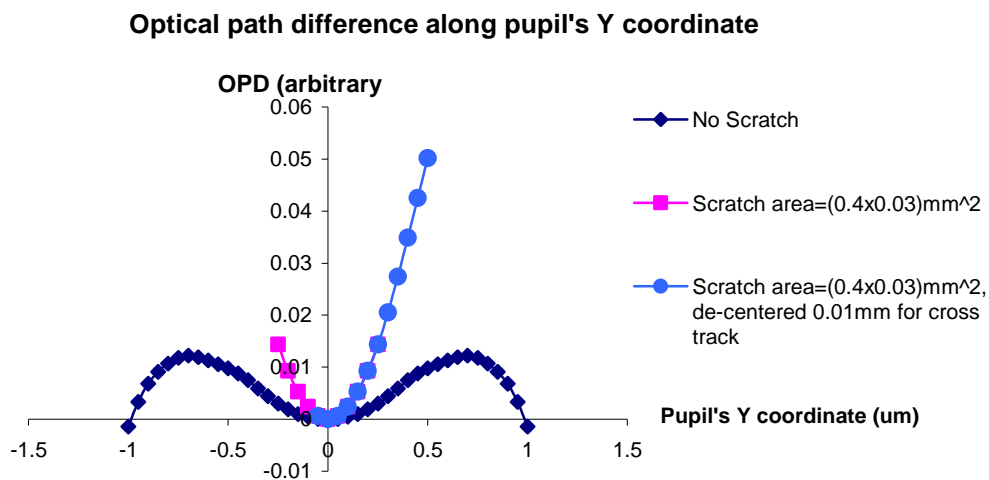


Figure 5.22(a) OPD along pupil's Y coordinate for the disc without scratch, with scratch and de-centered scratch

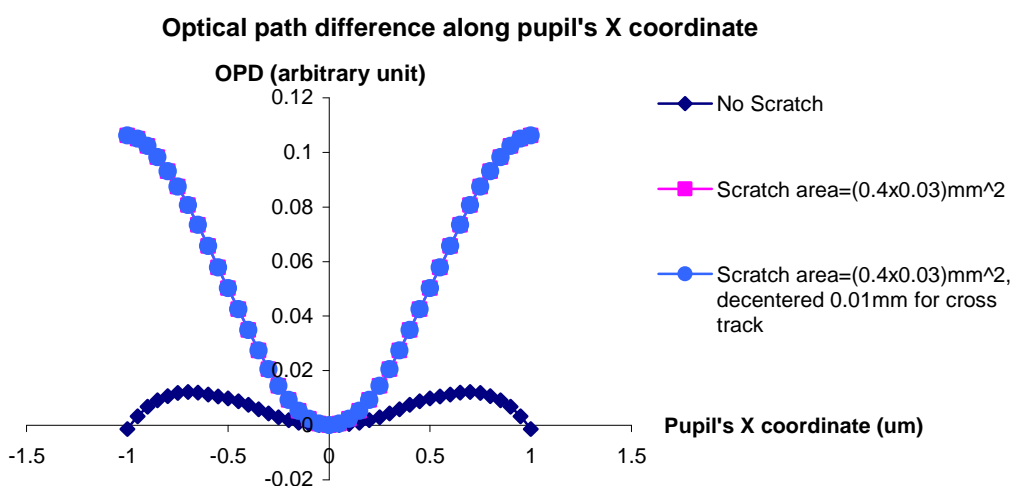


Figure 5.22(b) OPD along pupil's X coordinate for the disc without scratch, with scratch and de-centered scratch

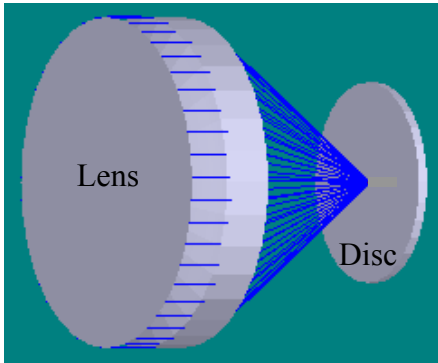
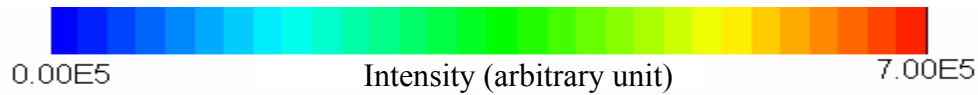


Figure 5.23(a) Three dimensional view of optical path from the lens to the disc without scratch

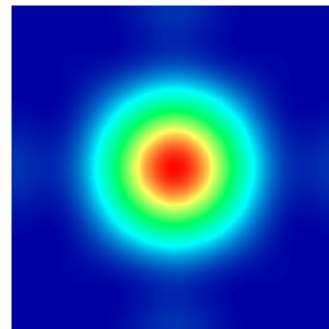


Figure 5.23(b) Beam profile on the disc without scratch

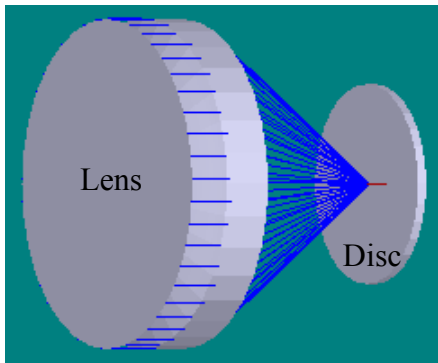


Figure 5.24(a) Three dimensional view of optical path from the lens to the disc with scratch of area 0.8mm x 0.03mm

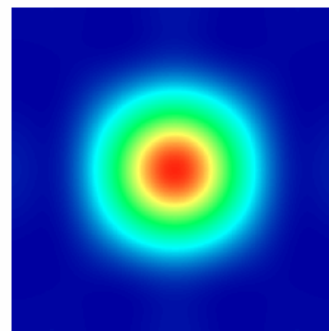


Figure 5.24(b) Beam profile on the disc with scratch area 0.8mm x 0.03mm

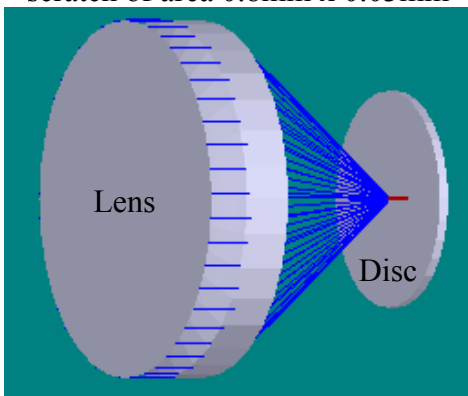


Figure 5.25(a) Three dimensional view of optical path from the lens to the disc with scratch of area 0.8mm x 0.03mm and 0.01mm offset along the cross track direction

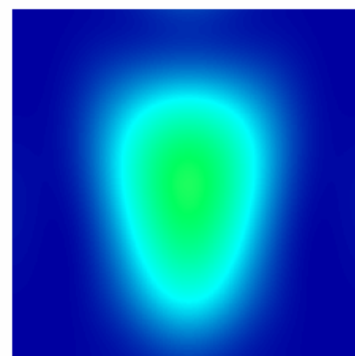


Figure 5.25(b) Beam profile on the disc with scratch area 0.8mm x 0.03mm and an offset of 0.01mm along the cross track direction

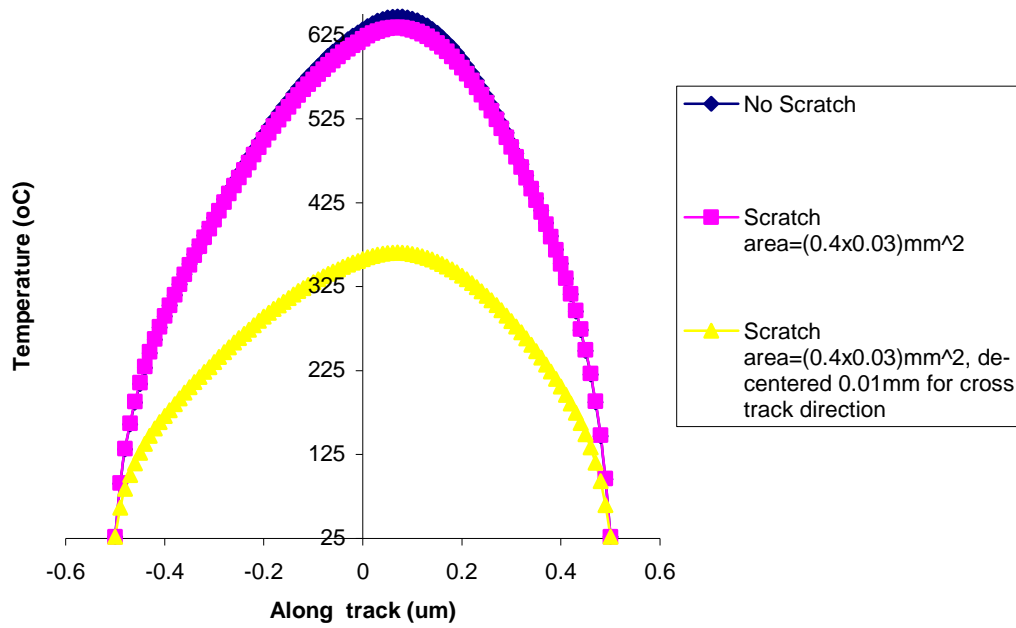


Figure 5.26 Temperature profile along the center track of the disc without scratch, with scratch and with de-centered scratch

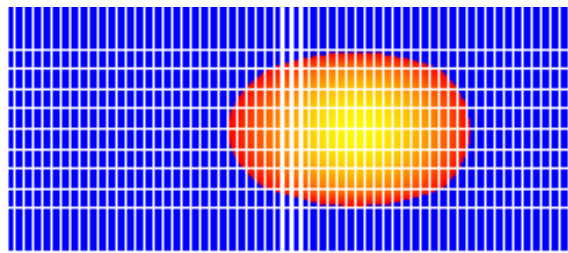


Figure 5.27(a) Mark on the disc without scratch

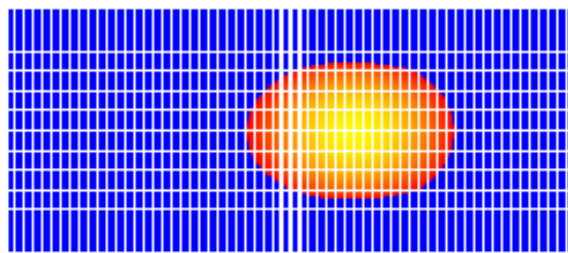


Figure 5.27(b) Mark on the disc with scratch

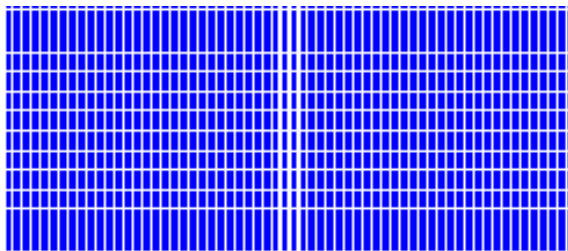


Figure 5.27(c) Mark on the disc with de-centered scratch

5.2.7 The effects of black dot on Blu-ray discs

The black dot is assumed to be a circular obscuration with a radius of 0.2mm, a thickness of 0.01mm and an offset of 0.16mm from the center of recording track on the cover layer surface. From Figure 5.28, it can be observed that the black dot induces a large OPD in the pupil's X and Y coordinates. Figure 5.29(a) and Figure 5.29(b) show the three dimensional of optical path from the lens to the disc and the beam profile on a disc with a black dot which is an offset of 0.01mm from the center of the recording track. As a result of large OPD in both pupil's X and Y coordinates, it can be seen that the beam profile is distorted from circular shape to rectangle shape and the peak intensity decreases from 70.3% to 55.7%. The peak temperature is lower than the melting point of the recording layer due to the decrease of the intensity of the beam spot as shown in Figure 5.30. Consequently, no mark is written on the disc as shown in Figure 5.31.

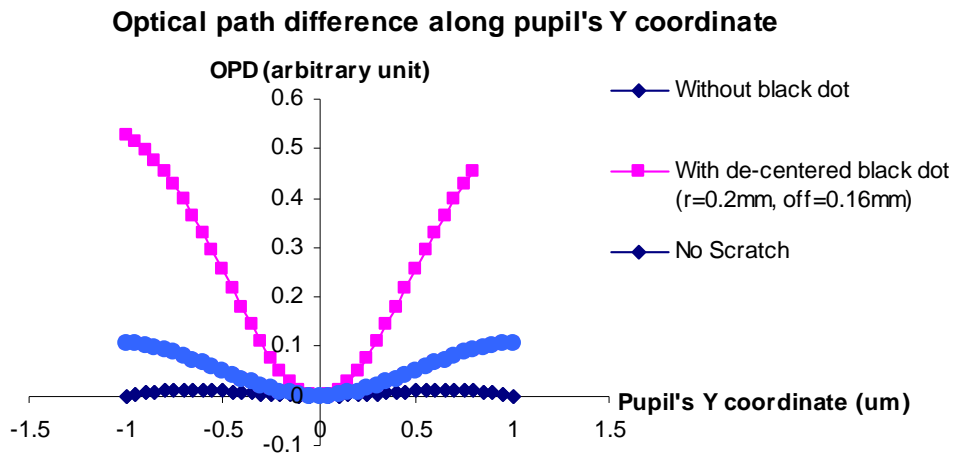


Figure 5.28(a) OPD along pupil's Y coordinate for cover layer without black dot and with black dot

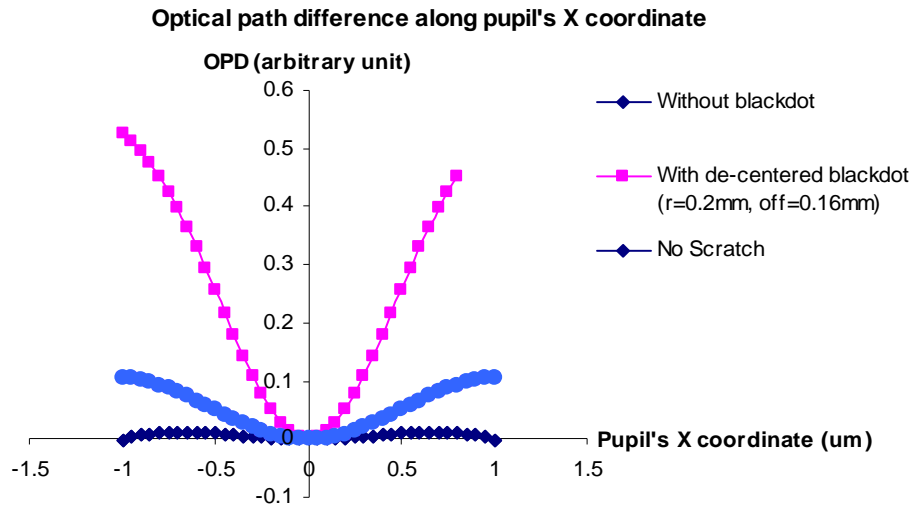


Figure 5.28(b) OPD along pupil's X coordinate for cover layer without black dot and with black dot

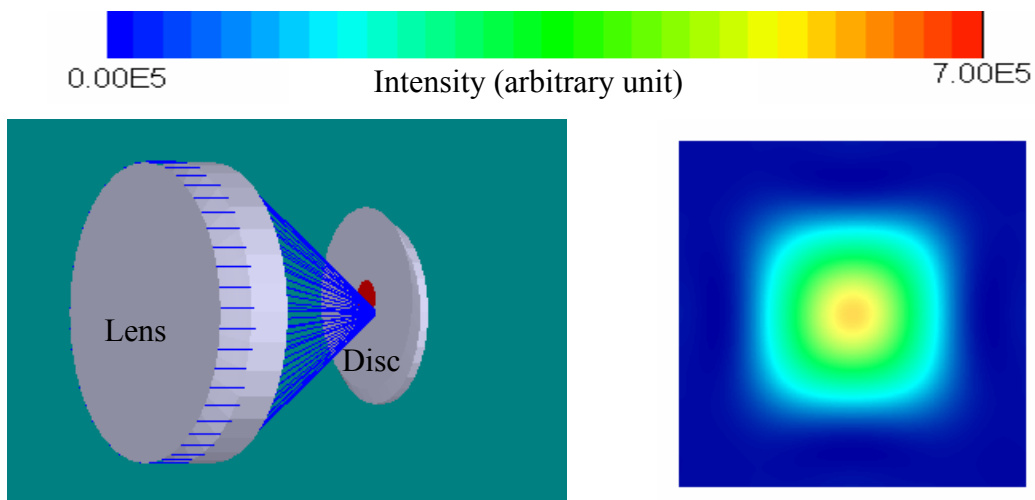


Figure 5.29(a) Three dimensional of optical path from the lens to the disc with a black dot offset 0.01mm from center of the recording track

Figure 5.29(b) Beam profile on the disc with a black dot offset 0.01mm from center of the recording track

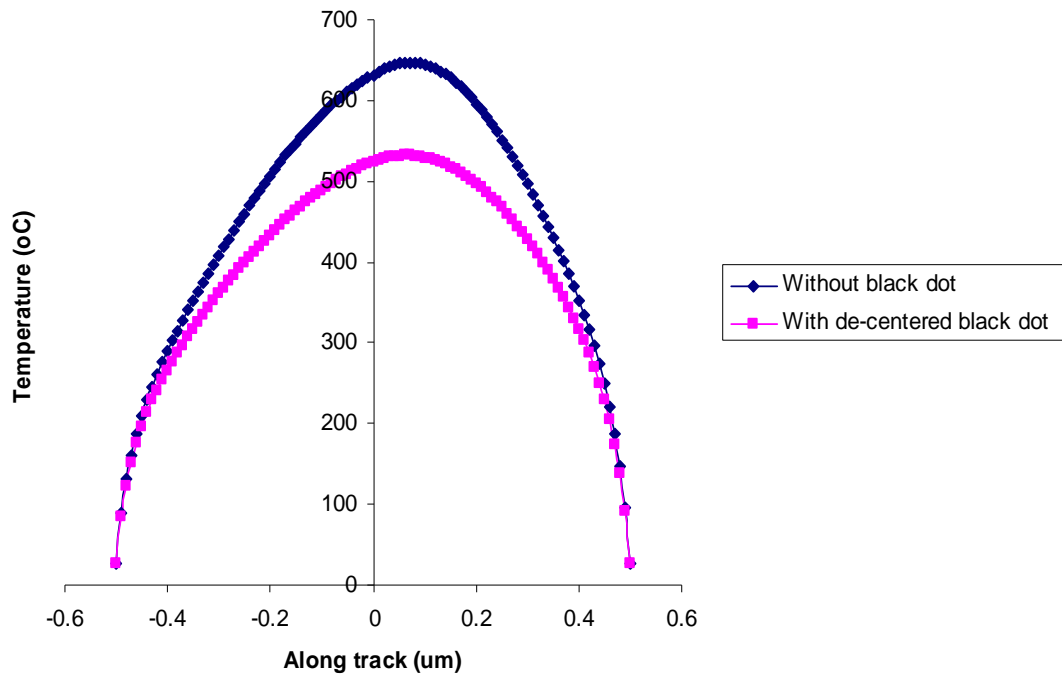
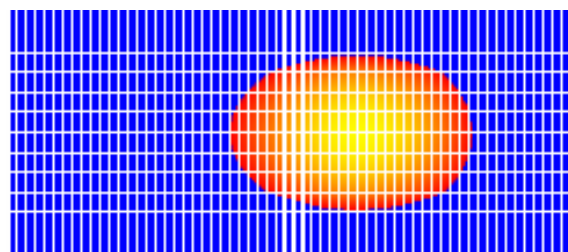
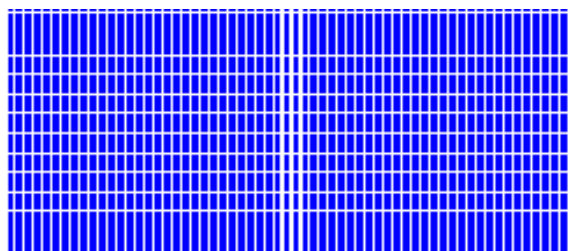


Figure 5.30 Temperature profile along the center track of cover layer without black dot and with black dot



(a) Cover layer without black dot



(b) Cover layer with black dot

Figure 5.31 Mark on disc with cover layer with black dot and without black dot

5.3 Summary

In this chapter, the effects of disc tilt, cover layer thickness, surface scratch and black dot on Blu-ray disc are investigated. As summary of the detailed results have been presented and discussed in various sections of this chapter is highlighted below

They are summarized as follows:

- 1) The disc with a de-centered black dot has lower and asymmetry near field intensity distribution on the phase change layer compared to the disc without a black dot. The disc with a de-centered black dot has also lower modulated amplitude and a broader FWHM of read back signal.
- 2) Tangential tilt can induce a serious mark shifting along the track direction, while radial tilt can induce a significant mark shifting along the cross track direction.
- 3) An increase in the cover layer thickness will increase the OPD in both pupil's X and Y coordinates. Consequently, the beam spot is distorted and the intensity is reduced. It has also been observed that the FWHM of the temperature profile becomes narrower and the temperature decreases as the cover layer thickness increases. The mark size also decreases when the cover layer thickness increases.
- 4) A de-centered scratch on the disc causes a large decrease in writing temperature, as a result, no mark is formed on the disc.
- 5) An offset black dot for center of the recording track induces a large OPD in pupil's X and Y coordinates; as a result, it causes distortion of the beam shape on the disc. Also, it lowers temperature at which writing is carried out.

Chapter 6 Conclusions

- 1) An integrated Optical System and Media Design Software (IOSMDS) has been developed. This integrated software has successfully combined both optical system design and optical media design together.
- 2) An user friendly WINDOW based interface has also been developed. The interactive post process graphical displays such as 2D plot, 3D contours display, 3D-volume visualization tools, 3D animation of temperature distribution, animation of writing and rewriting process, output as text file and output as bitmap file have made the design software a power tool for optical media design.
- 3) While the commercial software ZEMAX is used in the study of optical system design of DVD and Blu-ray discs, the FDTD method developed in this study is used to conduct the optical near-field analysis. This has allowed us to investigate the phenomena happening inside the thin film structure and this will help in the development of new optical storage technology such as Super-RENS. Also, Thermal solver based on FEM method has been incorporated into the integrated software for thermal analysis of optical disc and crystallization modeling methodology based on JMA model which allows the computation of the mark formation.
- 4) The analysis results of the influence of black dot on Blu-ray discs on the optical performance showed that the disc with de-centered black dot has lower and asymmetry near field intensity distribution at phase change layer compare to the disc without black dot. The disc with de-centered black dot has also lower the modulated amplitude and broader the width of half peak to peak read out signal.

- 5) On the analyses of influences of the disc tilt, the cover layer thickness and scratch on the thermal effects in Blu-ray discs, the following results were obtained:
- i) Tangential tilt can induce a serious mark shifting along the track direction, while radial tilt can induce a significant mark shifting along the cross track direction.
 - ii) The increment in the cover layer thickness will increase OPD in both pupil's X and Y coordinates. Consequently the beam spot is distorted and the intensity is reduced. It has also been observed that full width at half maximum (FWHM) of the temperature profile is narrowed and the temperature is decreased as the cover layer thickness increases. The mark sizes also decrease when the cover layer thickness is increased.
 - iii) The de-centered scratch cause a large decreasing of writing temperature, as a result, no mark is forming when writing to the disc with de-centered scratch.
 - iv) The position offset black dot induces a large OPD in pupil's X and Y coordinates, as a results, it cause distortion of the beam spot. Also, it lowers the writing temperature.

References

- [1] D.J. Parker: DVD, the update" CD-ROM Prof. 9(8) 68, (1996).
- [2] Lee Purcell. CD-R/DVD: Disc Recording Demystified. New York: McGraw-Hill, (2000).
- [3] Power point presentation from Optical Storage Lab, National Chung Hsing University, Taiwan, April 24, (2002).
- [4] S.R. Ovshinsky: Reversible Electrical Switching Phenomena in Disordered Structure, Phys. Rev. Lett., 21(20), 1450-1453, (1968).
- [5] T. Ohta, M. Birukawa, N. Yamada, K. Hirao: Optical Recording; Phase-change and Megneto-optical recoding. Journal of Magnetism and Magnetic Materials 242-245, 108-115, (2002).
- [6] N. Akahira, N. Miyagawa, K. Nishiuchi, Y. Skaue and E. Ohno: High Density Recording on Phase Change Optical disks. SPIE. 2514, 294, (1995).
- [7] G.F. Zhou: Material Aspects in Phase Change Optical Recording. Materials Science & Engineering A304-306, 73-80, (2001).
- [8] H. Yamazaki, R. Chiba and I. Hatakeyama: Crystallization Time of the Ternary Ge-Sb-Te Alloys and Their Aptitude to Optical Disk Media at Higher Linear Velocity. Trans. Mat. Res. Soc. Jpn., 15B 1031, (1993).
- [9] H.J. Borg, H.J. Borg, R.V. Woudenberg: Trends in Optical Recording. Journal of Magnetism and Magnetic Materials 193, 519, (1999).
- [10] N. Yamada, E. Ohno, K. Nishiuchi and N. Akahira: Rapid-phase Transitions of GeTe-Sb₂Te₃ Pseudobinary Amorphous Thin Films for an Optical Disk Memory, J. Appl. Phys., 69 (5), 2849-2856, (1991).

- [11] T. Nishida, M. Terao, Y. Miyauchi and N. Akahira: Single-beam Overwrite Experiment using In-Se based Phase-change Optical Media, *Appl. Phys. Lett.* 50 (11), 667-669, (1987).
- [12] N. Miyagawa, Y. Gotoh, E. Ohno, K. Nishiuchi and N. Akahira: Land and Groove Recording for High Track Density on Phase-Change Optical Disks. *Jpn. J. Appl. Phys.* 32No. 11B, 5324-5328, (1993).
- [13] S. Morita, M. Nishyawa and T. Ueda: Super-High-Density Optical Disk Using Deep Groove Method. *Jpn. J. Appl. Phys.* 36 No. 1B, 444, (1997).
- [14] T. Kurumizawa, M. Takao, K. Kimura and K. Nagata: Extended Abstracts of the 35th Spring Meeting, 1988; The Japan Society of Apply Physics and Related Societies, No. 3, 28p-ZQ-3, 839, (1988).
- [15] T. Ohta, K. Inoue, M. Uchida, K. Yoshioka, T. Akiyama, S. Furukawa, K. Nagata and S. Nakamura: Phase Change Disk Media having Rapid Cooling Structure, *Proc. Int. Symp. on Optical Memory*, 1989, *Jpn. J. Appl. Phys.* 28 suppl. 28-3, 123-128, (1989).
- [16] T. Ohta, M. Uchida, K. Yoshioka, K. Inoue, T. Akiyama, S. Furukawa, K. Kotera and S. Nakamura: Million Cycle Overwritable Phase Change Optical Disk Media, *Proc. SPIE 1078 (Optical Data Storage Topical Meeting)*, 27-34, (1989).
- [17] T. Ohta, S. Furukawa, K. Yoshioka, M. Uchida, K. Inoue, T. Akiyama, K. Nagata and S. Nakamura: Accelerated Aging Studies for Phase Change Type Disc Media, *Proc. SPIE 1316 (Optical Data Storage)*, 367-373, (1990).
- [18] Liu Liu, Shi Zhimin, He Sailing and George J.Y. Zhong: Simulation readout signals of 3D geometrical pits/lands and surface defects, *Proceedings of SPIE*, 5643, (2005).

- [19] J.M. Li, L.P. Shi, X.S. Miao, K.G. Lim, H.X. Yang and T.C. Chong Integrated thermal and optical analyses of phase-change optical disk. *Jpn. J. Appl. Phys.* 43, 4724-4729, (2004).
- [20] D.J. Gravesteeji: Materials developments for write-once and erasable phase-change optical recording, *Appl. Opt.* 27, 736, (1988).
- [21] H. Kando, T. Maeda, M. Terao, M. Miyamoto, A. Hirotsune and H. Ohnuki: *Proc. Int. Symp.on Optical Memory*, We-H-01, (1998).
- [22] Hsin-Chang Hsiung, Optical system design in combo pick-up head, Master thesis of Chung Yuan Christian University, (2004).
- [23] Wei-Hua Li, Optical system design in red and blue laser pickup head, Master Thesis of National Central University, (2005).
- [24] ZEMAX user's Guide, Version 10.0, p165.
- [25] H.H. Hopkins: The diffraction theory of laser read-out systems for optical video discs, *J. Opt. Soc. Am.* 69, 4-25, (1979).
- [26] M. Ogawa, M. Nakada, R. Katayama, M. Okada and M. Itoh: "Analysis of scattering light from magnetic material with land/groove by three-dimensional boundary element method," *Jpn. J. Appl. Phys.* 35, 336-341, (1996).
- [27] W. C. Liu and M. W. Kowarz: "Vector diffraction from subwavelength optical disk structures: two-dimensional near-field profiles," *Optics Express* 2, 191-197, (1998).
- [28] R. W. Ziolkowski: "The incorporation of microscopic material models into the FDTD approach for ultrafast optical pulse simulations," *IEEE Trans. Atten. Prop.* 45, 375-391, (1997).

- [29] K. H. Dridi and A. Bjarklev, "Optical electromagnetic vector-field modeling for the accurate analysis of finite diffractive structures of high complexity", *Appl. Opt.* 38, 1668-1676, (1999).
- [30] Y. He, T. Kojima, T. Uno and S. adachi: "FDTD analysis of three-dimensional light-beam scattering from the magneto-optical disk structure," *IEICE Trans. Electron.* E81-C, 1881-1888, (1998).
- [31] J. L. Kann, T. D. Milster, F. F. Froehlich, R. W. Ziolkowski and J. B. Judkins: "Rigorous numerical modeling of novel optical data storage systems," *Proc. SPIE* 3109, 222-228, (1997).
- [32] K. S. Kunz and R. J. Luebbers, *The finite difference time domain method for electromagnetics*, (CRC Press, Boca Raton, Fla., 1993).
- [33] J. B. Judkins, C. W. Haggans and R. W. Ziolkowski, *Appl. Opt.* 35, 2477-2487, (1996).
- [34] L.P. Shi, T.C. Chong, J.J. Ho, Z.J. Liu, B.X. Xu, X.S. Miao, Y.M. Huang, P. K. Tan and K. G. Lim: Thermal modeling of a phase-change optical recording disk, *Optical Data Storage*, 71-78, (1998).
- [35] L.P. Shi and C.T. Chong: New Structures of the Super-Resolution Near-Field Phase-Change Optical Disk and a New Mask-Layer Material. J.Tominaga and D.P. Tsai (Eds.): *Optical Nanotechnologies*, *Topics Appl. Phys.* 88, 87-107 (2003)
- [36] Giorgio Pauletto: *Computational solution of large-scale macroeconomic models*. Kluwer Academic Publishers, (1997).
- [37] R.J. Hosking et al. *First steps in numerical analysis* 2nd ed. London: Arnold, (1996).

Publications

1. K. G. Lim, L. P. Shi, J. M. Li, X. S. Miao, W. L. Tan, H.X. Yang, Y. B. Lim, G. Q. Yuan, T. C. Chong, “An Integrated Software of Optical System and Media Design”, Digest of Optical Data Storage 2007, MC7, (ODS 2007).
2. J. M. Li, L. P. Shi, H. X. Yuan, K. G. Lim, X. S. Miao and T. C. Chong, “Local Thermal Expansion in Super Resolution Near Field Structure”, Digest of ISOM 2006, p180, (ISOM 2006).
3. J. M. Li, L. P. Shi, X. S. Miao, K. G. Lim, H. X. Yang, P. K. Tan, T. C. Chong, Near-field characteristics and signal enhancement of Super-RENS disk with metal nanoparticles. International Symposium on Optical Memory and Optical Data Storage (ISOM/ODS 2005).
4. H.X.Yang, L.P. Shi, J.M. Li, K.G. Lim, T.C. Chong. Thermal deformation analysis of bl-ray optical disks. Proc. Int. Symp. on Optical Memory 2004, 188-190, (ISOM 2004).
5. X. S. Miao, L. P. Shi, P. K. Tan, W. Xu, J.M. Li, K.G.Lim and T.C. Chong. Initialization-free Blu-ray optical disk. International Symposium on Optical Memory 2004, 104-105, (ISOM 2004).
6. J.M. Li, L. P. Shi, K. G. Lim, X. S. Miao, H.X.Yang, and T.C. Chong. Enhanced Scattering of random-distribution nanoparticles and evanescent field in a super-RENS structure, International Symposium on Optical Memory 2004, 10-15 October, (ISOM 2004).
7. J.M. Li, L. P. Shi, K. G. Lim, X. S. Miao, and T.C. Chong. Scattering of nanoparticles in super-RENS structure. Optical Data Storage 2004, pp.34, 18-21 April, (ODS 2004).

8. K. G. Lim, L. P. Shi, J. M. Li, X. S. Miao, W. L. Tan, H.X. Yang, Y. B. Lim, G. Q. Yuan, T. C. Chong, “An Integrated Software of Optical System and Media Design”, SPIE Proceedings, p6620-15, 2007.
9. X. S. Miao, L. P. Shi, P. K. Tan, J. M. Li, K. G. Lim, X. Hu and T. C. Chong. Initialization-Free Multispeed Blue Laser Optical Disc. *Jpn. J. Appl. Phys.*, Vol 45, 6337-6339, 2006.
10. J. M. Li, L. P. Shi, K. G. Lim, X. S. Miao, H. X. Yang, T. C. Chong, Enhanced scattering of random-distribution nanoparticles and evanescent field in a super-resolution nearfield structure. *Jpn. J. Appl. Phys.*, Vol 44, 3620-3622, 2005.
11. X. S. Miao, L. P. Shi, P. K. Tan, W. Xu, J. M. Li, K. G. Lim, T. C. Chong. Initialization-free blue-laser optical disc. *Jpn. J. Appl. Phys.*, Vol 44, 3612-3614, 2005.
12. J.M. Li, L.P. Shi, X.S. Miao, K.G. Lim, H.X. Yang and T.C. Chong. Integrated thermal and optical analyses of phase-change optical disk. *Jpn. J. Appl. Phys. Vol 43.*, 4724-4729, 2004.
13. X.S. Miao, L.P. Shi, P.K. Tan, J.M. Li, K.G.Lim and T.C. Chong. New Improvement Methods of Multi-speed Initialization-free Phase-change Optical Disk. *Jpn. J. Appl. Phys. Vol.43.*, 4992-4996, 2004.
14. X.S. Miao, L.P. Shi, P.K. Tan, J.M. Li, R. Zhao, K.G. Lim, X. Hu and T.C. Chong. Multi-speed rewritable optical recording method with initialization-free phase-change disk. *Journal of applied optics*, Vol.43, No.5, 1140-1146, 2004.
15. P.K. Tan, L.P. Shi, H. Meng, X.S. Miao, K.P. Wong, K.G. Lim, T.C. Chong. Substrate deformation studies direct-overwriting (DOW) of phase change

rewritable optical disc with germanium nitride interface layer. Jpn. J. Appl. Phys.
Vol.43., 5024-5028, 2004.

Appendix I

```

void COpticalInputDlg:: DisplayData()
{
    if(m_Mat.GetSize() <= m_CurMat)
    {
        m_n.Empty();
        m_k.Empty();
        m_MatName.Empty();
        m_MatCombo.SetCurSel(1);
        m_bNK = 1;
    }
    else
    {
        m_MatName = m_Mat[m_CurMat].Name;
        m_MatCombo.SetCurSel(m_Mat[m_CurMat].Mat);
        m_bNK = m_Mat[m_CurMat].bnk;

        m_n = CvtoS(m_Mat[m_CurMat].n);
        m_k = CvtoS(m_Mat[m_CurMat].k);
        m_Einf = CvtoS(m_Mat[m_CurMat].e_inf);
        m_X0 = CvtoS(m_Mat[m_CurMat].X0);
    }
    -----
    -----
    GetDlgItem(IDC_X0)->EnableWindow(m_bNK==0);
    GetDlgItem(IDC_NEXT)->EnableWindow(m_CurMat<m_NumLayer);
    GetDlgItem(IDC_PREVIOUS)->EnableWindow(m_CurMat > 0);
    UpdateData(false);
}

void COpticalInputDlg::OnDatabase()
{
    CDataBase dlg;
    dlg.m_fWl = m_fWl;
    if(dlg.DoModal()==IDOK)
    {
        m_bNK = 1;
        GetDlgItem(IDC_N)->SetWindowText("n: ");
        GetDlgItem(IDC_K)->SetWindowText("k: ");

        if(dlg.m_bMix)
        {
            CMixCalDlg MDlg;
            MDlg.m_WL = m_fWl;
            if(MDlg.DoModal()==IDOK)
            {
                -----
                -----
            }
        }
        else
        {
            if(dlg.m_iCrys && dlg.m_Type==2)
            {
                m_n.Format("%.4f", dlg.m_n_c);
                m_k.Format("%.4f", dlg.m_k_c);
            }
        }
    }
}

```

```
        }
        else
        {
            m_n.Format("%.4f", dlg.m_n);
            m_k.Format("%.4f", dlg.m_k);
        }
        m_MatName = dlg.m_MatName;
    }
    UpdateData(false);
}
}
```

Appendix II

```

void CDataBase::RetrieveNK()
{
    CString FN;
    if(m_Type==0)
        FN=".\Database\Sub\\"+m_FName;
    else if(m_Type==1)
        FN=".\Database\die\\"+m_FName;
    else if(m_Type==2)
        FN=".\Database\pc\\"+m_FName;
    else if(m_Type==3)
        FN=".\Database\Ref\\"+m_FName;
    else
        FN=".\Database\other\\"+m_FName;

    CArray<float,float>D;
    //set all the array to 0
    m_DCombo.ResetContent();
    D.SetSize(0);
    N.SetSize(0);
    K.SetSize(0);
    N_C.SetSize(0);
    K_C.SetSize(0);
    int Rno;
    float d = 0;
    float w1, n, k, n_C, k_C;
    BYTE bFirst = 0;
    FILE* f;
    f=fopen(FN, "rt");
    Rno=fscanf(f, "%f", &d);

    if(d==0)
    {
        AfxMessageBox("The file is Empty or in a Different Format !!");
    }

    if(d != -1)//new format
    {
        GetDlgItem(IDC_DCOMBO)->EnableWindow(TRUE);
        D.Add(d);
        do
        {
            Rno = fscanf(f, "%f", &d);
            if(d != -1)
                D.Add(d);

        } while (d != -1);
        int max1=D.GetSize(); //obtain the total number of thickness in the database
        int Res;
        //retrieve the N,K with respect to Wavelength
        do
        {
            Res=fscanf(f,"%f",&w1);
            //scan for the wavelength in order to show the respective n,k
            for (int i=0;i<max1;i++)
            {

```



```
        if (m_Type != 2)
        {
            Res=fscanf(f,"%f %f",&n,&k);
            if(wl == m_fWl)
            {
                bFirst = 1;
                N.Add(n);
                K.Add(k);
            }
        }
        else
        {
            Res=fscanf(f,"%f %f %f %f",&n,&k,&n_C,&k_C);
            if(wl == m_fWl)
            {
                bFirst = 1;
                N.Add(n);
                K.Add(k);
                N_C.Add(n_C);
                K_C.Add(k_C);
            }
        }
    }

    if(wl >= m_fWl) break;
}while(Res!=EOF && d!=1);
fclose(f);
//add to combobox
CString t,t1;
int ind = 0;
if(m_Type != 2)
{
    for(int i=0; i<max1; i++)
    {
        t.Format("%.1f", D.GetAt(i));
        m_DCombo.AddString(t);
    }
    //pointe to the current cursor
    //and show up the n,k value
    m_DCombo.SetCurSel(0);
    if(bFirst)
    {
        m_k=K[ind];
        m_n=N[ind];
    }
}
else//for phase change
{
    for(int i=0; i<max1; i++)
    {
        t1.Format("%.1f", D.GetAt(i));
        m_DCombo.AddString(t1);
    }
    m_DCombo.SetCurSel(0);
    if(bFirst)
    {
```

```

        m_k=K[ind];
        m_n=N[ind];
        m_k_c = K_C[ind];
        m_n_c = N_C[ind];
    }
}

//Prompt message if cannot find the n & k of input wavelength
if(bFirst==0)
{
    t.Format("Cannot Find The n and k of Wavelength %.1f", m_fWl);
    AfxMessageBox(t);
}
UpdateData(false);
}
else// read single thickness file
{
    GetDlgItem(IDC_DCOMBO)->EnableWindow(FALSE);
    do
    {
        if(m_Type != 2)
        {
            Rno=fscanf(f,"%f %f %f",&wl, &n, &k);
            if(wl == m_fWl)
            {
                bFirst = 1;
                m_k = k;
                m_n = n;
            }
        }
        else // phase change
        {
            Rno=fscanf(f, "%f %f %f %f %f", &wl, &n, &k, &n_C, &k_C);
            if(wl == m_fWl)
            {
                bFirst = 1;
                m_k=k;
                m_n=n;
                m_k_c=k_C;
                m_n_c=n_C;
            }
        }
        if(wl >= m_fWl) break;
    }while(Rno!=EOF);
} //end of read old file
fclose(f);
CString t;
if(bFirst==0)
{
    t.Format("Cannot Find The n and k of Wavelength %.1f", m_fWl);
    AfxMessageBox(t);
}
UpdateData(false);
}
}

```

Appendix III

```

void CDiskStructureDlg::ShowXZLandGroove(CDC* pDC, int bUpdate)
{
    double angle = m_GrooveAngle*PI/180;
    double swall = m_GrooveDepth /tan(angle);
    double gw = m_GrooveWidth - swall;
    double lw = m_LandWidth - swall;
    int ngd = (int)(0.5 + m_GrooveDepth/m_Delz); //groove width
    int nsw = (int)(0.5 + swall/m_Delx); //sidewall
    int ngw = (int)(0.5 + gw/m_Delx); //groove width
    int nlw = (int)(0.5 + lw/m_Delx); //landwidth

    pDC->MoveTo(m_XStart, m_YStart);
    pDC->LineTo(m_XStart+m_XSize, m_YStart);
    pDC->LineTo(m_XStart+m_XSize, m_YStart-m_YSize);
    pDC->LineTo(m_XStart, m_YStart-m_YSize);
    pDC->LineTo(m_XStart, m_YStart);

    int Nd = 0;
    int kk = 0;
    int preNd = 0;
    int Tno;

    if(m_Tno==0)
        Tno =0;
    else
    {
        if(m_Tno %2)//odd no
            Tno = -(m_Tno+1)/2;
        else
            Tno = (m_Tno/2);
    }

    for(int i=0; i<m_NumLayer; i++)
    {
        int n1;
        BYTE IsLand;
        if(m_bOnGroove==0)
        {
            n1 = nlw;
            IsLand = 0;//indication next will be 0:groove, 1:land
        }
        else
        {
            n1 = ngw;
            IsLand = 1;//indication next will be land
        }
        int nlower = (int)((m_Nx-n1)/2.0);
        int nupper = nlower + n1;
        int lower = (int)(m_XStart + nlower*(float)m_XSize/m_Nx);
        int upper = (int)(m_XStart + nupper*(float)m_XSize/m_Nx);
        preNd = Nd;
        if(i==m_Lno && bUpdate)
        {
            Nd += (int)(m_Nd*(float)m_YSize/m_Size);
        }
    }
}

```

```

else
{
    Nd += (int)(m_LayerArray[i].m_nd*(float)m_YSize/m_Size);
}
//center track
if(m_bOnGroove==0)
    kk = m_YStart-(int)(ngd*(float)m_YSize/m_Size) - Nd;
else
    kk = m_YStart - Nd;

pDC->MoveTo(lower+1, kk);
pDC->LineTo(upper, kk);
if(i==m_Lno)
{
    int klower;
    if(m_Lno==0)
        klower = m_YStart;
    else
        klower = kk+Nd-preNd;

    CRect rect(lower, klower, upper, kk);
    CBrush NewBrush;
    NewBrush.CreateSolidBrush(RGB(150, 150, 150));
    pDC->FillRect(rect, &NewBrush);
    pDC->SetBkMode(TRANSPARENT);
    if(m_LayerType && Tno==0)
        pDC->SetTextColor(RGB(255, 0, 0));
    else
        pDC->SetTextColor(RGB(255, 255, 255));
    pDC->TextOut((rect.left+rect.right)/2-2, (rect.top+rect.bottom)/2-7, "0");
}
else if(i==m_NumLayer-1 && m_Lno==m_NumLayer)
{
    CRect rect(lower, kk, upper, m_YStart-m_YSize);
    CBrush NewBrush;
    NewBrush.CreateSolidBrush(RGB(150, 150, 150));
    pDC->FillRect(rect, &NewBrush);
    pDC->SetBkMode(TRANSPARENT);
    if(m_LayerType && Tno==0)
        pDC->SetTextColor(RGB(255, 0, 0));
    else
        pDC->SetTextColor(RGB(255, 255, 255));
    pDC->TextOut((rect.left+rect.right)/2-2, (rect.top+rect.bottom)/2-7, "0");
}
//for lower region
int curstart = 0;
if(m_bOnGroove==0)
    IsLand = 0;//indication next will be 0:groove, 1:land
else
    IsLand = 1;//indication next will be land
int no = 0;
int nx = 0;
int nT = 0;
CPoint point[6];
pDC->MoveTo(lower, kk);
while(no >=0)
{
    no = nlower - curstart;
    if(IsLand)
    {

```

```

if((no-nsw)<0)
    nx = 0;
else
    nx = (no-nsw);
pDC->LineTo((int)(m_XStart +
nx*(float)m_XSize/m_Nx),m_YStart -
(int)(ngd*(float)m_YSize/m_Size) - Nd);

point[0].x = m_XStart + (int)(no*(float)m_XSize/m_Nx);
point[0].y = m_YStart - Nd;
point[5].x = m_XStart + (int)(no*(float)m_XSize/m_Nx);
point[1].x = m_XStart + (int)((nx)*(float)m_XSize/m_Nx);
point[1].y = m_YStart -(int)(ngd*(float)m_YSize/m_Size) - Nd;
point[4].x = m_XStart + (int)(nx*(float)m_XSize/m_Nx);
if(m_Lno==0)
{
    point[5].y = m_YStart; point[4].y = m_YStart;
}
else
{
    point[5].y = m_YStart -preNd;
    point[4].y = m_YStart -(int)(ngd*(float)m_YSize/m_Size)
-preNd;
}
nT++;
if((no-nsw-nlw+1)<0)
    nx = 0;
else
    nx = (no-nsw-nlw);
pDC->LineTo((int)(m_XStart +
nx*(float)m_XSize/m_Nx),m_YStart -
(int)(ngd*(float)m_YSize/m_Size) - Nd);

if(i==m_Lno && no >=0)
{
    CRgn rgn;
    point[2].x = m_XStart +
(int)((nx)*(float)m_XSize/m_Nx);
    point[2].y = m_YStart -(int)(ngd*(float)m_YSize/m_Size)
- Nd;
    point[3].x = m_XStart + (int)(nx*(float)m_XSize/m_Nx);
    if(m_Lno==0)
        point[3].y = m_YStart;
    else
        point[3].y = m_YStart -
(int)(ngd*(float)m_YSize/m_Size) -preNd;

    rgn.CreatePolygonRgn(point, 6, WINDING);
    CBrush NewBrush;
    NewBrush.CreateSolidBrush(RGB(150, 150, 150));
    pDC->FillRgn(&rgn, &NewBrush);
    pDC->SetBkMode(TRANSPARENT);
    if(m_LayerType && Tno==nT)
        pDC->SetTextColor(RGB(255, 0, 0));
    else
        pDC->SetTextColor(RGB(255, 255, 255));
    CString t;
    t.Format("-%d", nT);
    pDC->TextOut((point[1].x+point[2].x)/2-3,
(point[3].y+point[2].y)/2-7, t);
}

```

```
    }
else if(i==m_NumLayer-1 && m_Lno==m_NumLayer && no>=0)
{
    CRgn rgn;
    point[2].x = m_XStart +
(int)((nx)*(float)m_XSize/m_Nx);
    point[3].x = m_XStart + (int)(nx*(float)m_XSize/m_Nx);
    point[0].y = m_YStart - m_YSize;
    point[1].y = point[0].y;
    point[2].y = point[0].y;
    point[3].y = m_YStart -(int)(ngd*(float)m_YSize/m_Size)
-Nd;
    point[4].y = m_YStart -(int)(ngd*(float)m_YSize/m_Size)
-Nd;
    point[5].y = m_YStart -Nd;
    rgn.CreatePolygonRgn(point, 6, WINDING);
    CBrush NewBrush;
    NewBrush.CreateSolidBrush(RGB(150, 150, 150));
    pDC->FillRgn(&rgn, &NewBrush);
    if(m_LayerType && Tno==nT)
        pDC->SetTextColor(RGB(255, 0, 0));
    else
        pDC->SetTextColor(RGB(255, 255, 255));
    CString t;
    t.Format("-%d", nT);
    pDC->TextOut((point[1].x+point[2].x)/2-3,
(point[3].y+point[2].y)/2-7, t);
}
}
else
{
    if((no-nsw)<0)
        nx = 0;
    else
        nx = (no-nsw);

    pDC->LineTo((int)(m_XStart +
nx*(float)m_XSize/m_Nx),m_YStart - Nd);
    point[0].x = m_XStart + (int)(no*(float)m_XSize/m_Nx);
    point[0].y = m_YStart -(int)(ngd*(float)m_YSize/m_Size) - Nd;
    point[5].x = m_XStart + (int)(no*(float)m_XSize/m_Nx);
    point[1].x = m_XStart + (int)((nx)*(float)m_XSize/m_Nx);
    point[1].y = m_YStart - Nd;
    point[4].x = m_XStart + (int)(nx*(float)m_XSize/m_Nx);
    if(m_Lno==0)
    {
        point[5].y = m_YStart; point[4].y = m_YStart;
    }
    else
    {
        point[5].y = m_YStart -
(int)(ngd*(float)m_YSize/m_Size)-preNd;
        point[4].y = m_YStart -preNd;
    }
    nT++;
    if((no-nsw-ngw+1)<0)
        nx = 0;
    else
        nx = (no-nsw-ngw);
}
```

```

pDC->LineTo((int)(m_XStart +
nx*(float)m_XSize/m_Nx),m_YStart - Nd);

if(i==m_Lno && no >=0)
{
    CRgn rgn;
    point[2].x = m_XStart +
(int)((nx)*(float)m_XSize/m_Nx);
    point[2].y = m_YStart - Nd;
    point[3].x = m_XStart + (int)(nx*(float)m_XSize/m_Nx);
    if(m_Lno==0)
        point[3].y = m_YStart;
    else
        point[3].y = m_YStart -preNd;

    rgn.CreatePolygonRgn(point, 6, WINDING);
    CBrush NewBrush;
    NewBrush.CreateSolidBrush(RGB(150, 150, 150));
    pDC->FillRgn(&rgn, &NewBrush);
    if(m_LayerType && Tno==nT)
        pDC->SetTextColor(RGB(255, 0, 0));
    else
        pDC->SetTextColor(RGB(255, 255, 255));
    CString t;
    t.Format("-%d", nT);
    pDC->TextOut((point[1].x+point[2].x)/2-2,
(point[3].y+point[2].y)/2-7, t);
}
else if(i==m_NumLayer-1 && m_Lno==m_NumLayer && no>=0)
{
    CRgn rgn;
    point[2].x = m_XStart + int)((nx)*(float)m_XSize/m_Nx);
    point[3].x = m_XStart + (int)(nx*(float)m_XSize/m_Nx);
    point[0].y = m_YStart - m_YSize;
    point[1].y = point[0].y;
    point[2].y = point[0].y;
    point[3].y = m_YStart -Nd;
    point[4].y = m_YStart -Nd;
    point[5].y = m_YStart -
(int)(ngd*(float)m_YSize/m_Size)-Nd;
    rgn.CreatePolygonRgn(point, 6, WINDING);
    CBrush NewBrush;
    NewBrush.CreateSolidBrush(RGB(150, 150, 150));
    pDC->FillRgn(&rgn, &NewBrush);
    if(m_LayerType && Tno==nT)
        pDC->SetTextColor(RGB(255, 0, 0));
    else
        pDC->SetTextColor(RGB(255, 255, 255));
    CString t;
    t.Format("-%d", nT);
    pDC->TextOut((point[1].x+point[2].x)/2-2,
(point[3].y+point[2].y)/2-7, t);
}
}
if(IsLand)
    curstart += (nlw + nsw);
else
    curstart += (ngw + nsw );
IsLand = !IsLand;
}

```

```

//for upper region
curstart = 0;
if(m_bOnGroove==0)
    IsLand = 0;//indication next will be 0:groove, 1:land
else
    IsLand = 1;//indication next will be land
no = 0;
nx = 0;
nT = 0;
pDC->MoveTo(upper,kk);
while(no<=m_Nx)
{
    no = nupper + curstart;
    if(IsLand)
    {
        if((no+nsw)>m_Nx)
            nx = m_Nx;
        else
            nx = (no+nsw);
        pDC->LineTo((int)(m_XStart +
            nx*(float)m_XSize/m_Nx),m_YStart -
            (int)(ngd*(float)m_YSize/m_Size) - Nd);
        point[0].x = m_XStart + (int)(no*(float)m_XSize/m_Nx);
        point[0].y = m_YStart - Nd;
        point[5].x = m_XStart + (int)(no*(float)m_XSize/m_Nx);
        point[1].x = m_XStart + (int)((nx)*(float)m_XSize/m_Nx);
        point[1].y = m_YStart -(int)(ngd*(float)m_YSize/m_Size) - Nd;
        point[4].x = m_XStart + (int)(nx*(float)m_XSize/m_Nx);
        if(m_Lno==0)
        {
            point[5].y = m_YStart; point[4].y = m_YStart;
        }
        else
        {
            point[5].y = m_YStart -preNd;
            point[4].y = m_YStart -(int)(ngd*(float)m_YSize/m_Size)
            -preNd;
        }
        nT++;
        if((no+nsw+nlw+1)>m_Nx)
            nx = m_Nx;
        else
            nx = (no+nsw+nlw);
        pDC->LineTo((int)(m_XStart +
            nx*(float)m_XSize/m_Nx),m_YStart -
            (int)(ngd*(float)m_YSize/m_Size) - Nd);

        if(i==m_Lno && no <=m_Nx)
        {
            CRgn rgn;
            point[2].x = m_XStart +
            (int)((nx)*(float)m_XSize/m_Nx);
            point[2].y = m_YStart -(int)(ngd*(float)m_YSize/m_Size)
            - Nd;
            point[3].x = m_XStart + (int)(nx*(float)m_XSize/m_Nx);
            if(m_Lno==0)
                point[3].y = m_YStart;
            else

```



```

        point[3].y = m_YStart -
        (int)(ngd*(float)m_YSize/m_Size) -preNd;

        rgn.CreatePolygonRgn(point, 6, WINDING);
        CBrush NewBrush;
        NewBrush.CreateSolidBrush(RGB(150, 150, 150));
        pDC->FillRgn(&rgn, &NewBrush);
        if(m_LayerType && Tno==nT)
            pDC->SetTextColor(RGB(255, 0, 0));
        else
            pDC->SetTextColor(RGB(255, 255, 255));
        CString t;
        t.Format("%d", nT);
        pDC->TextOut((point[1].x+point[2].x)/2-2,
        (point[3].y+point[2].y)/2-7, t);
    }

    else if(i==m_NumLayer-1 && m_Lno==m_NumLayer
    && no<=m_Nx)
    {
        CRgn rgn;
        point[2].x = m_XStart +
        (int)((nx)*(float)m_XSize/m_Nx);
        point[3].x = m_XStart + (int)(nx*(float)m_XSize/m_Nx);
        point[0].y = m_YStart - m_YSize;
        point[1].y = point[0].y;
        point[2].y = point[0].y;
        point[3].y = m_YStart -(int)(ngd*(float)m_YSize/m_Size)
        -Nd;
        point[4].y = m_YStart -(int)(ngd*(float)m_YSize/m_Size)
        -Nd;
        point[5].y = m_YStart -Nd;
        rgn.CreatePolygonRgn(point, 6, WINDING);
        CBrush NewBrush;
        NewBrush.CreateSolidBrush(RGB(150, 150, 150));
        pDC->FillRgn(&rgn, &NewBrush);
        if(m_LayerType && Tno==nT)
            pDC->SetTextColor(RGB(255, 0, 0));
        else
            pDC->SetTextColor(RGB(255, 255, 255));
        CString t;
        t.Format("%d", nT);
        pDC->TextOut((point[1].x+point[2].x)/2-2,
        (point[3].y+point[2].y)/2-7, t);
    }
}
else
{
    if((no+nsw)>m_Nx)
        nx = m_Nx;
    else
        nx = (no+nsw);
    pDC->LineTo((int)(m_XStart +
    nx*(float)m_XSize/m_Nx),m_YStart - Nd);

    point[0].x = m_XStart + (int)(no*(float)m_XSize/m_Nx);
    point[0].y = m_YStart -(int)(ngd*(float)m_YSize/m_Size) - Nd;
    point[5].x = m_XStart + (int)(no*(float)m_XSize/m_Nx);
    point[1].x = m_XStart + (int)((nx)*(float)m_XSize/m_Nx);
    point[1].y = m_YStart - Nd;
    point[4].x = m_XStart + (int)(nx*(float)m_XSize/m_Nx);

```

```

if(m_Lno==0)
{
    point[5].y = m_YStart; point[4].y = m_YStart;
}
else
{
    point[5].y = m_YStart -
(int)(ngd*(float)m_YSize/m_Size)-preNd;
    point[4].y = m_YStart -preNd;
}
nT++;
if((no+nsw+ngw+1)>m_Nx)
    nx = m_Nx;
else
    nx = (no+nsw+ngw);
pDC->LineTo((int)(m_XStart +
nx*(float)m_XSize/m_Nx),m_YStart - Nd);
if(i==m_Lno && no <=m_Nx)
{
    CRgn rgn;
    point[2].x = m_XStart +
(int)((nx)*(float)m_XSize/m_Nx);
    point[2].y = m_YStart - Nd;
    point[3].x = m_XStart + (int)(nx*(float)m_XSize/m_Nx);
    if(m_Lno==0)
        point[3].y = m_YStart;
    else
        point[3].y = m_YStart -preNd;

    rgn.CreatePolygonRgn(point, 6, WINDING);
    CBrush NewBrush;
    NewBrush.CreateSolidBrush(RGB(150, 150, 150));
    pDC->FillRgn(&rgn, &NewBrush);
    if(m_LayerType && Tno==nT)
        pDC->SetTextColor(RGB(255, 0, 0));
    else
        pDC->SetTextColor(RGB(255, 255, 255));
    CString t;
    t.Format("%d", nT);
    pDC->TextOut((point[1].x+point[2].x)/2-2,
(point[3].y+point[2].y)/2-7, t);
}
else if(i==m_NumLayer-1 && m_Lno==m_NumLayer &&
no<=m_Nx)
{
    CRgn rgn;
    point[2].x = m_XStart +
(int)((nx)*(float)m_XSize/m_Nx);
    point[3].x = m_XStart + (int)(nx*(float)m_XSize/m_Nx);
    point[0].y = m_YStart - m_YSize;
    point[1].y = point[0].y;
    point[2].y = point[0].y;
    point[3].y = m_YStart -Nd;
    point[4].y = m_YStart -Nd;
    point[5].y = m_YStart -
(int)(ngd*(float)m_YSize/m_Size)-Nd;
    rgn.CreatePolygonRgn(point, 6, WINDING);
    CBrush NewBrush;
    NewBrush.CreateSolidBrush(RGB(150, 150, 150));
    pDC->FillRgn(&rgn, &NewBrush);
}

```

```
        if(m_LayerType && Tno==nT)
            pDC->SetTextColor(RGB(255, 0, 0));
        else
            pDC->SetTextColor(RGB(255, 255, 255));
        CString t;
        t.Format("%d", nT);
        pDC->TextOut((point[1].x+point[2].x)/2-2,
                    (point[3].y+point[2].y)/2-7, t);
    }
}

if(IsLand)
    curstart += (nlw + nsw);
else
    curstart += (ngw + nsw );
IsLand = !IsLand;
}
}
}
```

Appendix IV

```

void CImportZemaxFileDialog::ReadBeamFile(CString fn, BYTE bSec)
{
    FILE* f= fopen(fn, "rt");
    int res = 0, er=0;
    int no = 1, sno, nnx, nny;
    char d[50000];
    char t1[200];
    float x,y;
    CString t;
    //read first row data, to find out n_x
    do{
        res = fscanf(f, "%[^\n]\n", d);
        if(no==5)
        {
            t = d;
            t.MakeLower();
            int no = t.Find("total");
            if(bSec==0)
            {
                if(no != -1)
                {
                    m_bField = 1;
                    m_Field = 0;
                    GetDlgItem(IDC_BROWSE2)->EnableWindow(false);
                    AfxMessageBox("The electric field of the imported file is
                    total field, by default set as Ex field.");
                }
                else
                {
                    no = t.Find("ex");
                    if(no != -1)
                    {
                        m_bField = 1;
                        m_Field = 0;
                        GetDlgItem(IDC_S1)->SetWindowText("Select
                        the beam file of the second field : Ey");
                        GetDlgItem(IDC_BROWSE2)-
                        >EnableWindow(true);
                        AfxMessageBox("The electric field of the
                        imported file is Ex field, please import Ey field.");
                    }
                    else
                    {
                        no = t.Find("ey");
                        if(no != -1)
                        {
                            m_bField = 2;
                            m_Field = 1;
                            GetDlgItem(IDC_S1)-
                            >SetWindowText("Select the beam file
                            of the second field : Ex");
                            GetDlgItem(IDC_BROWSE2)-
                            >EnableWindow(true);
                        }
                    }
                }
            }
        }
    } while(res != -1);
}

```

```

        AfxMessageBox("The electric field of
        the imported file is Ey field, please
        import Ex field.");
    }
}
}
if(no == -1)
{
    AfxMessageBox("Invalid beam file!");
    fclose(f);
    return ;
}
}
else
{
    if(m_bField == 1)
    {
        no = t.Find("ey");
        if(no == -1)
        {
            m_FN2.Empty();
            m_bField = 1;
            AfxMessageBox("The imported file was not Ex
            field file, please reimport again.");
            UpdateData(false);
            fclose(f);
            return;
        }
        else
        {
            m_bField = 11;
        }
    }
    else if (m_bField == 2)
    {
        no = t.Find("ex");
        if(no == -1)
        {
            m_FN2.Empty();
            m_bField = 2;
            AfxMessageBox("The imported file was not Ey
            field file, please reimport again.");
            UpdateData(false);
            fclose(f);
            return;
        }
        else
        {
            m_bField = 12;
        }
    }
}
UpdateData(false);
}
if(no==6)
{
```

```

t = d;
sno = t.Find(":");
t = t.Mid(sno+1);
er = sscanf(t, "%d %s %d", &nny, &t1, &nnx);
if(er==0)
{
    AfxMessageBox("Invalid Zemax Beam File");
    fclose(f);
    return;
}

if(bSec==0)
{
    m_nnx = nnx; m_nny = nny;
}
else
{
    if(m_nnx != nnx || m_nny != nny)
    {
        AfxMessageBox("The Grid size x or y of the selected
        beam file of second field didn't match with first beam
        file!\n Please reselect the file.");
        m_FN2.Empty();
        if(m_bField == 11) m_bField = 1;
        else if(m_bField == 12) m_bField = 2;
        UpdateData(false);
        fclose(f);
        return;
    }
}
}

if(no==7)
{
    t = d;
    sno = t.Find(":");
    t = t.Mid(sno+1);
    er = sscanf(t, "%e %s %e", &y, &t1, &x);
    if(er==0)
    {
        AfxMessageBox("Invalid Zemax Beam File");
        fclose(f);
        return;
    }

    if(bSec==0)
    {
        m_ZDx = (float)(x*1E3); m_ZDy = (float)(y*1E3);
    }
    else
    {
        x *= 1E3; y *= 1E3;
        if(m_ZDx != x || m_ZDy != y)
        {
            AfxMessageBox("The Delta x or Delta y of the selected
            beam file of second field didn't match with first beam
            file!\n Please reselect the file.");
            m_FN2.Empty();
            if(m_bField == 11) m_bField = 1;
            else if(m_bField == 12) m_bField = 2;
        }
    }
}

```

```

        UpdateData(false);
        fclose(f);
        return;
    }
}

}

if(no==9)
{
    t = d;
    sno = t.Find("=");
    t = t.Mid(sno+1);
    sscanf(t, "%e ", &y);
    sno = t.Find("=");
    t = t.Mid(sno+1);
    er = sscanf(t, "%e ", &x);
    if(er==0)
    {
        AfxMessageBox("Invalid Zemax Beam File");
        fclose(f);
        return;
    }

    if(bSec==0)
    {
        m_Zx = (float)(x*1E3); m_Zy = (float)(y*1E3);
    }
    else
    {
        x *= 1E3; y *= 1E3;
        if(m_Zx != x || m_Zx != y)
        {
            AfxMessageBox("The sample size x or y of the selected
            beam file of second field didn't match with first beam
            file!\n Please reselect the file.");
            m_FN2.Empty();
            if(m_bField == 11) m_bField = 1;
            else if(m_bField == 12) m_bField = 2;
            UpdateData(false);
            fclose(f);
            return;
        }
    }
    UpdateData(false);
    fclose(f);
    return;
}
no ++;
if(res ==0)
{
    AfxMessageBox("Invalid Zemax Beam File");
    fclose(f);
    return;
}

}while(res != EOF);

if(no < 9)
{

```

```
        if(bSec==0) m_FN.Empty();
        else
        {
            m_FN2.Empty();
            if(m_bField == 11) m_bField = 1;
            else if(m_bField == 12) m_bField = 2;
        }
        UpdateData(false);
        AfxMessageBox("Invalid Zemax Beam File");
        fclose(f);
        return;
    }
    fclose(f);
}
```


Appendix V

```
void CFDTDView::OnDraw(CDC* pDC)
{
    GetClientRect(&m_oldRect);
    m_oldRect.top = 0;
    m_oldRect.left = 0;
    InitGL(GetDC());
    DrawScene();

    HGLRC hrc;
    hrc = wglGetCurrentContext();
    if(hrc !=NULL)
    {
        wglMakeCurrent(NULL, NULL);
        wglDeleteContext(hrc);
        hrc =NULL;
    }
}
```

Appendix VI

```
void CRFView::OnDraw(CDC* pDC)
{
    CFDTDDoc* pDoc = (CFDTDDoc*)GetDocument();
    CRect PlotArea;
    CRect InfoArea;

    if(pDoc->m_RFData.GetSize()==0)
        return;

    if(pDC->IsPrinting())
    {
        // get size of printer page (in pixels)
        int cxPage = pDC->GetDeviceCaps(HORZRES);
        int cyPage = pDC->GetDeviceCaps(VERTRES);

        if(cxPage >= cyPage)
            m_nPrintScale = cxPage/756;
        else
            m_nPrintScale = cyPage / 630;
    }
    else
        m_nPrintScale = 1;

    PrepareRect(pDC, &PlotArea, &InfoArea);
    DrawRFSignal(PlotArea, pDC, pDoc->m_StartPoint*pDoc->m_Dely,
        (pDoc->m_StartPoint+(pDoc->m_TotalPoint-1)*pDoc->m_SimStep)*pDoc-
        >m_Dely, pDoc->m_RFData);
    if(m_bDrawBullet)
        DrawBulletText(pDC);
}
```

Appendix VII

```

void ThermalDlg::OnPaint()
{
    CPaintDC dc(this); // device context for painting
    if(LInd==0)
    {
        GetDlgItem(IDC_THE_WAVELENGTH)->EnableWindow(TRUE);
        GetDlgItem(IDC_THE_WAVELENGTH_EDIT)->EnableWindow(TRUE);
        GetDlgItem(IDC_THE_DIRECTION)->EnableWindow(TRUE);
        GetDlgItem(IDC_THE_DIRECTION_TOPRADIO)->EnableWindow(TRUE);
        GetDlgItem(IDC_THE_DIRECTION_SUBRADIO)->EnableWindow(TRUE);
        GetDlgItem(IDC_THE_NUMLAYERS)->EnableWindow(TRUE);
        GetDlgItem(IDC_THE_NUMLAYERS_EDIT)->EnableWindow(TRUE);
        GetDlgItem(IDC_GR)->EnableWindow(TRUE);
        GetDlgItem(IDC_GR_TEXT)->EnableWindow(TRUE);
        GetDlgItem(IDC_ABSORPTION_CHECK)->EnableWindow(FALSE);
    }
    else
    {
        GetDlgItem(IDC_THE_WAVELENGTH)->EnableWindow(FALSE);
        GetDlgItem(IDC_THE_WAVELENGTH_EDIT)->EnableWindow(FALSE);
        GetDlgItem(IDC_THE_DIRECTION)->EnableWindow(FALSE);
        GetDlgItem(IDC_THE_DIRECTION_TOPRADIO)->EnableWindow(FALSE);
        GetDlgItem(IDC_THE_DIRECTION_SUBRADIO)->EnableWindow(FALSE);
        GetDlgItem(IDC_THE_NUMLAYERS)->EnableWindow(FALSE);
        GetDlgItem(IDC_THE_NUMLAYERS_EDIT)->EnableWindow(FALSE);
        GetDlgItem(IDC_GR)->EnableWindow(FALSE);
        GetDlgItem(IDC_GR_TEXT)->EnableWindow(FALSE);
        GetDlgItem(IDC_ABSORPTION_CHECK)->EnableWindow(!m_the_pc_check);
    }
    //Disable pc layer check and Previous button on beginning
    if(LInd==0)
    {
        GetDlgItem(IDC_THE_PC_CHECK)->ShowWindow(SW_HIDE);
        GetDlgItem(IDC_THE_PREVIOUS_BUTTON)->EnableWindow(FALSE);
        m_the_layerthick.SetWindowText("Thickness(nm) :");
    }
    else
    {
        GetDlgItem(IDC_THE_PC_CHECK)->ShowWindow(SW_SHOW);
        GetDlgItem(IDC_THE_PREVIOUS_BUTTON)->EnableWindow(TRUE);
        m_the_layerthick.SetWindowText("Thickness(nm) :");
    }
    //Disable Next Button at last layer activate finish button
    if(LInd == m_the_numlayers)
    {
        GetDlgItem(IDC_THE_NEXT_BUTTON)->EnableWindow(FALSE);
        GetDlgItem(IDC_THE_FINISH_BUTTON)->EnableWindow(TRUE);
    }
    else
    {
        GetDlgItem(IDC_THE_NEXT_BUTTON)->EnableWindow(TRUE);
        GetDlgItem(IDC_THE_FINISH_BUTTON)->EnableWindow(FALSE);
    }

    // Change the name of the group box.

```

```

switch(LInd)
{
    case 0:
        m_the_layername.SetWindowText("Substrate :");
        break;
    case 1:
        m_the_layername.SetWindowText("1st Layer :");
        break;
    case 2:
        m_the_layername.SetWindowText("2nd Layer :");
        break;
    case 3:
        m_the_layername.SetWindowText("3rd Layer :");
        break;
    default:
        char* buffer=new char[15];
        sprintf(buffer, "%dth Layer :", LInd);
        m_the_layername.SetWindowText(buffer);
        delete buffer;
        break;
}
// check for phase change layer, then show new set.
if(!m_the_pc_check) //not phase change layer
{
    GetDlgItem(IDC_THE_TT_STATIC)->ShowWindow(SW_HIDE);
    GetDlgItem(IDC_THE_TT_EDIT)->ShowWindow(SW_HIDE);
    GetDlgItem(IDC_THE_MP)->ShowWindow(SW_HIDE);
    GetDlgItem(IDC_THE_MP_EDIT)->ShowWindow(SW_HIDE);

    GetDlgItem(IDC_THE_REFRACT_CEDIT)->ShowWindow(SW_HIDE);
    GetDlgItem(IDC_THE_AMORPHOUS)->ShowWindow(SW_HIDE);
    GetDlgItem(IDC_THE_CRYSTALLINE)->ShowWindow(SW_HIDE);
    GetDlgItem(IDC_THE_DENSITY_CEDIT)->ShowWindow(SW_HIDE);
    GetDlgItem(IDC_THE_SHC_CEDIT)->ShowWindow(SW_HIDE);
    GetDlgItem(IDC_THE_HC_CEDIT)->ShowWindow(SW_HIDE);
    GetDlgItem(IDC_THE_HC_CEDIT3)->ShowWindow(SW_HIDE);
    GetDlgItem(IDC_THE_HC_CEDIT2)->ShowWindow(SW_HIDE);
    GetDlgItem(IDC_THE_EC_CEDIT)->ShowWindow(SW_HIDE);
    // DISABLE for precaution
    //GetDlgItem(IDC_THE_LH)->EnableWindow(FALSE);
    GetDlgItem(IDC_THE_TT_EDIT)->EnableWindow(FALSE);
    //GetDlgItem(IDC_THE_MP)->EnableWindow(FALSE);
    GetDlgItem(IDC_THE_MP_EDIT)->EnableWindow(FALSE);
    GetDlgItem(IDC_THE_REFRACT_CEDIT)->EnableWindow(FALSE);
    //GetDlgItem(IDC_THE_AMORPHOUS)->EnableWindow(FALSE);
    //GetDlgItem(IDC_THE_CRYSTALLINE)->EnableWindow(FALSE);
    GetDlgItem(IDC_THE_DENSITY_CEDIT)->EnableWindow(FALSE);
    GetDlgItem(IDC_THE_SHC_CEDIT)->EnableWindow(FALSE);
    GetDlgItem(IDC_THE_HC_CEDIT)->EnableWindow(FALSE);
    GetDlgItem(IDC_THE_EC_CEDIT)->EnableWindow(FALSE);
}
else
{
    GetDlgItem(IDC_THE_TT_EDIT)->ShowWindow(SW_SHOW);
    GetDlgItem(IDC_THE_TT_STATIC)->ShowWindow(SW_SHOW);
    GetDlgItem(IDC_THE_MP)->ShowWindow(SW_SHOW);
    GetDlgItem(IDC_THE_MP_EDIT)->ShowWindow(SW_SHOW);

    GetDlgItem(IDC_THE_AMORPHOUS)->ShowWindow(SW_SHOW);
    GetDlgItem(IDC_THE_CRYSTALLINE)->ShowWindow(SW_SHOW);
}

```

```
GetDlgItem(IDC_THE_DENSITY_CEDIT)->ShowWindow(SW_SHOW);
GetDlgItem(IDC_THE_SHC_CEDIT)->ShowWindow(SW_SHOW);
GetDlgItem(IDC_THE_HC_CEDIT)->ShowWindow(SW_SHOW);
GetDlgItem(IDC_THE_HC_CEDIT3)->ShowWindow(SW_SHOW);
GetDlgItem(IDC_THE_HC_CEDIT2)->ShowWindow(SW_SHOW);
GetDlgItem(IDC_THE_EC_CEDIT)->ShowWindow(SW_SHOW);
GetDlgItem(IDC_THE_REFRACT_CEDIT)->ShowWindow(SW_SHOW);
// DISABLE for precaution
//GetDlgItem(IDC_THE_LH)->EnableWindow(TRUE);
GetDlgItem(IDC_THE_TT_EDIT)->EnableWindow(TRUE);

//GetDlgItem(IDC_THE_MP)->EnableWindow(TRUE);
GetDlgItem(IDC_THE_MP_EDIT)->EnableWindow(TRUE);

//GetDlgItem(IDC_THE_AMORPHOUS)->EnableWindow(TRUE);
//GetDlgItem(IDC_THE_CRYSTALLINE)->EnableWindow(TRUE);
GetDlgItem(IDC_THE_DENSITY_CEDIT)->EnableWindow(TRUE);
GetDlgItem(IDC_THE_SHC_CEDIT)->EnableWindow(TRUE);
GetDlgItem(IDC_THE_HC_CEDIT)->EnableWindow(TRUE);
GetDlgItem(IDC_THE_EC_CEDIT)->EnableWindow(TRUE);
GetDlgItem(IDC_THE_REFRACT_CEDIT)->EnableWindow(TRUE);
}
GetDlgItem(IDC_RX)->EnableWindow(m_IsEllipse);
GetDlgItem(IDC_RY)->EnableWindow(m_IsEllipse);
}
```

Appendix VIII

```

void DatabaseDlg::OnSelchangeNamelist()
{
    GetDlgItem(IDOK)->EnableWindow(FALSE);
    UpdateData();
    m_NameList1.ResetContent();
    int ind = m_NameList.GetCurSel();
    CString name;
    m_NameList.GetText(ind, name);
    int Rn = ft.Find("*.odb");
    CString FileName;
    FileName = ft.Left(Rn) + name + ".tdb";
    CString DataName;
    CString rString;
    CFile f;
    mat.SetSize(0);

    // Add items into the Data list box
    mat.SetSize(0);
    if(!f.Open(FileName, CFile::modeRead))
    {
        AfxMessageBox("Only optical parameter will be import!");
        GetDlgItem(IDOK)->EnableWindow(TRUE);
    }
    else
    {
        CArchive ar(&f, CArchive::load);
        data pmat; // pointer to material
        char t;
        BYTE bRs;
        int rno;
        do
        {
            bRs = ar.ReadString(rString);
            rno = rString.Find(";");
            DataName = rString.Left(rno);
            if(bRs)
            {
                m_NameList1.AddString(DataName);
                DataName = rString.Mid(rno);
                if(!bpc)
                    sscanf(DataName,"%c %f %f %f", &t, &pmat.cd,
                        &pmat.sp, &pmat.ds);
                else
                    sscanf(DataName,"%c %f %f %f %f %f %f", &t,
                        &pmat.cd, &pmat.sp, &pmat.ds, &pmat.mp, &pmat.tt);
                mat.Add(pmat);
            }
        } while(bRs && (rno !=-1));
        ar.Close();
        f.Close(); // end of addlist to namelist1
    }
    fn = ft.Left(Rn) + name + ".odb";
    if(!bpc)
    {
        // NON-PHASE CHANGE LAYER
        GetDlgItem(IDC_RELATIONSHIP)->ShowWindow(SW_SHOW);
    }
}

```

```
        GetDlgItem(IDC_N3)->ShowWindow(SW_SHOW);
        GetDlgItem(IDC_N3_AMP)->ShowWindow(SW_SHOW);
        GetDlgItem(IDC_K3)->ShowWindow(SW_SHOW);
        GetDlgItem(IDC_K3_AMP)->ShowWindow(SW_SHOW);
    }
    else
    {
        // PHASE CHANGE LAYER
        GetDlgItem(IDC_RELATIONSHIP)->ShowWindow(SW_SHOW);
        GetDlgItem(IDC_N3)->ShowWindow(SW_SHOW);
        GetDlgItem(IDC_N3_AMP)->ShowWindow(SW_SHOW);
        GetDlgItem(IDC_K3)->ShowWindow(SW_SHOW);
        GetDlgItem(IDC_K3_AMP)->ShowWindow(SW_SHOW);
        GetDlgItem(IDC_AMORPHOUS)->ShowWindow(SW_SHOW);
        GetDlgItem(IDC_CRYSTALLINE)->ShowWindow(SW_SHOW);
        GetDlgItem(IDC_K3_CRY)->ShowWindow(SW_SHOW);
        GetDlgItem(IDC_N3_CRY)->ShowWindow(SW_SHOW);
        GetDlgItem(IDC_MIX)->EnableWindow(bpc);
    }
    m_Dcombo.ResetContent();
    RetrieveNK();
}
```

Appendix IX

```

void CGMESHSETTING::UpdateNE()
{
    int trackno = m_pDoc->iNoOfTrack;
    if(m_pDoc->fGrooveAngle)
    {
        double Angle = 3.14159265359 * m_pDoc->fGrooveAngle / 180.0;
        int n_s = (int)((pNz[0] * m_pDoc->fGrooveDepth*1e3) / (m_pDoc->Layer[0].d *
        cos(Angle)));
        for(unsigned i = 1; i <=uiNumberOfLayer; i++)
            n_s += (int)( pNz[i] * m_pDoc->fGrooveDepth*1e3)/(m_pDoc-
            >Layer[i].d* cos(Angle));

        n_s /= (uiNumberOfLayer + 1);
        if(!n_s) n_s = 1;

        int ny = 0;
        if(m_pDoc->iRecordOnGroove)
            ny = (trackno-1)* (m_nyl + n_s) + m_nyg ;
        else
            ny = (trackno-1) * (m_nyg + n_s) + m_nyl;

        m_node = (m_nx+1)*(ny+1)*(pNz[0]+1);
        m_Element = m_nx*ny*pNz[0];
        for(i=1; i<=uiNumberOfLayer; i++)
        {
            m_node += (m_nx+1)*(ny+1)*(pNz[i]);
            m_Element += m_nx*ny*pNz[i];
        }
    }
    else
    {
    }
    UpdateData(false);
}

```


Appendix X

```

void ThermalSimDlg::DrawPulseList()
{
    //display pulse shape
    CDC *pDC = new CClientDC(this);
    CBrush NewBrush;
    CPen NewPen;
    NewBrush.CreateSolidBrush(RGB(1, 1, 1));
    NewPen.CreatePen(PS_SOLID, 1, RGB(255, 255, 0));
    pDC->FillRect(m_rPulseZone, &NewBrush);
    m_rPulseZone.InflateRect(0, -10);
    CPen* OldPen = pDC->SelectObject(&NewPen);
    int iX = m_rPulseZone.left;
    int iY = m_rPulseZone.bottom;

    if(bDisplay==1)
    {
        if(m_iCurno) m_PS = "Pulse Shape: " + m_SimSymbol;
        int iPulseWidth = 0;
        double dPulseHeight = 0.0;
        for (int i = 0; i < pBasicList[m_iCurno - 1].GetSize(); i++)
        {
            iPulseWidth += pBasicList[m_iCurno - 1][i].iTime;
            dPulseHeight = (pBasicList[m_iCurno - 1][i].dPower >
                dPulseHeight)?pBasicList[m_iCurno - 1][i].dPower:dPulseHeight;
        }

        iY = m_rPulseZone.bottom - (int)(0.4 * m_rPulseZone.Height());
        pDC->MoveTo(iX, iY);
        iX += m_rPulseZone.Width() * 5 / 100;
        pDC->LineTo(iX, iY);

        for (i = 0; i < pBasicList[m_iCurno - 1].GetSize(); i++)
        {
            iY = m_rPulseZone.bottom - (int)((pBasicList[m_iCurno - 1][i].dPower /
                dPulseHeight) * m_rPulseZone.Height());
            pDC->LineTo(iX, iY);
            iX += (int)(((double)pBasicList[m_iCurno - 1][i].iTime /
                (double)iPulseWidth) * m_rPulseZone.Width() * 90 / 100);
            pDC->LineTo(iX, iY);
        }

        iY = m_rPulseZone.bottom - (int)(0.4 * m_rPulseZone.Height());
        pDC->LineTo(iX, iY);
        iX += m_rPulseZone.Width() * 5 / 100;
        pDC->LineTo(iX, iY);
    }
    //end of display = 1
    else if(bDisplay==2)
    {
        UnCombineLoad(m_PulseLoads);
        m_PS = "Pulse Shape: " + m_PulseLoads;
        int d = 1;
        int listno;
        char Symbol;
        int iPulseWidth = 0;
        double dPulseHeight = 0.0;
        CString C,S;
    }
}

```

```
iX = m_rPulseZone.left;
iY = m_rPulseZone.bottom;

for(int k=0; k < Loads.GetSize(); k++)
{
    int res = sscanf(Loads[k], "%d %c", &d, &Symbol);
    if(!res)
    {
        d = 1;
        sscanf(Loads[k], "%c", &Symbol);
    }

    for(int j=1; j <= d; j++)
    {
        for(int charno = 0; charno < m_iTotalBasicPulse; charno++)
        {
            C = cPulseListName[charno];
            S = Symbol;
            C.MakeUpper();
            S.MakeUpper();
            if(C == S)
            {
                listno = charno;
                break;
            }
        }
        for (int i = 0; i < pBasicList[listno].GetSize(); i ++ )
        {
            iPulseWidth += pBasicList[listno][i].iTime;
            dPulseHeight = (pBasicList[listno][i].dPower >
                dPulseHeight)?pBasicList[listno][i].dPower:dPulseHeight;
        }
    }
}

iY = m_rPulseZone.bottom - (int)(0.4 * m_rPulseZone.Height());
pDC->MoveTo(iX, iY);
iX += m_rPulseZone.Width() * 5 / 100;
pDC->LineTo(iX, iY);
for( k=0; k < Loads.GetSize(); k++)
{
    int res = sscanf(Loads[k], "%d %c", &d, &Symbol);
    if(!res)
    {
        d = 1;
        sscanf(Loads[k], "%c", &Symbol);
    }

    for(int j=1; j <= d; j++)
    {
        for(int charno = 0; charno < m_iTotalBasicPulse; charno++)
        {
            C = cPulseListName[charno];
            S = Symbol;
            C.MakeUpper();
            S.MakeUpper();
            if(C == S)
            {
                listno = charno;
                break;
            }
        }
    }
}
```

```
        }
    }

    for (int i = 0; i < pBasicList[listno].GetSize(); i++)
    {
        iY = m_rPulseZone.bottom -
            (int)((pBasicList[listno][i].dPower / dPulseHeight) *
                m_rPulseZone.Height());
        pDC->LineTo(iX, iY);
        iX += (int)(((double)pBasicList[listno][i].iTime /
            (double)iPulseWidth) * m_rPulseZone.Width() * 90 / 100);
        pDC->LineTo(iX, iY);
    }
}

iY = m_rPulseZone.bottom - (int)(0.4 * m_rPulseZone.Height());
pDC->LineTo(iX, iY);
iX += m_rPulseZone.Width() * 5 / 100;
pDC->LineTo(iX, iY);
} //end of display =2
m_rPulseZone.InflateRect(0, 10);
pDC->SelectObject(OldPen);
DeleteObject(NewPen);
delete pDC;
UpdateData(false);
//End Of display
}
```

Appendix XI

```

void CFEADODView::OnDraw(CDC* pDC)
{
    CFEADODoc* pDoc = GetDocument();
    ASSERT_VALID(pDoc);
    if(!pDoc->Temperature[0].GetSize())
        pDoc->bpre = 1;
    bpre = pDoc->bpre;

    if(pDoc->uiReadFile)
    {
        //max &min Point
        for(int i=0; i<pDoc->ElementArray.GetSize(); i++)
        {
            if((pDoc->ElementArray[i].material <4) || pDoc->ElementArray[i].material
                == 5)
            {
                MinBPoint = MaxBPoint = pDoc->nodeArray[pDoc-
                    >ElementArray[i].nodeNo[0] -1];
                break;
            }
        }
        for( i=0; i<pDoc->ElementArray.GetSize(); i++)
        {
            for(int j=0; j <8; j++)
            {
                Min(MinBPoint, pDoc->nodeArray[pDoc-
                    >ElementArray[i].nodeNo[j] -1]);
                Max(MaxBPoint, pDoc->nodeArray[pDoc-
                    >ElementArray[i].nodeNo[j] -1]);
            }
        }

        float Temp_MAX, Temp_MIN;
        if(!pDoc->bpre)
        {
            if(!pDoc->btReWrite)
            {
                Temp_MAX = pDoc->Temperature[CurTime][0];
                Temp_MIN = pDoc->Temperature[CurTime][0];
                //find out minimum and maximum pDoc->Temperature
                if(!bMarkShape)
                {
                    for(int j = 0; j <pDoc->Temperature[CurTime].GetSize();
                        j++)
                    {
                        if (pDoc->Temperature[CurTime][j] >
                            Temp_MAX)
                            Temp_MAX = pDoc->Temperature[CurTime][j];
                        if (pDoc->Temperature[CurTime][j] <
                            Temp_MIN)
                            Temp_MIN = pDoc->Temperature[CurTime][j];
                    }
                }
            }
            else
            {

```

```

        for(int i = 0; i <pDoc->TimeStep.GetSize(); i++)
        {
            for(int j = 0; j <pDoc->Temperature[CurTime].GetSize(); j++)
            {
                if (pDoc->Temperature[i][j] >
                    Temp_MAX)
                    Temp_MAX = pDoc->Temperature[i][j];
            }
            Temp_MIN = fMeltingPoint;
        }
    }
else
{
    bMarkShape = 0;
    //find out minimum and maximum pDoc->Temperature
    Temp_MAX = pDoc->Temperature1[CurTime][0];
    Temp_MIN = pDoc->Temperature1[CurTime][0];
    for(int j = 0; j <pDoc->Temperature1[CurTime].GetSize(); j++)
    {
        if (pDoc->Temperature1[CurTime][j] > Temp_MAX)
            Temp_MAX = pDoc->Temperature1[CurTime][j];
        if (pDoc->Temperature1[CurTime][j] < Temp_MIN)
            Temp_MIN = pDoc->Temperature1[CurTime][j];
    }
}

if (pDC->IsPrinting())
{
}
else
{
    Init(pDC);
    DrawScene(pDoc, Temp_MAX, Temp_MIN);
    //delete RC for opengl
    HGLRC hrc;
    hrc = wglGetCurrentContext();
    if(hrc !=NULL)
    {
        wglMakeCurrent(NULL, NULL);
        wglDeleteContext(hrc);
        hrc =NULL;
    }
}
else
{
    CRect rect;
    GetClientRect(&rect);
    pDC->FillSolidRect(rect, RGB(0,0,0));
}
}

```